Daniele Trovato

Degradation of Dissipative Characteristics of Friction Pendulum Isolators due to Thermal Effects

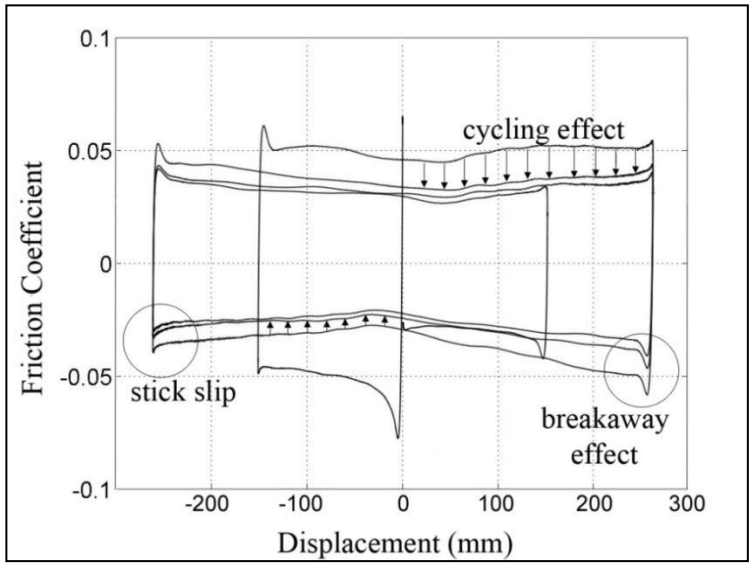

Dottorato di Ricerca in Ingegneria delle Strutture

Politecnico di Torino

Aprile 2013

Dottorato di Ricerca in Ingegneria delle Strutture
Politecnico di Torino, Corso Duca degli Abruzzi 24, 10129 Torino, Italy

Tutori: Prof. Andrea Giuseppe Ferro, Ing. Gianmario Benzoni

Coordinatore: Prof. Alberto Carpinteri

Acknowledgement

It would not have been possible to write this doctoral thesis without the help and support of the people around me, to only some of whom it is possible to give particular mention here.

I would like to express my gratitude to my advisors, Prof. Giuseppe Ferro for his support of my Ph.D study, for his patience and encouragement. He has given me the freedom to pursue various projects without objection and he was instrumental in my formation.

I extend my gratitude to Dr. Gianmario Benzoni for his technical guidance, scientific advice, for his many insightful discussions and valuable suggestions. He gave me the chance to work at Caltrans SRMD in San Diego and live one year in a beautiful place.

I thank also Dr. Davide Pedicone and Dr. Giuseppe Lomiento for their precious collaboration and support and Donato Innamorato for his essential job at the laboratory.

Besides my advisors, I would like to thank the rest of my thesis committee and especially Prof. Giuseppe Lacidogna and Prof Alberto Carpinteri for their essential support in the last part of my PhD. I gratefully acknowledge Dr. Gianfranco Piana for his friendship and the encouragement that have lasted over the last three years.

A warmly thank all the beautiful friends I met in San Diego, for their smile, enthusiasm and love they gave me.

At last but not the least I would lovely thank my parents for their guidance and continuous support.

Index

Index of figure

Chapter 1

1. Introduction

The purpose of my research is to predict the reliability of friction pendulum devices during their service life. These bearings are characterized by the capability to undergo large displacements despite their compact size. This peculiar property makes this device competitive among other commonly used isolation devices such as lead-rubber bearings. In these supports the dissipation of seismic motion occurs exclusively by the friction produced during sliding of the surfaces while the seismic isolation is obtained by the shifting of the natural period of the superstructure.

Over the time, the interest of the scientific community for such devices has focused on the study of the friction coefficient involved during the motion and also on its dependence on certain mechanical variables such as velocity and apparent pressure. Several studies have shown that the friction coefficient in a contact problem between polymer (PTFE) and stainless steel deviates from the Coulomb's friction law. Furthermore, most recent studies have shown that the coefficient of friction is closely related to the increase of temperature due to the thermal effect. This phenomenon consists in a cyclic degradation of the dissipative capacities of friction pendulum that in the design phase is not considered. The observed reduction of energy dissipated during repetitive cycles is

often coupled with peak displacements larger than predicted with potential consequences on the whole structure's safety.

This PhD study is composed by 8 chapter and it start with an introduction of the basic concept in seismic base isolation (Chapter 2) while the main characteristics of friction pendulum devices are introduced are defined in Chapter 3. The basic theory of frictional heating useful to describe the increase of temperature which occurs in polymer-stainless steel surface is introduced in chapter 4.

Through an experimental campaign carried out with single pendulum bearings, the dependence of the friction coefficient with the temperature rise has been investigated in chapter 5, in order to propose a phenomenological model able to assess the real performance of the friction pendulum.

Specifically, in chapter 5 is described the experimental analysis carried out in Caltrans SRMD Testing Facility of San Diego University of California. A series of friction pendulum have been tested at Caltrans SRMD which is equipped with a shaking table test specifically designed for full-scale tests. During the tests, the table was also equipped with a thermographic camera specially calibrated for the type of material tested (polished stainless steel). Thanks to the use of the camera it has been possible to evaluate the temperature rise during the whole testing time and in the portion of the concave surface affected by the thermal heating.

In chapter 6, an analytical comparison has been carried out between the friction coefficient recorded during the test and the temperature rise obtained with the analytical model of degradation of the friction coefficient introduced in chapter 4. Finally in chapter 7 a prediction model that takes into account mechanical

variables such as velocity and apparent pressure, and also the degradation of dissipative characteristics of a friction pendulum due to thermal effects, is given.

The proposed friction model is suitable for immediate implementation in generalized structural analysis codes and provides an important design tool for a more realistic assessment of the seismic response of structures equipped with Friction Pendulum devices.

Chapter 2

2. Seismic Isolation

The recent seismic events occurred in the regions with high seismic hazard like in Japan (Tohoku, 2011) and Chile (2010), have shown that despite the efforts made to reduce and prevent economic losses, casualties and injuries, earthquakes continue to be a huge plague in the world.

For mitigating the seismic hazard many seismic construction designs and technologies have been developed over the years and particularly attention has been given to the effects of earthquake in the most vulnerable buildings like bridges, hospitals, data centers, etc.

Many protection system have been developed and utilized in many application all over the world, and the seismic isolation has become a relevant and important way to improve the seismic response in the design of new buildings and in the retrofitting of existing ones.

In seismic, isolation devices are applied between the superstructure and the foundation of the building to decouple the structures from the ground earthquake motion. These Seismic Response Modification Device (SRMD) refer to a large family of mechanical devices that can modify the dynamic characteristics of a structure increasing for instance the flexibility of the structures and giving an appropriate damping.

These mechanical systems, in terms of functioning technique, are divided in two main categories. The first category includes devices that improve structural

dynamic performance by adding supplementary stiffness and/or damping properties to help structure gain more stability and energy dissipation property. Viscous Fluid Dampers and Tuned Mass Devices are two well recognized devices of this category. The second category includes devices that modify structural response by the applications of devices mounted underneath the structure witch enforced the discontinuity of the ground motion. The mechanical systems which belong to the latter category are referred to as base isolation, and they are "Seismic Isolation Devices".

2.1. Introduction of seismic isolation

Seismic design of structures is based on the condition that the capacity of resistance and deformability of the structure is greater than the demand due to the motion of the ground. A seismic event is manifested by the vibrations induced by the movement of the ground and generates in the structure forces inertia equal to the product of its masses for accelerations. To avoid structural damage during an earthquake, it would be necessary to increase the resistance of the structure proportionally with the intensity of the earthquake.

The structural damage does not correspond to a condition of collapse, because the structure has significant extra resistance in the plastic range. In fact, the structure has the ability to deform while maintaining a constant resistant force of the structural elements involved. The indefinite increase of the resistance capacity of the structural elements is not the best design method because it is not cost convenient. The current codes and regulations permit the use of structural ductility to satisfy the capacity design condition related to resistance, deformations and

displacements. The acceptance of high demand for ductility constitutes acceptance of damage to structural elements as a result of moderate-high earthquake intensity and relative costs of interruption and service repair. The seismic design can be developed according to two possible strategies:

- to increase the structural strength, thereby increasing the manufacturing costs and allowing more accelerations on the structure.
- to increase the ductility of the structure through a design aimed at developing favorable yielding mechanisms to obtain high and flexible local capacity by accurate construction details.

Current codes are inspired by the latter alternative. With the capacity design method, seismic forces are focused on the structural elements which have ductility capacity whereas the unfavorable collapse mechanisms are reduces. Modern seismic isolation design has the main purpose to avoid the collapse of the structures for high intensity earthquake, to reduce the damaging of non-structural building elements for medium earthquake by means of an ad hoc selection of design criterions and structural features such as stiffness, resistance and ductility.

Some modern techniques of passive seismic protection of structures use special devices to reduce demand and concentrate on them rather than in parts of the structure, the absorption and dissipation of energy.

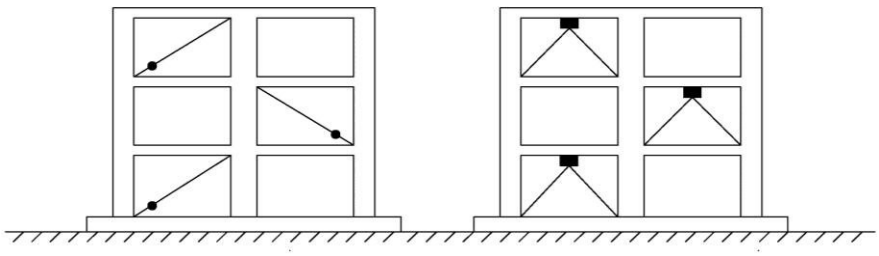

Figure 1: Schematic example of dissipative braces.

An effective technique consists in the dissipation of energy, generally based on the use of dissipating braces inserted in the frame of structural buildings. These devices dissipate the energy transmitted by the earthquake to the structure, significantly reducing the displacements of the structure in the plastic range. A dissipation of viscous type does not create particular changes to the dynamic behavior of the structure as a whole but instead increases the damping capacity of the overall structure. The devices inserted as illustrated on Figure 1 have a hysteretic behavior due in particular to an elastic-plastic behavior. The choice of devices reflects the criterion of capacity design. The technique based on the dissipation of energy is well suited to adjustment and seismic improvement of existing framed construction, when the buildings are built in adjacency and joints are small.

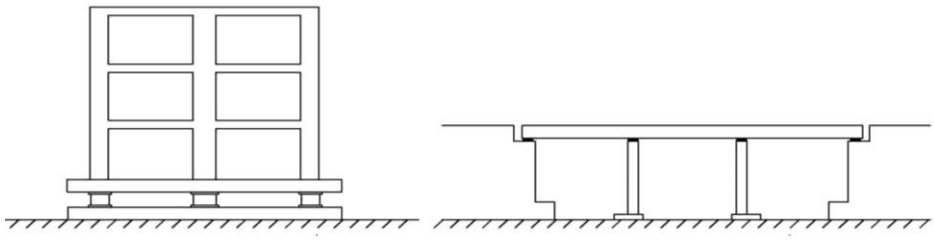

Figure 2: Base isolation in buildings and bridges.

Another effective method is seismic isolation. This method reverses the problem and achieves the isolation through the reduction of the global demand of the structure, reducing the energy transmitted from the ground over the entire structure (see Figure 2).

2.2. Basic Concepts in Seismic base Isolation

Base isolation, also known as seismic base isolation or base isolation system, is one of the most popular means of protecting a structure against earthquake forces. Besides it is one of the most powerful tools of earthquake engineering among the passive structural vibration control technologies. It is meant to enable a building or non-building structure to survive a potentially devastating seismic impact.

All the technologies developed in the recent past are used to provide effective solutions for a wide range of seismic design problems. Base isolation system is well effective when for example a large structure has an important role which involves for it to be operational right after a severe earthquake, like hospitals, airports, data centers and public civil facilities.

In all those cases the use of isolation system can considerably increase both the seismic performance of the structure and its seismic sustainability , and reduce the cost providing the designed earthquake resistance. Reduced costs stem from reduced seismic loads, from reduced ductility demand, and from lower structural deformations which could bring lower costs for internal and external details of the building.

Typical earthquake accelerations have dominant periods of about 0.1-1s with a pick of values between 0.2 and 0.8s. Structures with a natural period of vibration within the range of 0.1-1s are therefore vulnerable because they could resonate.

The main concept of base isolation consist in a system able to reduce the effect of the horizontal components of the ground acceleration introducing devices having low horizontal stiffness between the structure and the foundation (Figure 3). The substructure is generally very rigid and takes approximately the same ground acceleration, while the superstructure uses the benefits deriving from the deformation due to the introduction of isolators. This application gives in the isolated structure a fundamental period of oscillation bigger than an equivalent fixed-base structure avoiding the resonance of the structures and reducing the seismic acceleration response. In this way during the shaking ground motion the deformation are concentrated in the isolation system protecting a building or non-building structure's integrity.

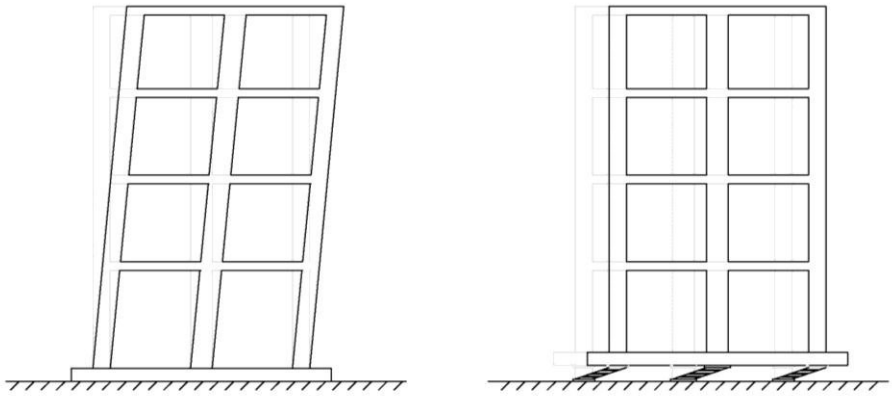

Figure 3: Schematic comparison of the deformation between a fixed base and a base isolated structure.

The shift of the period and the consequent increased flexibility also affect the horizontal seismic displacement of the structure as shown in Figure 4. The same picture shows how excessive displacements are controlled by the introduction of increased damping. As a consequence of the shift of the period the higher modes of the structure don't participate in the motion. If there is high energy in the ground motion at these higher frequencies, this energy cannot be transmitted into the structures.

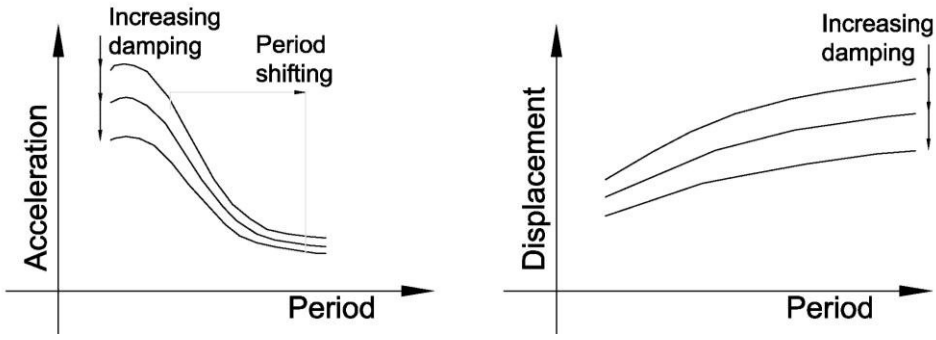

Figure 4: The increase of flexibility of the structure products a shifting of the period and, as a consequence, lower acceleration response. The increased period increases the total displacement of the isolated system.

The isolation system does not absorb the earthquake energy, but addresses it to the deformation and the dynamics of the system. Although a certain level of damping is beneficial to suppress any possible resonance of the isolation frequency and for controlling excessive displacement of the structure, (see Figure 4), the concept of isolation it is does not strictly rely on damping. On the other hand, excessive damping could reduce the effectiveness of the isolation.

Seismic isolation systems are particularly designed and installed on the base of the structure to maintain all components of the superstructure within the elastic range. The displacement of the structure can be concentrated in the isolator components, allowing little deformation in the structure, which moves like a rigid body mounted on the isolated system.

The seismic isolation design can be achieved in two main strategies:

- Increasing of the period, with or without dissipation of energy.
- limitation of force, without or with energy dissipation.

With the first strategy, the acceleration of the structure is reduced according to the principles just described and summarized in Figure 4. The reduction of the effects on the structure is basically achieved through the absorption of the seismic energy input to strain energy, largely dissipated with the hysteresis behavior of the devices for each cycle of oscillation. The power dissipation of the isolation system reduces both the displacements at the base, up to a certain limit, the forces transmitted to the superstructure.

In the strategy of force limitation, the devices are used for rigid or elastic perfectly plastic behavior, or otherwise highly non-linear, with a branch nearly horizontal for large displacements. The reduction of the effects on the structure occurs through the limitation of the force transmitted to the superstructure. The imposition of an upper limit on force transmitted can also be seen as an application of the capacity design in terms of the structural system, in which a hierarchy is established between the resistance of the structure and the resistance of the isolation system. The strategy based on the increase of the period is the most frequently adopted in the isolation of buildings. Than one based on the limitation

of the force is used mainly in cases in which the control of forces induced on the structure represents the crucial aspect of the design, as for example it may occur in seismic retrofitting of structures. It is essential to adopt a control of the transmitted force even when the methodology of the increase period reaches its limits of applicability and convenience as for example in case of deformable structures or earthquakes expected with a high energy content at low frequencies.

It is possible to sort seismic isolation systems in two major models. In Figure 5-a, the first case shows a linear damped isolator by means of a linear spring and a viscous damper. As a consequence the hysteretic loop created in the force-displacement has an effective slope which represents the stiffness of the isolator. Figure 5-b represents a bilinear isolator with two parallel springs in which one of them has a Coulomb dumper in series with it. The resultant force-displacement loop is bilinear, characterized with two slopes which represent the initial and the yielded stiffness respectively, resulting of the elastic and plastic deformation of the isolator. The most common linear isolator is the laminated-rubber bearing, whereas non-linear devices include high damping bearing, lead rubber bearing and the friction pendulum.

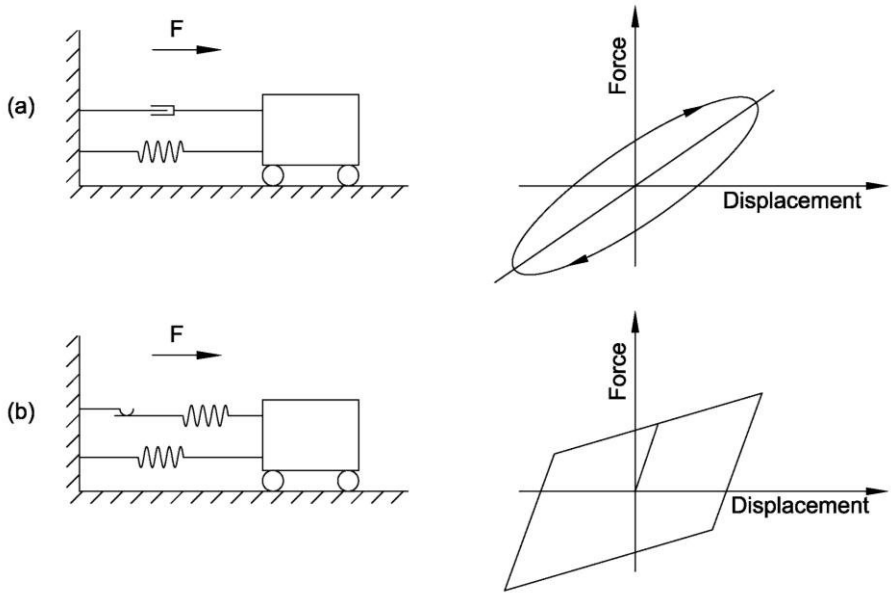

Figure 5: Simplified representation of the force-displacement loops produced of a linear damped isolator (a); a bilinear isolator with a Coulomb damper (b) [66I].

The most application of isolated buildings use multilayered laminated rubber bearing. These devices have reinforced steel layers to increase the stiffness in the vertical direction and for carrying the vertical load of the structure. Conversely they are soft in the horizontal direction as required to the isolation effect. Another most commonly used isolation system is the lead-plug rubber bearing. These bearings are composed with multilayered, laminated elastomeric bearings with a lead circular plugs embedded in the core of the isolator. The lead plug introduces an extra damping in the seismic isolation and often they are coupled with normal elastomeric bearing.

Most recently a new device based on sliding elements has been used (Friction Pendulum System). These devices provide a low friction contact layer which transmits a lower shear forces in the structures.

The benefits of adopting seismic isolation are varied. The significant reduction of the accelerations on the structure determines the significant differences with respect to the fixed base configuration:

- the reduction of inertia forces and then of stress produced by the earthquake on the structure, in order to avoid damage of structural elements (beams, columns, etc.);
- a drastic reducing interstory displacement, such as to significantly reduce or eliminate the damage to non-structural elements (cladding, partitions) and ensure the full functionality of the building, even after a violent earthquake.
- high protection of the structural content.
- a much lower perception of earthquakes by the occupants.

All these technology can be used both for new structural design and seismic retrofit. Although isolation techniques have been used for new construction of building, 1989 Loma Prieta and 1994 Northridge earthquake in California incited designers in applying these devices in process of seismic retrofit in some of the most prominent U.S. monuments, e.g. Pasadena City Hall, San Francisco City Hall, Salt Lake City and County Building or LA City Hall or the U.S. Court of Appeals in San Francisco were mounted on Base Isolation Systems (Figure 6).

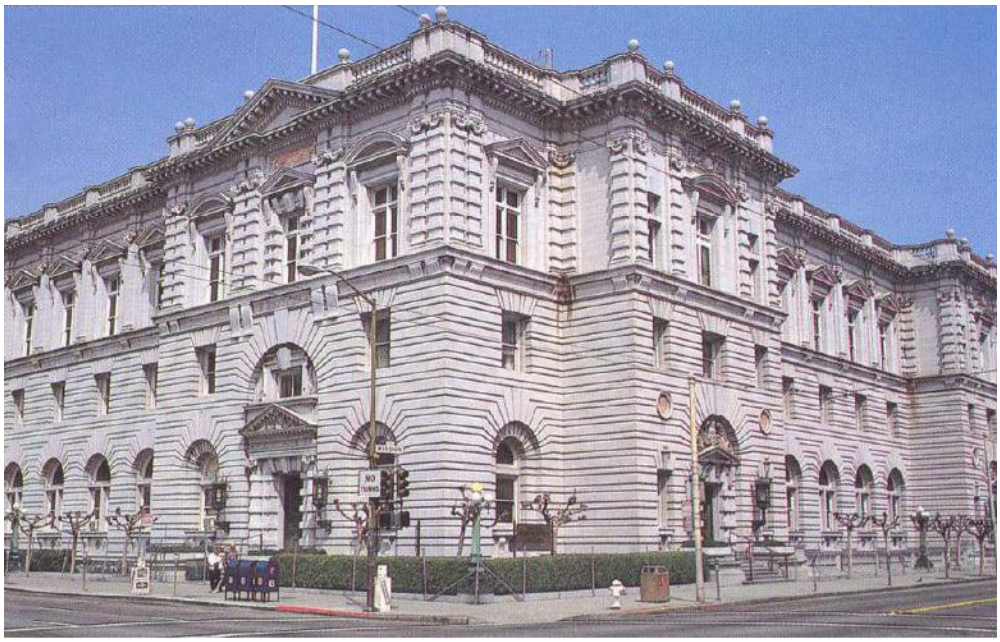

Figure 6: The U.S. Court of Appeals was damaged in the 1989 Loma Prieta earthquake. It is retrofitted with a total of 256 Friction Pendulum Seismic Isolation Bearing, installed between the existing foundation and columns

As a result of the Hyogo-ken Nanbu earthquake of 1995 and the consequently creation of an adequate specific legislation in 2000 which liberalized the use of seismic isolation devices, Japan is increasingly consolidating its leadership in the world in this sector with over 6,000 current isolated buildings. In this country, the tendency is now to isolate skyscrapers buildings supported by a single large isolated structure (artificial ground plate) as well as isolate small and light private buildings.

In Italy the application of modern seismic started in 1975 for bridges and viaducts and in 1981 for buildings. Particular attention is dedicated in seismic isolation of new hospitals and buildings relevant to the civil protection, for the

schools. Nowadays, Italy represents one of the world leaders in the number and importance of the application of modern seismic in the field of preservation of cultural heritage.

2.3. Theory of Base isolation

The behavior of an isolated building could be explained using a linear models and a linear analysis. This is possible when the structure is provided with a linear isolation system having low damping and an effective isolator flexibility higher than the effective structural flexibility. The structures are usually approximated by linear models with a moderate number N of concentrated masses m_r, like shown in Figure 7a.

Two general masses m_r and m_s are interconnected by a component with a stiffness k(r,s) and a damping coefficient c(r,s). In Figure 7a, the generic mass m_r has a single horizontal degree of freedom, and it is subject to a seismic displacement of u_r with respect the supporting ground, or $u_r + u_g$ if one considers the horizontal displacement of the ground. Each discrete mass has an inertia force $-(\ddot{u}_r - \ddot{u}_g)m_r$, while the interconnection exerts an elastic force $-(u_r - u_s)$k(r,s) and a damping force $-(\dot{u}_r - \dot{u}_s)$c(r,s). In general the N equations which represent the equilibrium of the forces are expressed in matrix form:

$$[M]\ddot{u} + [C]\dot{u} + [K]u = -[M]\ddot{u}_g \tag{2.1}$$

where [M], [C] and [K] are the mass, damping and stiffness N x N matrices respectively. The seismic responses of the N-mass linear system are obtained as the sum of the responses of N independent modes of vibration. Each mode n has a

fixed orthogonal modal shape Φ_n, a natural frequency ω_n and damping ζ_n. The natural frequencies of the undamped modes are obtained by assuming that there are free vibrations in which each mass moves as a sinusoid with a frequency ω.

$$u = \phi \sin(\omega t + \theta) \tag{2.2}$$

Substituting (2.2) in equation (2.1), removing the ground acceleration and the damping terms

$$\left([K] - \omega^2 [M]\right)\phi \sin(\omega t + \theta) = 0 \tag{2.3}$$

The non-trivial solution is given by

$$\det\left([K] - \omega^2 [M]\right) = 0 \tag{2.4}$$

Equation (2.4) gives N positive frequencies ω_n which represent the undamped natural or modal frequencies of the structure. It may be shown that the shape Φ_n of the n mode is found substituting ω_n in equation (2.3) giving N linear homogeneous equations

$$\left([K] - \omega_n^2 [M]\right)\phi_n = 0 \tag{2.5}$$

Where in each modal shape Φ_n the top displacement is fixed one. A mode-shape matrix is defined as

$$[\Phi] = [\phi_1 \ldots, \phi_n, \ldots \phi_N] \tag{2.6}$$

In order to illustrate the natural periods and mode shapes for base fixed and isolated structures, let's use a continuous uniform shear structure, having a frame building equal-mass floors, with the columns considered inextensible and with the same shear stiffness.

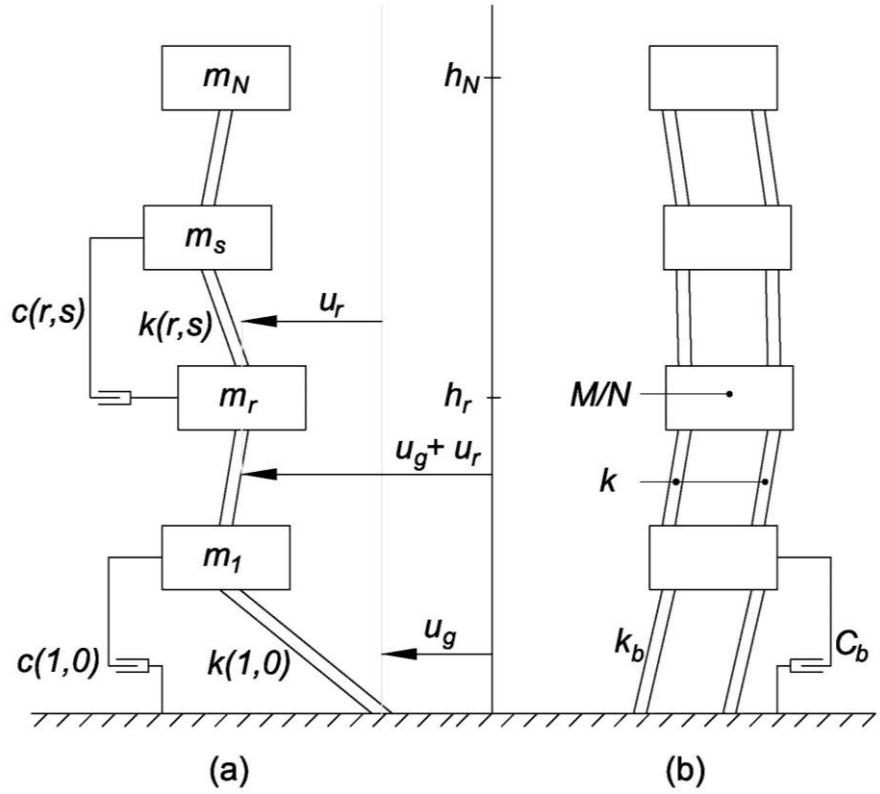

Figure 7: (a) Linear shear structure with concentrated masses. (b) Uniform shear structure with total mass M [66].

As illustrated in picture Figure 7b, let consider m_r = M/N and k(r,r-1)=KN with r=1,…,N. The model has a linear isolation with an horizontal stiffness k(1,0)= K_b typically considered less than the overall shear stiffness K. Letting the structural model continuous N $\rightarrow \infty$ it may be shown that the mode shapes ϕ_n have a sinusoidal profile, and that the modal frequencies ω are proportional to the number of quarter-wavelengths in the modal profile. Non-isolated modes have (2n-1) quarter wavelengths and isolated modes have just over (2n-2) quarter

wavelengths. The first mode shape is give with $T_{n1}(U)/T_{n1}(I)$, where $T_{n1}(U)$ is the first non-isolated periods and $T_{n2}(U)$ is the first isolated period, with $T_{n1}(I)>T_{n1}(U)$. The higher isolated modes converge to (2n-2) quarter wavelengths increasing n. For an isolated structure, the first mode period is controlled by the isolator stiffness. The others modes periods for both isolated and non-isolated structures are controlled by the structure.

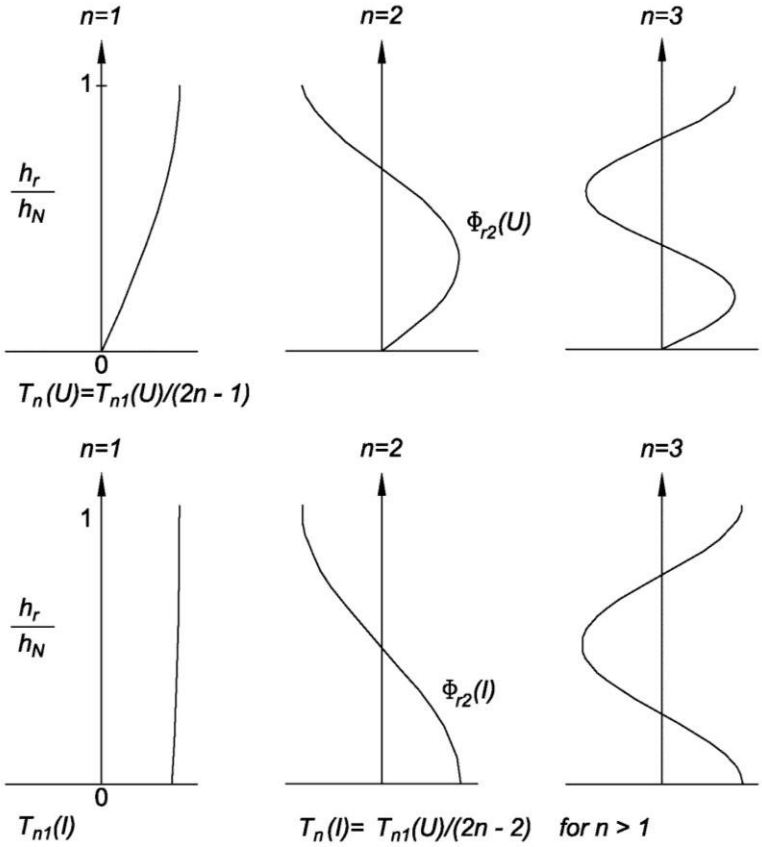

Figure 8: Variation in height of ϕ_{rn} which is the approximate shape of the n^{th} mode at the r^{th} level of the continuous uniform shear structure. The modal shapes and periods are represented in the unisolated case (U) and isolates (I).

The general features given in Figure 8 are also representative of non-shear and non-uniform structures, even though the argumentation is less simple. In the case considered here, the isolated mode-1 profile is still approximately rectangular. The high modes profiles are no longer sinusoidal but they present a sequence of nodes and antinodes.

In order to simplify the interpretation of the behavior of a building block, it is possible to identify two fundamental behaviors in the deformability of the system, structural seismic isolation and superstructure, and two inertial components, the mass of the base of the structure, directly bound to the ground through the isolation system, and the mass of the superstructure which moves with respect to the latter, being connected to it by the superstructure itself.

An insight example that provides the fundamental concepts of seismic isolation is illustrated in Figure 9 [52], which represents the extreme simplification of the structural system described above, in which the masses, stiffness and energy dissipation of the superstructure are distributed along the height the building. In this example is shown the mode shapes in an isolated building with two 2 degree of freedom which a mass, m, carried on a linear structural system on a base mass, m_b, supported on an isolation system.

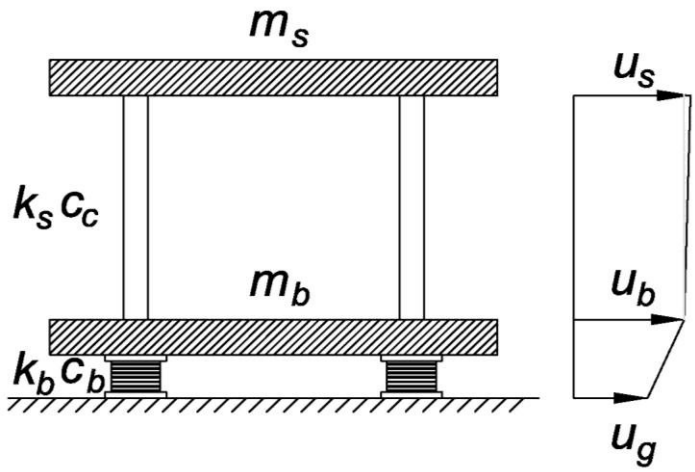

Figure 9: Two degree of freedom isolation system model.

The stiffness and damping of the superstructure and isolation system (supposed to have an elastic behavior) are denoted k_s and c_s, and k_b and c_b, respectively. The model is characterized by two dynamic degrees of freedom, corresponding to the horizontal displacements of the two masses, denoted in Figure 9 by u_s and u_b, while u_g represents the displacement of the ground.

In order to simplify the interpretation of the behavior of the system, the problem is carried out in terms of relative displacements:

(2.7) $$v_b = u_b - u_g$$

(2.8) $$v_s = u_s - u_b$$

The basic equations of motion of the two degrees of freedom system shown in Figure 9 are written by applying the d'Alembert principle:

(2.9) $$(m + m_b) \cdot \ddot{v}_b + m \cdot \ddot{v}_s + c_b \cdot \dot{v}_b + k_b \cdot v_b = -(m + m_b) \cdot \ddot{u}_g$$

$$m \cdot \ddot{v}_b + m \cdot \ddot{v}_s + c_S \cdot \dot{v}_S + k_S \cdot v_S = -m \cdot \ddot{u}_g \quad (2.10)$$

We defined the mass ratio γ as:

$$\gamma = \frac{m}{m + m_b} \quad (2.11)$$

and the frequencies ratio:

$$\varepsilon = \frac{\omega_b^2}{\omega_s^2} = \frac{k_b \cdot m}{(m + m_b) \cdot k_s} = \left(\frac{T_s}{T_b}\right)^2 = O(10^{-2}). \quad (2.12)$$

the damping ratio, ξ_b e ξ_s are given by:

$$2 \cdot \omega_b \cdot \xi_b = \frac{c_b}{(m + m_b)} \quad (2.13)$$

$$2 \cdot \omega_s \cdot \xi_s = \frac{c_s}{m} \quad (2.14)$$

In term of these quantities the basic equations of motion become:

$$\ddot{v}_b + \gamma \cdot \ddot{v}_s + 2 \cdot \omega_b \cdot \xi_b \cdot \dot{v}_b + \omega_b^2 \cdot v_b = -\ddot{u}_g \quad (2.15)$$

$$\ddot{v}_b + \ddot{v}_s + 2 \cdot \omega_s \cdot \xi_s \cdot \dot{v}_s + \omega_s^2 \cdot v_s = -\ddot{u}_g \quad (2.16)$$

the variables $\omega_b, T_b,\ \xi_b$ and $\omega_s, T_s,\ \xi_s$ are the pulse, the period and the damping ratio respectively of two elementary oscillators, one involves the complete mass constrained by isolation system, the other only by the superstructure assumed fixed at the base.

Beside the ratio of the pulsations, can be introduced by the ratio of isolation, which is the ratio between the periods $\frac{T_b}{T_s}$, equal to the square root of the inverse of

ε. The resolution of eigenvalues and eigenvectors problem leads to the definition of the two modes of vibration of the structure. Assuming $\varepsilon \ll 1$, (superstructure much more rigid than isolators), it is possible to greatly simplify the problem. The approximate expressions of the two modal frequencies are reduced to:

(2.17) $$\omega_1^2 = \omega_b^2 \cdot (1 - \gamma \cdot \varepsilon)$$

(2.18) $$\omega_2^2 = \frac{\omega_s^2}{(1-\gamma)} \cdot (1 + \gamma \cdot \varepsilon)$$

The modal shapes with $(\phi_b^i = 1), i = 1, 2$, are:

(2.19) $$\Phi_1^T = \{1, \varepsilon\}$$

(2.20) $$\Phi_2^T = \left\{1, -\frac{1}{\gamma} \cdot [1 - (1-\gamma) \cdot \varepsilon]\right\}$$

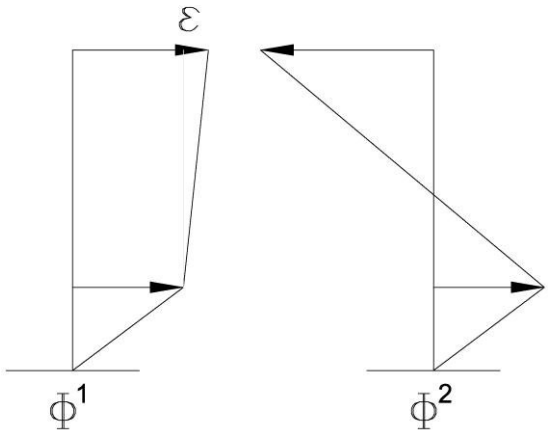

Figure 10: Mode shapes of two degree of freedom isolation system model.

Figure 10 shows the mode shapes of two degree of freedom of the isolation system model. The structure is almost rigid in the first mode shape. The second mode shape produces deformation in both structure and isolation system, with a displacement of the base comparable with the displacement of the top, but in opposite direction. The frequency of the first mode represents the characteristic of the isolated model when the structure is rigid.

Determined the vibration modes of the structure, the system response is expressed as a linear combination of the mode shapes Φ_1 e Φ_2 through two modal coefficients (q_1 and q_2) that are time-dependant:

$$v_b = q_1 \cdot \Phi_{11} + q_2 \cdot \Phi_{12} \tag{2.21}$$

$$v_s = q_1 \cdot \Phi_{21} + q_2 \cdot \Phi_{22} \tag{2.22}$$

the introduction of vibration modes allows to uncouple the equations of motion in the modal coefficient (q_1, q_2) of the form:

$$\ddot{q}_1 + 2 \cdot \omega_1 \cdot \xi_1 \cdot \dot{q}_1 + \omega_1^2 \cdot q_1 = -\pi_1 \ddot{u}_g \tag{2.23}$$

$$\ddot{q}_2 + 2 \cdot \omega_2 \cdot \xi_2 \cdot \dot{q}_2 + \omega_2^2 \cdot q_2 = -\pi_2 \ddot{u}_g \tag{2.24}$$

Where π_1 and π_2 and are the modal participation factors:

$$\pi_1 = 1 - \gamma \cdot \varepsilon \tag{2.25}$$

$$\pi_2 = \gamma \cdot \varepsilon \tag{2.26}$$

Similarly, it is possible to express in compact form the damping ratios associated with the vibration modes of the structure:

(2.27) $$\xi_1 = \xi_b \cdot \left(1 - \frac{3}{2} \cdot \gamma \cdot \varepsilon\right)$$

(2.28) $$\xi_2 = \frac{\xi_s + \gamma \cdot \xi_b \cdot \sqrt{\varepsilon}}{\sqrt{1-\gamma}} \cdot \left(1 - \frac{\gamma \cdot \varepsilon}{2}\right)$$

Considering a generic response spectrum, in terms of displacement $S_{De}(\omega, \xi)$ or pseudo acceleration $S_e(\omega, \xi)$ for the ground motion $\ddot{u}_g(t)$, it is possible to calculate the maximum modal response of the structure:

(2.29) $$q_{1\max} = \pi_1 \cdot S_{De}(\omega_1, \xi_1)$$

(2.30) $$q_{2\max} = \pi_2 \cdot S_{De}(\omega_2, \xi_2)$$

In order to estimate the maximum value of the maximum displacement of isolation system and the maximum interstory drift it is necessary to use the SRSS method:

(2.31) $$v_{b\max} = \sqrt{(q_{1\max} \cdot \varphi_{11})^2 + (q_{2\max} \cdot \varphi_{12})^2}$$

(2.32) $$v_{s\max} = \sqrt{(q_{1\max} \cdot \varphi_{21})^2 + (q_{2\max} \cdot \varphi_{22})^2}$$

Inserting the results obtained from Eqs. (2.25), (2.26),(2.29) and (2.30), we get:

(2.33)
$$v_{b\max} = \sqrt{(1-\gamma \cdot \varepsilon)^2 \cdot [S_{De}(\omega_1, \xi_1)]^2 + \gamma^2 \cdot \varepsilon^2 \cdot [S_{De}(\omega_2, \xi_2)]^2}$$

(2.34)
$$v_{s\max} = \varepsilon \sqrt{(1-2 \cdot \gamma \cdot \varepsilon)^2 \cdot [S_{De}(\omega_1, \xi_1)]^2 + [1-2 \cdot (1-\gamma) \cdot \varepsilon]^2 \cdot [S_{De}(\omega_2, \xi_2)]^2}$$

where the displacement of high frequencies (i.e., ω_2) is much smaller than at lower frequencies (i.e.,ω_1). Thus, when $\omega_2 S_{De}(\omega_1,\xi) \ll S_{De}(\omega_2,\xi)$, the value $\varepsilon^2 \cdot S_{De}(\omega_2,\xi_2)$ is negligible. So eq. (2.33) and (2.34) become:

(2.35) $$v_{b\,max} = (1-\gamma\cdot\varepsilon)\cdot\left[S_{De}(\omega_1,\xi_1)\right]$$

(2.36) $$v_{s\,max} = \varepsilon\sqrt{\left[S_{De}(\omega_1,\xi_1)\right]^2 + \left[S_{De}(\omega_2,\xi_2)\right]^2}$$

Similarly, the base shear coefficient is given by:

(2.37) $$C_s = \max\left|\frac{k_s\cdot v_s}{m}\right| = \omega_s^2\cdot v_{s\,max}$$

(2.38) $$C_s = \sqrt{\left[S_e(\omega_1,\xi_1)\right]^2 + \varepsilon^2\cdot\left[S_e(\omega_2,\xi_2)\right]^2}$$

Assuming $\varepsilon \ll 1$ it is possible to simplify Eqs. (2.17), (2.25) and (2.27):

(2.39) $$\omega_1 \cong \omega_b\,,\quad \pi_1 \cong 1,\quad \xi_1 \cong \xi_b$$

Assuming $S_{De}(\omega_1,\xi) \ll S_{De}(\omega_2,\xi)$ and $S_{De}(\omega_1,\xi) \cong 0$ we have the approximated equation:

(2.40) $$v_{b\,max} = S_{De}(\omega_b,\xi_b)$$

(2.41) $$v_{s\,max} = \varepsilon\cdot S_{De}(\omega_b,\xi_b)$$

(2.42) $$C_s = S_e(\omega_b,\xi_b)$$

This expressions indicate that for small ε and a typical design spectrum, the isolation system can be designed, at least in the initial phase, for a relative base displacement of $S_D(\omega_b,\beta_b)$ and the building for a base shear coefficient of

$S_e(\omega_b, \beta_b)$. These two values may be obtained by referring directly to the oscillator shown in Figure 9, with a mass equal to the mass of the whole superstructure, and stiffness and damping of the corresponding features of the isolation system k_b and ξ_b.

The reduction of the base shear as compared with a fixed-base structure, where $C_s = S_e(\omega_s, \beta_s)$, is given by $S_e(\omega_b, \beta_b)/S_e(\omega_s, \beta_s)$, which for a constant-velocity spectrum is ω_b/ω_s, or roughly of order $\varepsilon^{1/2}$; this underestimate the reduction in base shear because, in general, β_b will be larger than β_s.

2.4. American Earthquake Regulation for seismically isolated Structures

The first building to be seismically isolated in the United States, and the first in the world to incorporate high-damping rubber bearings, was the Foothill Community Law and Justice Center in Rancho Cucamonga, California, it was in 1985. The first rehabilitation of an existing structure with seismic isolation was in 1986 with the City and County Building in Salt Lake City, Utah. This project pioneered many construction methods of jacking and post-installation of bearings that are still used today. After the first building to use a seismic isolation system was completed, the Structural Engineers Association of Northern California (SEAONC) created a working group to develop design guidelines for isolated building. The Seismology Committee of the Structural Engineers Association of California (SEAOC) is responsible for developing provisions for earthquake-resistant design of structures. These previsions have been published for described

lateral force requirements for conventional structures generally know as the Blue Book [70] [71]. This publication served as the basis for different editions of the Uniform Building Code (UBC) and it still represents the most widely used code for earthquake design.

The first document describing prescriptive design requirements for seismic isolated buildings was published by the Structural Engineers Association of Northern California in 1986 [72]. This was informally referred to as the "Yellow Book," ostensibly to avoid confusion with the existing Blue Book . This document was created in response to the design and construction of isolated buildings and bridges that had already taken place. A need was identified for some minimum standard to assure the safety of the general public who may occupy isolated facilities. These early provisions sought to provide a margin of safety comparable to that of conventional structures. To this effect, the 1986 Yellow Book states:

*"[*These] limits on isolation system and superstructure response are intended to ensure that seismically isolated buildings will be at least as safe as conventional buildings during extreme events considering the uncertainties in the new and developing technology of *seismic isolation."*

In these recommended provisions, a clear process for selecting and proportioning the isolation system and the supported structure is provided. This process mimics that for conventional structures in an effort to maintain consistence between the design methodologies. Several key distinctions for the design requirements were introduced, including the following:

- The design base shear for the isolated superstructure is intended to limit ductility demand in the design basis earthquake relative to that

expected for the conventional fixed-base structure in the same level of earthquake.

- A review of the isolation concept and design is required, as established by the governing regulatory agency. Significantly, no prescriptive requirements for the scope of this review are established in recognition of the diverse nature of potential project sand the agencies charged with permit issuance.
- Testing requirements for isolation devices are required as part of the plan approval process.

Since the publication of the 1986 Yellow Book, these requirements were included as an Appendix to the 1991 UBC. The UBC code differs from the SEAONC guidelines because the first one explicitly requires that the design have to be based on two levels of seismic input. A design Basis Earthquake (DBE) is defined as the level of earthquake ground shaking that has a 10% probability of being exceeded in a 50-year period. The design provisions for this level of input require that the structure above the isolation system remains elastic. The second level of input called Maximum Capable Earthquake (MCE), which is the maximum level of earthquake ground shaking that may be expected at the site within the known geological frame-work. This level is considered as the earthquake ground motion that has a 10% probability of being exceeded in 100 years. The isolation system it is designed with this level of seismicity input as well as all the building separations and utilities that cross the isolation interface which has to accommodate the forces and displacements.

The 1994 editions of the UBC (1994) incorporated many changes. The vertical distribution of forces generally used for fixed-base structures were changed from uniform to triangular one. The 1994 code specified provisions for prototype tests that must be carried out before the construction of the isolators with the intent to establish the design properties of the isolation system.

The isolation provisions remained as an Appendix through each edition of the UBC, although revisions were made alongside those for conventional structures. Subsequent to the final version of the UBC in 1997, provisions for isolated structures have been contained in the International Building Code, the current version of which (ICC, 2002) directly references provisions contained in ASCE 7 (ASCE, 2002). Further changes and new terms have been introduced in the 1997 UBS version, like a more detailed description and division of new soil profile types such as hard rock, rock and soft rock.

The 1997 version represents a conservative, more complicated version of the UBC regulations which have changes the basic and simple set of the 1986 Yellow Book. Nowadays the conservatism in calculating design displacements and seismic forces seriously undermines the use of isolation technology by the engineering community.

The provisions of the current code requiring isolated buildings to be designed for lower ductility-based reduction factors inherently penalize the isolated superstructure and lead to unnecessarily high costs for the superstructure. A recommendation coming from the scientific and the general engineering community is put forth that future code provisions should include optional performance requirements for conventional isolated buildings, where the design forces are reduced substantially compared to the fixed-base counterpart, while the

expected performance is at least equivalent between the two. Other more recent publications have been released which provide further provisions for isolate structures as the chapter 9 of FEMA-356 (2000) about the seismic rehabilitation of existing buildings and chapter 13 of FEMA-368 (2001) for new construction.

Even though the base isolation technology is a reliable one and in Japan and New Zealand many applications exist even in the housing private contest, only a few new projects each year are presented and/or completed in USA. This because the codes are too conservative, and the professional category have the perception that base isolation design is complicated and even more expensive than others design process.

2.5. Design Principles of Seismic Isolated Structures and Bridges in the Italian code.

In Italy a first specific legislation to regulate the construction of buildings in concrete and masonry dates back to 1996, with a minister ordinance where for the first time were introduced. Immediately after the earthquake of 31 October 2002, which affected the territory on the border between Molise and Puglia, the Civil Protection has adopted the ordinance of Council of Ministers no. 3274 of 20.03.2003, which includes two chapters on seismic isolation of buildings and bridges, in order to provide an immediate response to the need to update the classification of seismic and earthquake regulations.

This seismic code has been for a long time not mandatory but only indicative of the basics of seismic design requirements. Only in 2008 it was published in the

“Gazzetta Ufficiale” the last Italian seismic code, called "Nuove Norme Tecniche delle Costruzioni" [46]. The new technical regulations are based on the European standards related to Eurocode 8 and in particular the parts relating to the evaluation of the seismic horizontal forces and the seismic isolation design.

The New Italian Code Introduce in Chapter 7 the seismic design rule action. Paragraph 7.10 provides criteria and rules for construction, bridges design and for the retrofitting of existing structures in which an isolation system is placed below the construction. The legislation introduces the terms "isolation" and "dissipation" referring to innovative techniques that propose the use of devices in the structure of the constructions in order to protect them from seismic loads.

The reduction of the horizontal seismic response can be obtained by two strategies of isolation, or through their appropriate combination:

a) increasing the fundamental period of the construction to bring it in the field of minors acceleration response;
b) limiting the maximum horizontal force transmitted.

In both strategies, the isolation performance can be improved through the dissipation in the isolation system of a substantial portion of the mechanical energy transmitted from the ground to the building.

Italian code includes provisions concerning the devices. Isolation devices and their connection to the structure must be designed to ensure the access and make the devices inspected and replaced.

To minimize the torsion effects, the projection of the center of mass of the superstructure and the center of rigidity of the isolation devices must be, as far as possible, coincident. Also, where the isolation system includes a dissipative and self centering function, it is necessary that such devices are, arranged in a way that

minimizes the torsion effects (e.g. increasing the perimeter) and are in number statically redundant.

To minimize the differences in behavior of the isolators, the compressive strength should be as uniform as possible. In the case of isolation systems that use different types of isolators, special attention must be paid to the possible effects of different vertical deformation under static and seismic actions.

To prevent or limit tensile strength that could occur in the isolators, the vertical load on an individual isolator should be zero or positive under the seismic actions. When the analysis proves that he vertical load are negative, it is should be proved with appropriate tests which the isolators is able to support such a condition.

2.6. Fundamental Characteristics of Common Devices

An Isolation system has to guarantee general requirements and criteria for seismic design. The isolation system performs one or more of the following functions:

a) Support of the vertical loads with high stiffness in the vertical direction and low stiffness or resistance in the horizontal direction, allowing significant horizontal displacements;
b) Energy dissipation mechanisms with hysteretic or viscous;
c) A self centering system;
d) Support for an adequate stiffness under horizontal loads non-seismic (wind force).

A classification of Seismic Isolation Devices could be set considering the different functional performance characteristics. All the category of seismic isolators creates a discontinuity between the over structures and the foundation system and they also contribute to damping the structure providing an additional dissipation of energy. Therefore it is possible classified seismic devices considering the mechanism they use to give dissipation of energy.

An isolation system is characterized by different combined devices which provide the behavior designed. The devices used in a isolation system could be composed by one or two and they are arranged in order to create a link between the foundation and the superstructure. Different devices have been proposed and developed in the last 20 years and some of them have been massively used in different part of the world, [Housner 1998, Buckle and Mayes, 1990].

The devices used in isolation systems can be distinguished in isolators and auxiliary devices. Isolators are generally bidirectional devices which perform the function of support the gravity loads, with high stiffness in the vertical direction and high deformability in the horizontal direction. Isolators system currently most in use can be divided into two specific categories:

- Isolators with elastomeric and stainless steel components, based on high elastic deformability of the rubber part of the bearing.
- Sliding isolators, made with two plan or curved surfaces characterized by low friction coefficient.

In Figure 11 is shown the ideal mechanical behavior of elastomeric and sliding isolators.

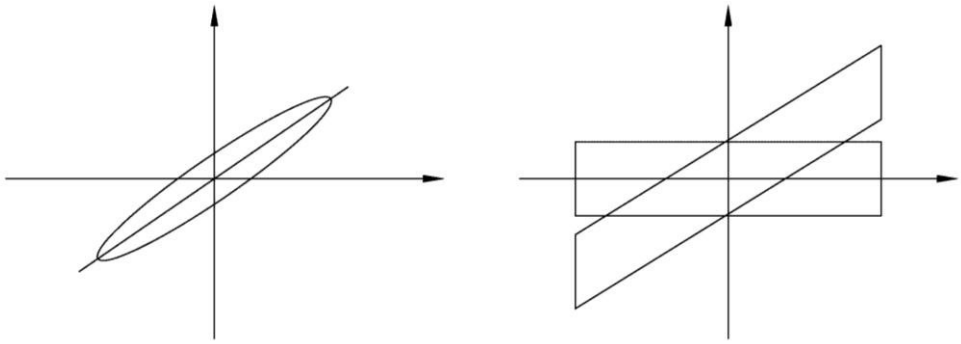

Figure 11: Schematic force-displacement loop for elastomeric isolator (on the left) and sliding isolators (on the right).

The auxiliary devices perform the function of dissipation of energy and / or re-centering of the system and / or provide lateral horizontal constraint under loads such as wind. It is possible to distinguish different auxiliary devices:

- devices with non-linear behavior, strain rate not dependent, based on the hysteresis of some metals, such as steel and lead, Figure 12 (loop a), devices based on friction between treated surfaces (loop b) or on super elastic properties of shape memory alloys (loop c) [34] particularly used to obtain self-centering properties.
- devices with viscous behavior (loop d), dependent on the speed of deformation, based on the extrusion of highly viscous fluids inside a cylinder equipped with orifices of appropriate size.
- devices with a linear/viscoelastic behavior (loop e), based on the shear deformation of special polymers devices.

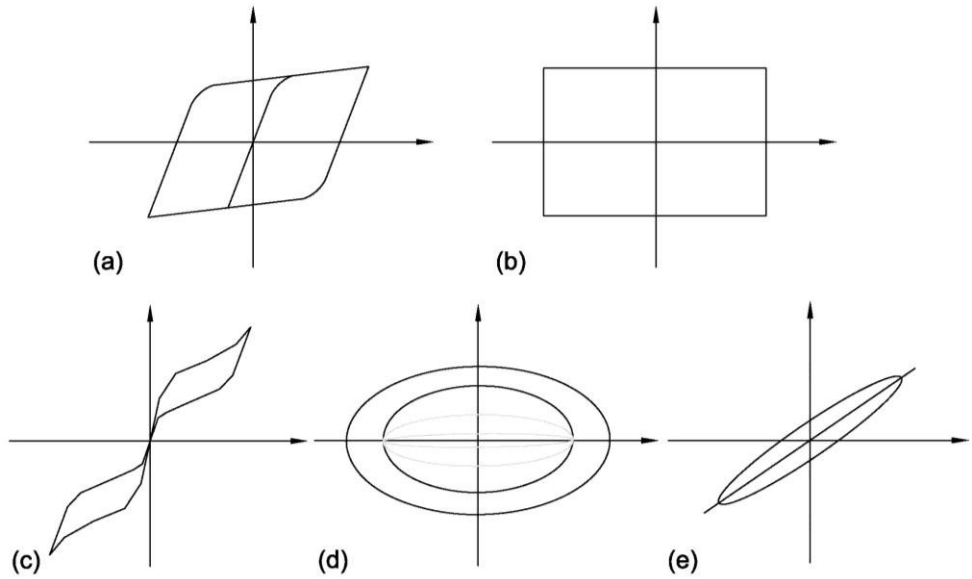

Figure 12: Force-displacement graphs of auxiliary devices with non linear behavior base on: (a) hysteresis of metal, (b) friction and (c) on super elastic properties of shape memory alloys; (d) auxiliary devices with viscous behavior (e) devices with viscoelastic/linear behavior.

The three most popular subcategories of elastomeric bearings are the Natural Rubber (LDRB), Lead Core Rubber (LRB) and High Damping Rubber Bearings (HDRB). The family of sliding bearings includes devices that utilize friction as mechanism of energy dissipation.

Among the Seismic Isolation Devices also exist hybrid bearings that couple the characteristics of sliding device as well as additional function obtained with different materials.

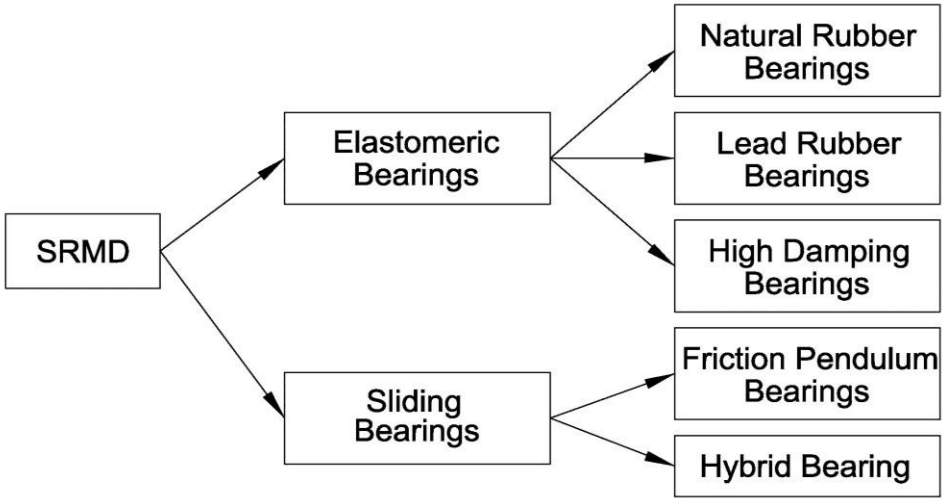

Figure 13: Different Seismic Response Modification Devices.

2.7. Isolation system based on elastomeric bearings

These devices are meant to accommodate large displacements imposed to the structures under a seismic activities. They have a layered structure manufactured by laminated rubber layers with steel shims. The rubber is the material which exhibits excellent resiliency and it can accommodate very high deformation. The use of steel shims is due to increase the vertical stability of the device and improves axial load capacity. Figure 14 shows the section view of a common type of rubber bearing having a circular section.

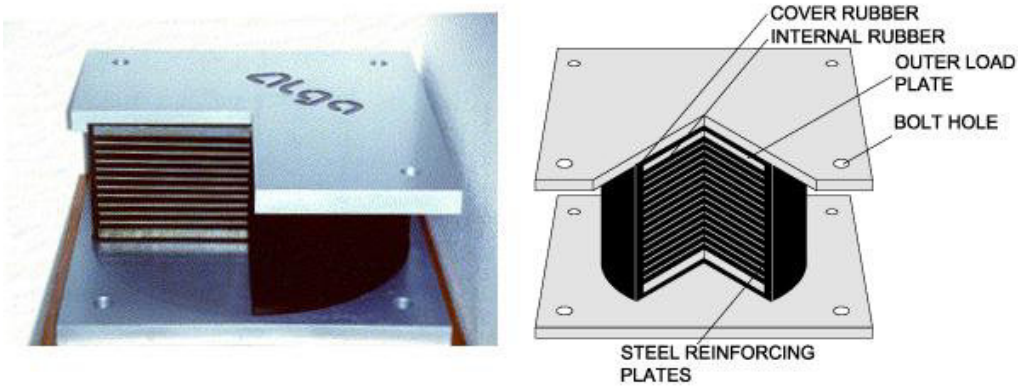

Figure 14: Section view of a laminated rubber bearing. (Source: Micheli I. et al.,2004)

During the motion a rubber bearing can accommodate shear strain and steel reinforcing plates inhibit flexural deformation while allowing to shear deformation. Therefore a laminated rubber beating may be considered like a vertical shear beam, in which pure shear deformations occur only in the internal rubber layers. The lateral stiffness of a laminated rubber bearing k_b can be approximated as

$$k_b = \frac{GA}{h} \tag{2.43}$$

where A represent the section area of the bearing, G rubber's shear modulus and h the cumulated height of rubber's layers. Lateral stiffness could be affected under the effect of large displacement due to flexural beam action and due to increased compression of the reduced overlap area. Although rubber beatings are made with different mix design, they could be sort in two major types, low and high damping rubbers. They can provide ~10% and ~15% damping respectively.

2.8. Isolation system based on elastomeric: Lead Rubber Bearing

Laminated-rubber bearings are able to supply the required displacements for seismic isolation. By introducing in a laminated rubber bearings a lead plug insert it is possible to obtain a single compact component able to support the structure vertically, to provide the horizontal flexibility together with the restoring force, and at the same time providing the required hysteretic damping. The main reason for choosing lead as the material for the insert in the isolators is due to the capacity of this metal to yield in shear at relative low stress of ~ 10 MPa at room temperature, behaving approximately as an elastic-plastic solid. When plastically deformed, lead can restore its mechanical properties with a simultaneous process of recovery and recrystallisation and grain growth. This means that lead regains its crystalline structure after yielding and continues to dissipate significant amount of energy. Deforming lead plastically at 20°C is equivalent to deforming iron or steel plastically at a temperature greater than 400°C. The simplest form of a lead core bearing is illustrated in Figure 15.

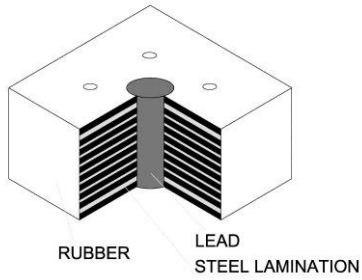

Figure 15: Lead rubber bearing which consist of a lead plug inserted into a vulcanized laminated rubber bearing.

It is composed by a lead plug that serves as energy dissipating component, rubber which is the component that provides restoring force to bring the structure back to the static equilibrium point and steel shims that serve as reinforcing elements for rubber to improve stability and compressive load capacity.

The initial elastic stiffness, k_u, is defined as sum of rubber and lead contribution

$$k_u = \frac{1}{h}\left(G_p A_p + G_r A_r\right) \tag{2.44}$$

Where A_p is the total area of the lead plug, G_p and G_r are the shear modulus of the lead plug and of the rubber respectively, A_r the area of the rubber and h the total height of the bearing.

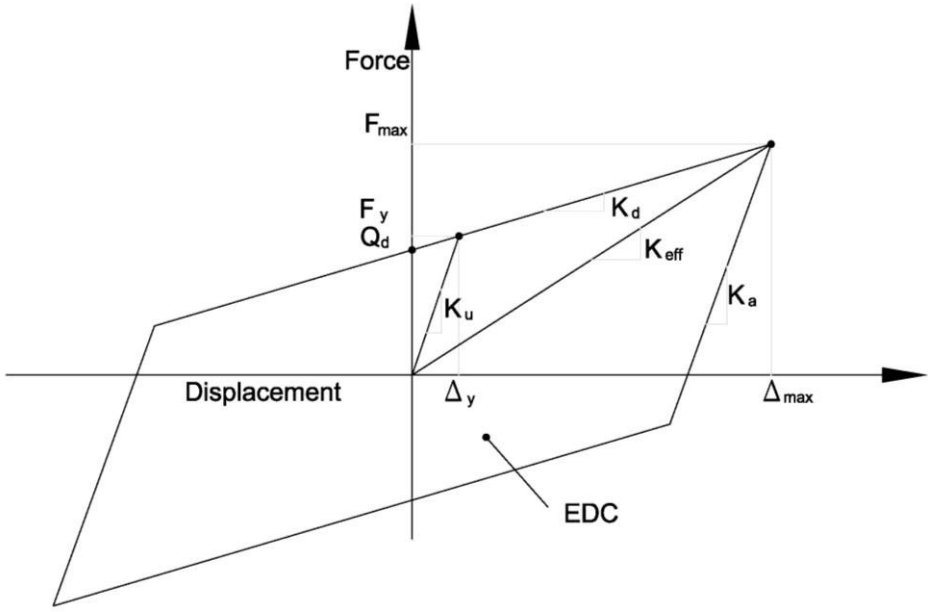

Figure 16: Force displacement idealized loop of an isolation bearing.

The post elastic stiffness, k_d, is mainly due to the rubber contribution

$$k_d = \frac{G_r A_r f_c}{h} \quad (2.45)$$

Where f_c is a coefficient related to the contribution of post yield lead. For current types of LRB's the elastic stiffness $k_u$ranges between 6.5 and 10 times post yield stiffness, k_d. The area made with the hysteresis loop is the measure of energy dissipated per cycle of motion (EDC). In the idealized system shown in Figure 16 the viscous damping is determined by

$$\beta = \frac{EDC}{2\pi k_{eff} \Delta_{max}^2} \quad (2.46)$$

where β represents the critical damping; k_{eff} the effective stiffness and Δ_{max} the maximum bearing displacement during a single cycle of testing. The yield force can be defined as the force required for yielding of the lead plus the elastic force carried by the rubber at the corresponding yield displacement

$$F_y = \tau_{py} A_p \left(1 + \frac{G_r A_r}{G_p A_p} \right) \quad (2.47)$$

where τ_{py} represents the shear yield strength of lead. The shear force at zero displacement is generally associated to the yield strength of the lead core

$$Q \cong \tau_{py} A_p \quad (2.48)$$

2.9. Isolation system based on sliding

Sliding bearings include all devices that accommodate large displacement by sliding rather than stretching, shearing or compressing. In this bearings, the dissipated energy is given by the friction caused by sliding of the surface. Figure 17 illustrate the friction pendulum device.

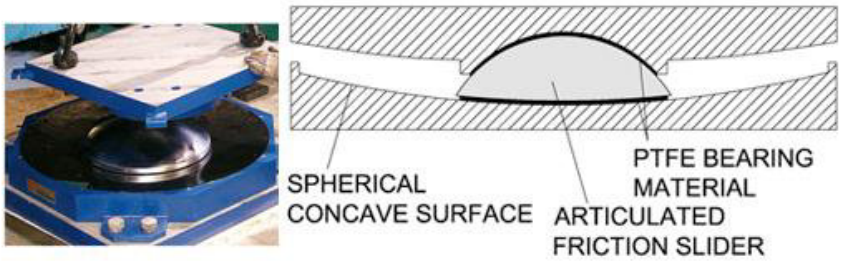

Figure 17: Components of a friction pendulum. Source: www.maurer-soehne .com/structural _protection _system.

The bottom portion (concave plate) is typically constructed as a spherical dish with a stainless steel overlaying. An articulated slider is free to move over the concave plate and inside the bearing plate. The bottom of the slider and the inside of the cup part of the bearing plate are lined with the self-lubricating low friction composite. The device uses the characteristics of a pendulum to lengthen period of the isolated structure. Seismic isolation is achieved by shifting the natural period of the supported structure. The natural period is controlled by the selection of the radius of curvature, R, of the concave surface. The natural period of vibration, T, if a rigid mass supported of FPS connections is determined from the pendulum equation

$$T = 2\pi\sqrt{\frac{R}{g}} \tag{2.49}$$

Where, g is the acceleration of gravity. This pendulum period is the period of a mass sliding on FPS isolators, and is the isolated period of vibration of a relatively stiff structure supported on the FPS. The isolated period becomes active once the friction force level of the isolators is exceeded. Choices of bearing, material composite, mating surface properties can define the amount of friction of the isolator and therefore the amount of energy dissipation per cycle during seismic movements. The lateral stiffness and friction force is directly proportional to the supported weight of the bearing. Very recently the original concept of the device was extended to bearings with 2 and 3 sliding surface. In Figure 18 is presented the typical force-displacement curve of a friction pendulum device. The intersection of the curve with the Y-axis (zero displacement) is obtained as product of the friction coefficient μ, times the supported load W, the stiffness k is defined as

$$k = \frac{W}{R} \tag{2.50}$$

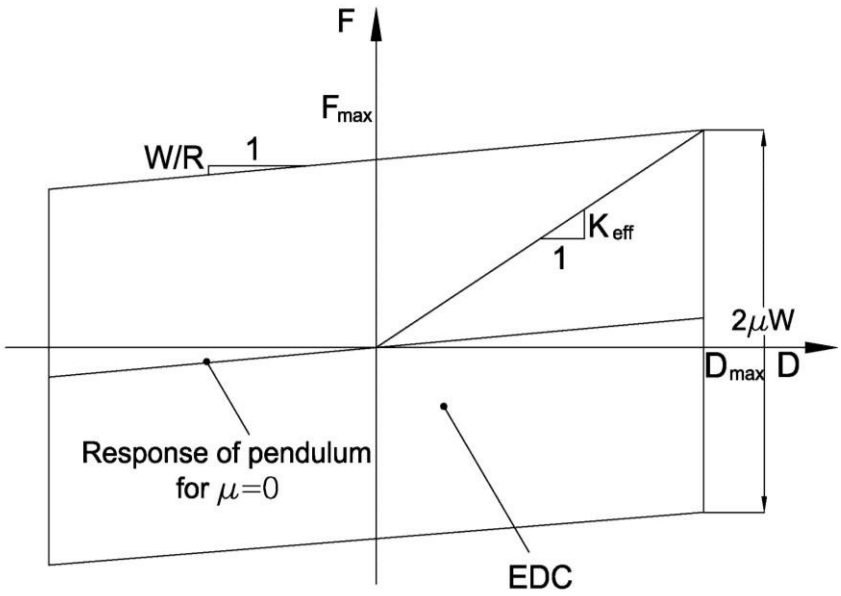

Figure 18: Schematic of hysteresis loop of a single concave Friction Pendulum bearing

Simpler sliding devices are available with flat sliding surfaces as shown in Figure 19. Their behavior is simply associated to the friction as source of energy dissipation.

Figure 19: Sliding device with flat sliding surface.

2.10. Development of seismic isolation in Italy and in the world

The first applications of structures disconnected from the ground date back to the ancient civilizations in China Greece, Peru, Italy. Layers of materials (coal, fleeces of wool, sand) were placed in correspondence to the foundation in order to favor the sliding of the structure with respect to the ground. The seismic isolation has been proposed in Italy after the earthquake of Messina and Reggio in 1908 with first patents compatible with the technology available at the beginning of the last century.

The first use of a rubber isolation system to protect a structure from earthquake was in 1969 for an elementary school in Skopje, Yugoslavia. The Pestalozzi School, a three story concrete structure designed and built by Swiss engineers, is isolated by a system known as the Swiss Full Base Isolation-3D System [69]. The rubber bearings, used in this application were completely unreinforced so that the weight of the building causes them to bulge sideways.

Figure 20: Pestalozzi School, Skopje, Macedonia, [52].

This bearings were able to bounce and rock backward and forward in an earthquake because the vertical and horizontal stiffness of the system is approximately the same. Because of this, the adoption of these devices turned out to be unsatisfactory and they were no longer used in others application.

Seismic isolation became a reality in the seventies in England, where were produced the first elastomeric bearings by the MRPRA (Malaysian Rubber Producers' Association Research), who devised a process for vulcanizing rubber layers with a stainless steel.

The first application was made in France in the early 70s, in order to safeguard a series of nuclear power stations and plant facilities. The utility developed a

standard nuclear power plant with the safety grade equipment qualified for 0.2g acceleration. The system combines laminated neoprene bearings with lead-bronze alloy in contact with stainless steel, the sliding surface being mounted on top of the elastomeric bearing. The coefficient of friction of the sliding surface is supposed to be 0.2 over the service life of the isolator (Electrcité-de- France System).

At the end of the 70s, the concept of seismic isolation was introduced in Italy, where it was widely applied to bridges and viaducts, in a period of remarkable development of the highway network. In the 80s the seismic isolation technique spread throughout the world with important applications in bridges and buildings strategic, especially in the U.S. and New Zealand, elastomeric isolators with high damping rubber using high dissipation (HDRB) or isolators with lead plug LRB [Tarics et al., 1984; Anderson, 1989, Charlerson. 1987, Reaveley et al. 1988]; in Japan the solution initially more adopted involved the use of low-damping elastomeric devices (LDRB) with the addition of viscous or hysteretic dissipaters [Kelly J.M.,1988].

A development of applications of seismic isolation system has occurred as a result of numerous studies carried out on the 80s who demonstrated the reliability of this method in the protection of the structural and non-structural parts in the presence of violent earthquakes. Moreover, two catastrophic events such as the 1994 Northridge and the 1995 Kobe earthquake, which struck respectively California and Japan, the development of seismic isolation had an additional input. Indeed in those events the isolated structures turned out to be an excellent performance than the performance of the equivalent fixed base structures located in the same affected area [Asher et al. 1995].

After these events, the number of applications of seismic isolation has undergone considerable development particularly in Japan. The interest for this application is remarkable in existing buildings, in which the seismic isolation can reach levels of security significantly higher than those achieved by the traditional type of retrofitting.

In USA the first examples of seismic retrofitting of existing buildings by basic insulation go back to the mid-90s. The structures were large buildings such as City Hall in Oakland [Walters et al. 1995], San Francisco [Naaseh 1995] and Los Angeles [Youssef 1995]. In all above cases it have been used rubber devices with lead plugs or high damping bearing (LRB or HDRB).

Recently , important applications of sliding isolators with curved (Friction Pendulum System, [Amin and Mokha 1995]) or flat surface have been applied in the U.S.A. or flat, with the addition of auxiliary devices re-centering rubber [Way and Howard, 1990].

The seismic isolation in Italy has experienced a constant development in last 40 years. After the earthquake in Friuli (1976) where the viaduct Somplago, protected with a seismic isolation system relatively simple but effective, was the only viaduct that was without damage after the earthquake event. Consequently to this event, in the decade from 1983 to 1993 seismic isolation was widely used in Italy for the protection of highway bridges and viaducts [Medeot 1991].

Over the past 15 years, important national and international research programs, involving companies, research institutes and Italian universities, have been carried out in order to develop the efficacy of the seismic devices.

At the same time, new technology for devices and isolation systems, and developing methods of calculation and verification of safety have been developed.

Different studies have involved the study seismic isolation at different scale levels and different devices such as the execution of dynamic tests on insulators individual small-scale [Kelly and Quiroz 1992] and real scale [Braga et al. 1997], or the performance of dynamic shaking table tests on scale models of isolated structures [Dolce et al. 2001a, 2006a and 2008].

Chapter 3

3. Friction Pendulum Devices

A system using pure sliding was proposed in 1909 by Jahonnes Avetican Calantarients, a medical doctor in England; he suggested to separate an existing structure from the foundation by a layer of tale.

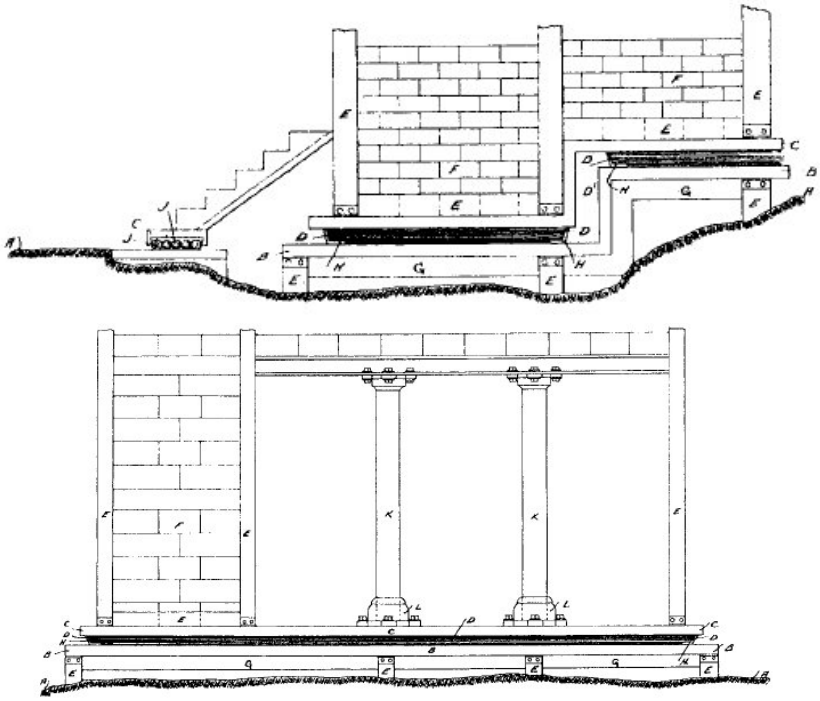

Figure 21: Calantarient's base isolation system using a layer of tale as the isolating layer, [52].

Calantarients understood that the isolation of systems reduce accelerations in buildings at the expense of large relative displacements between the building and the foundation. He designed a set of connections for utilities, which were restricted to gas lines and sewage pipes to accommodate for these displacements.

Isolation was first considered as a seismic-resistant design strategy by the Italian government after the great Messina. Reggio earthquake of 1908, which killed 160,000 people in unreinforced masonry buildings. After this event a commission considered an approach for earthquake resistant design to isolate buildings from the ground, by either interposing a sand layer in its foundation, or by using rollers under columns to allow the building to move horizontally. The idea that isolation can help buildings survive when great displacements occur, has been observed several times, in different places, for example after the severe Indian earthquakes of Dhubai (1930) and Bihar (1934) it was observed that small masonry buildings that slid on their foundations survived the earthquake, while similar buildings fixed at the base were destroyed.

A considerable amount of theoretical analysis has been done over the time on the dynamics of structures on sliding system subjected to harmonic input, or to an earthquake input. Udwadia, 1983 studied the periodic response of a linear oscillator on a coulomb friction sliding interface. Contrary to the general perception that friction will always reduce the response, they discovered that the response may be even larger than might be expected in the equivalent fixed base model, and that the single degree of freedom model had subharmonic resonance frequencies generated by the sliding interface.

The assumption of coulomb friction was generally used in the theoretical analyses described above, but more recent studies demonstrated how it is not an

accurate representation of real behavior [Mokha et al., 1990]. The most common materials used for sliding bearings are unfilled or filled Polytetrafluoroethylene (PTFE, or Teflon) on stainless steel. Recently PTFE has been replaced with high strength polymer, which has better mechanics and dissipative characteristics.

3.1. Basic Principles of solid Friction

The utilization of the frictional behavior for sliding bearings requires the introduction of the basic mechanism of this phenomenon in order to gain an insight into the relevant aspect in seismic applications with sliding bearings. This requires that an understanding of the origin of friction in these interfaces is developed in order to provide a complete presentation and a base for the good interpretation of the results introduced in this dissertation.

This section presents a physical interpretation and the basic mechanism of the phenomenon of friction in selected sliding interfaces. It deals primarily with PTFE-stainless steel interfaces. The presentation is limited to certain aspects of frictional behavior that are relevant to the interpretation of experimental results at the macroscopic level.

Friction is the resistance to motion, which exist when a solid object is moved tangentially with respect to the surface of another that it touches. This dissertation aims at explaining the friction caused by sliding movements between solid bodies, which is called sliding solid friction. It also presents a description of the frictional behavior of sliding interfaces as they are used in sliding bearings for structural

applications. The frictional force, F, at the sliding interface of a bearing will be described with the classical law of friction of Coulomb:

$$F = \mu N \tag{3.1}$$

Where μ is the coefficient of friction and N is the normal load acting in the interface. By means of eq. (3.1) is possible define the static or breakaway coefficient of friction as the ration F/N, which is different respect the sliding coefficient of friction that occurs during the motion between two sliding surfaces.

The equation (3.1) postulates a friction coefficient directly proportional to the normal force N, and independent of sliding velocity and apparent contact area. Whereas these laws are valid in many cases, they do not, in general if applied to sliding surfaces. So for sliding bearing the friction coefficient is dependent on the velocity of sliding and apparent pressure.

3.1.1. Basic Mechanisms

To gain an understanding of the basic mechanisms of friction it is important to describe the microscopic events that cause friction. For this purpose here is reported an overview of the microscopic aspects of friction, this is limited to the events that may provide physical insight into the frictional behavior of sliding bearings [Bowden and Tabor, 1950, 1964, 1973].

Various mechanisms of friction have been proposed over the past years. It is believed that all these mechanisms contribute in the generation of friction in various degrees depending on the particular situation.

The origin and magnitude of the frictional force is given from the “adhesion theory”. This consider the intimate atomic bonds that interacts when two solid material are placed in contact (Figure 22).

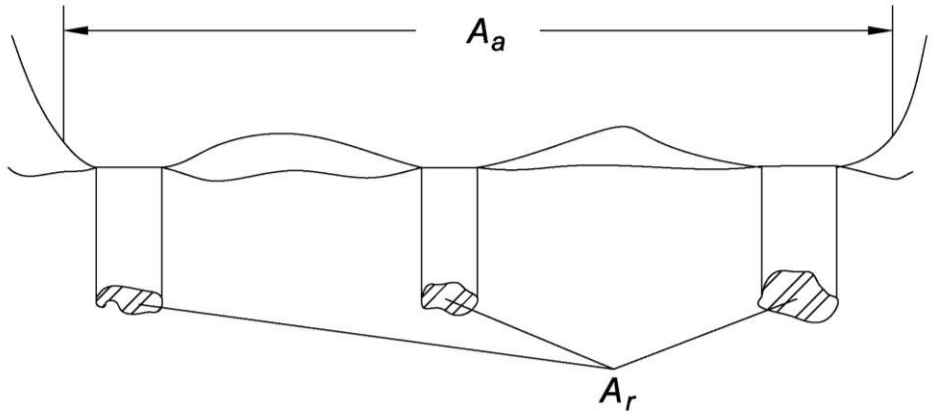

Figure 22: Schematic illustration of an interface, showing the apparent and real areas of contact.

Some regions on their surface will be very close together in some regions called "*junctions"* and the sum of the areas of all the junctions constitutes the real area of contact A_r. The total interfacial area consists of the area of contact and also of those regions denoted as the apparent area of contact, A_a. When the two surfaces are pressed together by a load, sliding is induced the frictional force is given by the product of the real area of contact, A_r, and the shear strength of the junctions, s:

$$F = sA_r \tag{3.2}$$

Although, a discreet number of frictional phenomena are explained by the postulate mentioned above, friction mechanism presents some criticisms and limitations and still now it is generally recognized that adhesion does not provide a clearly separate contribution of friction.

Although, the main resistance to sliding arises from the need to shear of adherent surface atoms, there are a number of other factors to be taken into account. These components will be described below.

Roughness component: a contribution is given by the roughness component, which arises from the need, during the sliding of rough surfaces, to lift one surface over the roughness of the others. If we call the asperity θ a contribution of the friction will be produced. However, if we consider a plane surface, during the motion there may be negative as well as positive values of θ. Summing up for all the contacts, the roughness friction contribution tend to zero and the remain contribution is about 0.05 to the overall friction coefficient.

Figure 23: Schematic illustration of the roughness of sliding surface. Positive and negative θ coexist.

The plowing component. when a hard surface has a sharp asperity and it slides over a soft surface, it will tend to dig into the softer surface and produce a plastic deformation. The energy of deformation represented by the groove must be supplied by the friction force, which will have the plowing contribution. Considering a simple calculation with a circular cone asperity dig into a softer surface as schematically illustrated in Figure 24. During sliding, the penetrated area A_p is given by

$$A_p = \frac{1}{2} 2r \cdot r \tan\theta = r^2 \tan\theta \tag{3.3}$$

Therefore the frictional force will be

$$F = \pi r^2 s + r^2 \tan\theta \, p \tag{3.4}$$

Where $p = \frac{L}{\pi r^2}$ represents the pressure in the junction.

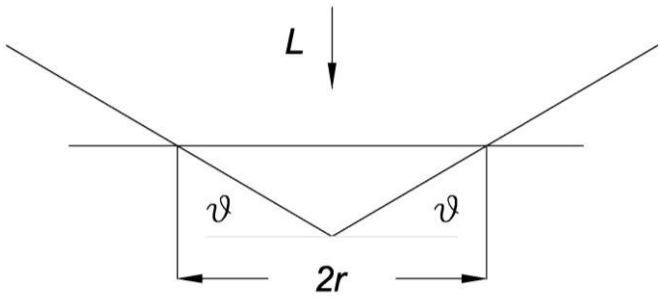

Figure 24: Schematic illustration of a cone pressed into a flat surface. The asperity moving horizontally create a groove which is swept out of A_p.

Third body effects: wear debris and contaminants at the sliding interface contribute an additional term to the friction force. The contribution is due to plastic deformation as agglomerates of debris and contaminants roll between the surfaces or as they indent these surfaces.

Viscoelastic Effect: polymers, such as PTFE, exhibit viscoelastic behavior. As asperities of a harder material slides over a viscoelastic material, energy is dissipated due to viscoelastic deformation, contributing thus an additional component to friction.

In general, it is believed that several mechanisms contribute to friction. Their relative roles are the subject of much debate. However, we shall recognize that adhesion and mechanical deformation (elastic, plastic or viscoelastic) are collectively responsible for friction. Moreover, we shall recognize that the real

area of contact is of paramount importance in the qualitative description of friction at the macroscopic scale.

3.1.2. Static and Sliding Friction

The static or breakaway friction is the maximum force, which exists to start a macroscopic motion in a solid. The breakaway frictional force decreases, when compare to the sliding frictional force, when macroscopic motion occurs. It is noticed from experimental results that the static friction is higher than the sliding friction force. Figure 25 illustrates a schematic test of a friction pendulum device, in which the low friction material that interfaces the stainless steel concave surface is an un-lubricated polymer composite with about 400 MPa compressive yield strength. The interface was at constant average pressure of 15 MPa. A cycle of sinusoidal motion with a pick velocity of 1.27 (mm/sec) was imposed. The different between the static and sliding values of the coefficient of friction is relevant.

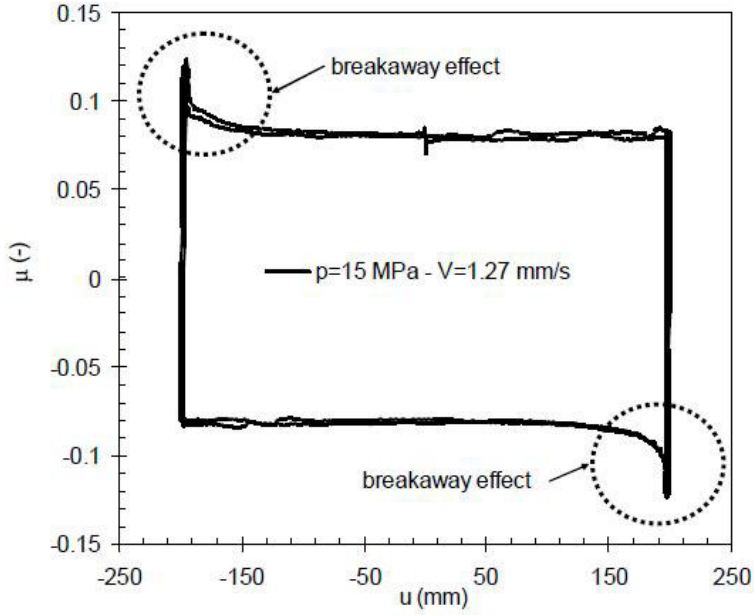

Figure 25: Typical Friction Force-Sliding Loop of Polymer-Stainless Steel Interface without the contribution of restoring stiffness W/R (Pressure=15 MPa, Peak Velocity=1.27 mm/sec).

3.1.3. Stick Slip

The Stick Slip phenomenon is a common experience in the sliding on one body over another under the effect of a continue force, and sometimes at constant or close to constant velocity. In displacement controlled testing of a sliding bearing (i.e., motion is imposed by an actuator and measurement of the friction force is made), stick-slip behavior is manifested as fluctuation in the recorded friction force versus time. Conversely, in a force controlled test the behavior is manifested as motion with stops. Stick-slip may be an intrinsic property of the sliding interface or more often is the result of inertia effects and the flexibility in

the testing arrangement, although the phenomenon may be aggravated by the frictional behavior of the interface.

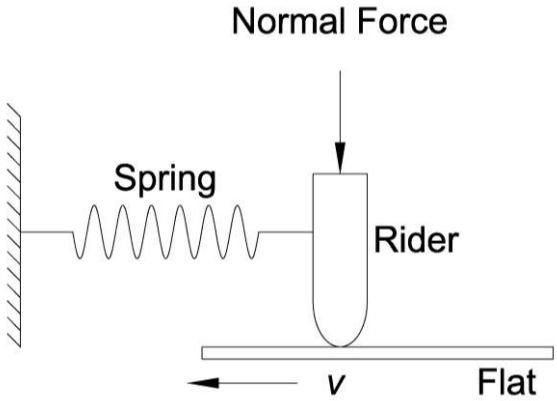

Figure 26: Schematic representation of a friction apparatus.

The Stick Slip phenomenon could be explained considering the sliding situation represented in Figure 26, in which a rider is fixed to a support by means of a spring and posed on a surface in motion under a constant velocity v. It is supposed that the velocity is low so that the rider keeps up with the movement of the flat and the damping is consequently negligible. Supposing a friction force displacement plot as shown in Figure 27a if we start the run at A the rider will move over the flat maintaining a constant velocity v. This phase is steady until the point B is reached. At this point the frictional force drops abruptly and the rider tries to adjust its position following the force-displacement function of the spring. The discrepancy created between the straight line of slope k and the friction force is highlighted with a dashed area. This portion has the dimension of energy, and it represents excess energy in the system, which becomes potential energy for the movement of the rider. The body then slips until it reaches the point C, where until

all the kinetic energy has been used. The spring force at this point is below the friction force, so that the rider will stick to the flat and it will be dragged along by it until the point D, where the friction force is large again to initiate relative motion again. In Figure 27b it is plotted the friction force as a function of time. The path denoted an irregular stick slip and occur really frequently with the sliding of clean metals, and the sliding of metals covered with a partially worn away solid film lubricant. In the first case the stick slip is basically due to the coalescence of the area contact's junctions in a larger junction, creating a severe fluctuation of the frictional force. In the second case the fluctuation arise because the rider proceeds alternately areas covered by the film and regions, in which the film is absent or worn.

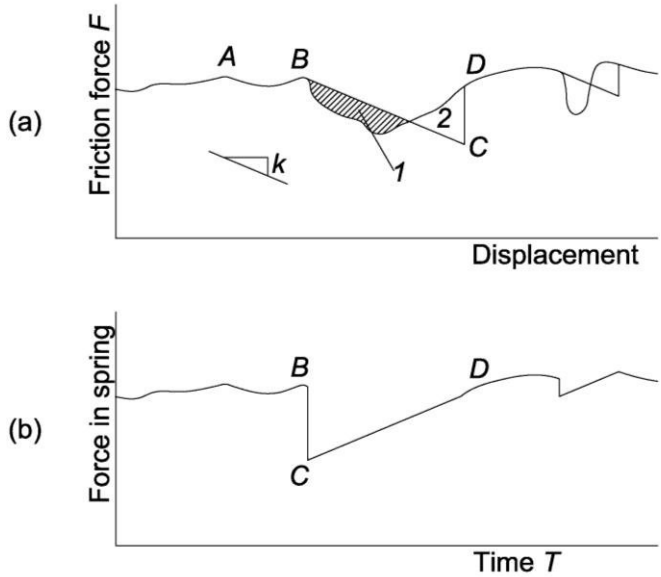

Figure 27: (a) A schematic hypothetical force displacement plot. (b) Friction record corresponding the force displacement plot.

3.2. Frictional behavior in PTFE-Polished Stainless Steel Interfaces

. The PTFE is a synthetic fluoro-polymer of tetrafluoroethylene, which is well known as the brand name Teflon by DuPont Co.

This material finds numerous applications and PTFE or PTFE-based materials in contact with polished stainless steel represent, by far, one of the most frequently used interface in sliding bearings.

Friction in this kind of interface is basically the result of adhesion, where the contribution of plowing effect is not significant. In PTFE surfaces the sliding occurs only at the interface deviating from the tendency of others polymers to shear in their bulk (Tabor, 1981).

The shear strength is given, as first approximation, by a linear function of the actual pressure, which is the pressure over the real contact area (Tabor, 1981).

$$s = s_0 + \alpha p_r \tag{3.5}$$

then the coefficient is friction is given combining eq. (3.2) and eq. (3.5)

$$\mu = \frac{F}{N} = \frac{(s_0 + \alpha p_r)A_r}{p_r A_r} = \frac{s_0}{p_r} + \alpha \tag{3.6}$$

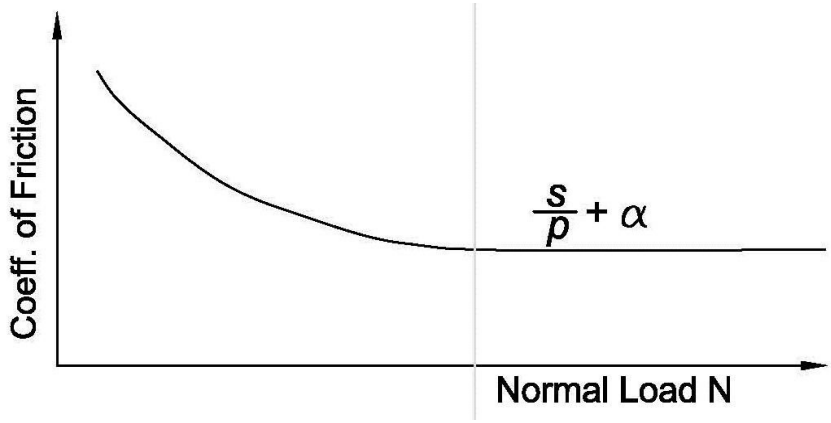

Figure 28: Schematic variation of Real Area of contact, Pressure and Coefficient of Sliding Friction.

The reduction in the coefficient of friction with increasing normal load is illustrated in figure 28.

PTFE is a viscoelastic material and it is subjected to creep, therefore to the real area of contact and as a result the motion depends on the load dwell (Bowden and Tabor, 1964).

The experiments conducted by many groups demonstrated increases in both the real area of contact and the static friction force over loading times. Testing of PTFE sliding bearings for the effect of load dwell has been conducted over a long time Paynter (1973), Campbell and Kong (1987) and Mokha et al. (1990).

The results of these studies could be briefly summarized with the following points:

The results on the static friction exhibit fluctuations that cannot be correlated to the load dwell. Rather, it was observed that static friction is higher in the first test conducted on a new specimen regardless of the load dwell. The static friction is lower in any subsequent test, again regardless of the load dwell. This may be

explained by the existence of a film of PTFE on the stainless steel surface ,which was deposit in the previous tests.

The time dependent deformation of PTFE is nearly completed within a very short time interval, likely of the order of a few minutes or hours, resulting in a constant real area of contact. As discussed earlier the experimental results on the dependency of the low velocity friction on normal load suggest that the real area of contact is approximately equal to the apparent area of the bearing Mokha et al. (1988). One explanation of these may be found by investigating the rate of deformation of PTFE under conditions of confined compression. Shames and Cozzarelli, (1992), demonstrated that confined PTFE creeps at very fast rate. It is thus likely that the condition of the real area of contact being approximately equal to the apparent area of the bearing is reached within very short time.

3.3. Single Pendulum System

In recent years, the use of concave sliding isolators (Friction Pendulum) for the seismic protection of buildings and bridges experienced a significant world-wide spread. The capability to undergo large displacements despite their compact size make these devices competitive among other commonly used isolation devices such as lead-rubber bearings or high dumping rubber bearing.

Concave sliding bearings are suitable for a wide range of applications for buildings, bridges and industrial facilities, due to their relevant features. Compared with High Damping Rubber Bearings (HDRB) and Lead Rubber Bearings (LRB), they offer a quite compact shape, with considerably lower thickness, and larger displacement capacity, these characteristics are very desirable for installation in

existing structures. Moreover, the natural vibration frequency of the structure depends only on the sliding surface radius and not on the supported mass. The seismic retrofit of the historic U.S. Court of Appeals building in San Francisco, damaged during the Loma Prieta earthquake in 1989 and retrofitted using 256 Friction Pendulum System (FPS) isolators, the San Francisco Airport International Terminal considered the largest isolated building in the world and the Benicia-Martinez Bridge retrofitted using 24 FPS isolators can be considered among the most important applications of this technology.

FPS have been recently used in Italy for the construction of approximately 4600 apartments to recover the homeless after the April 2009 earthquake in L'Aquila. The new buildings have been erected on a reinforced concrete slab, which supported by 40 steel columns provided on the top with seismic isolators (Figure 29). Considerable literature on experimental and analytical analyses of these devices is available, and in these section it is briefly reported.

Figure 29: A single pendulum bearing in situ. In this installation the sliding surface is faced down.

According to the simplified analytical model of the predominantly bilinear behavior of sliding concave isolators, developed by Zayas et al. (1989, 1990), the

force-displacement relationship based on the horizontal force balance is expressed as:

$$F = \frac{W}{R}u + \text{sign}(v)\mu W \tag{3.7}$$

where W represents the applied vertical load, μ the horizontal relative displacement between slider and concave base, v the velocity, R the radius of the concave surface, μ is the friction coefficient of the sliding system and F is the horizontal restoring force.

Equation (3.7) is derived from the equilibrium of forces presented in Figure 30, in which are represented the theoretical sliding concave behavior and the force-displacement loop under a constant vertical load W with a constant coefficient of friction μ.

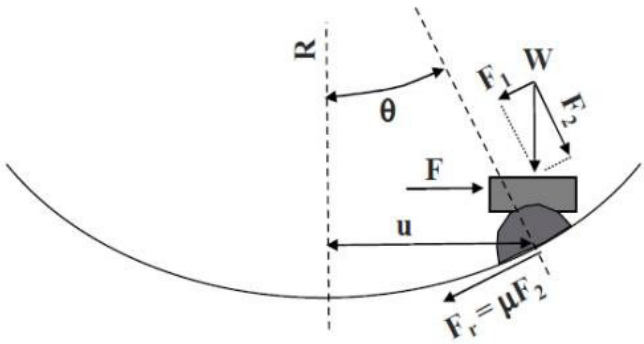

Figure 30: Theoretical sliding concave behavior and equilibrium of the forces involved during the motion.

As depicted in Figure 31 the frictional force of the device is partially given by the force due to the frictional behavior of the contact surfaces between the steel

concave surface and the slider. The rest of the force is provided by a component called “restoring stiffness”.

$$K_{ra} = \frac{W}{R} \tag{3.8}$$

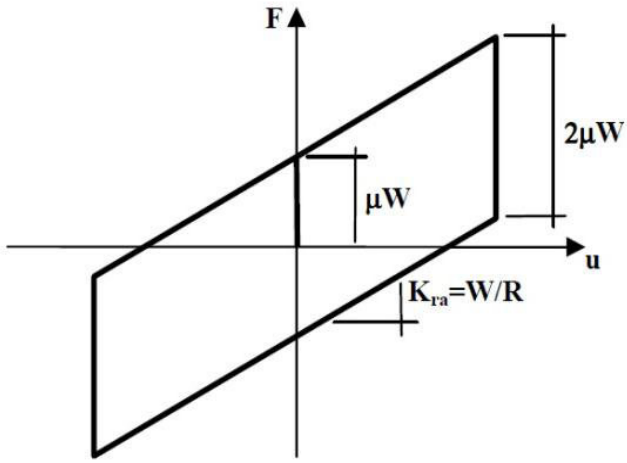

Figure 31: Typical bilinear force-displacement loop for a sliding concave device.

The stiffness of this single pendulum is directly proportional to the supported weight W (see eq.(3.8)). This aspect is an important and unique property of the FPS and it has advantageous effect on the torsion response of the structure.

After recent studies carried out from many research groups [Mokha et al. 1990, Bondonet and Andre Filiatrault, 1997, Dolce et al. 2005] on PTFE-stainless steel contact surfaces, it has been demonstrated that, due to the non linear relationship between coefficient of friction and weight supported by the isolator, the center of rigidity is eccentric, laying in the direction of the lightest portion of

the structure. So in the design of friction pendulum system is necessary to avoid an irregular distribution of weight on the superstructure in order to avoid unexpected torsional effects.

.

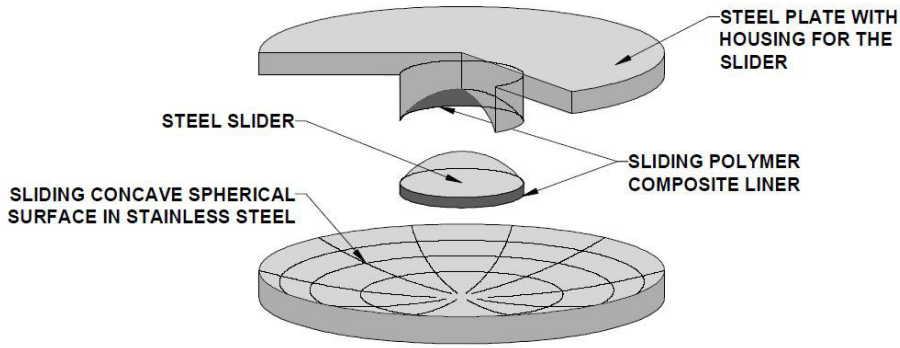

Figure 32: Schematic of concave sliding bearing [44].

An important property of the FPB is the unique design of the articulated slider (Figure 32). It is designed as a semispherical shape with an internal constant radius of curvature. As regards the sliding part, this has the same radius of curvature R of the steel sliding surface with the purpose of guarantee a uniform contact pressures between the slider and the concave surface for any combination of lateral and vertical loads.

The period is independent of the structure mass in the FP, making it a unique device among the SRMD. The flexibility of FPS connections consist of varying the sliding period and friction coefficient simply choosing the radius of curvature of the concave surface, or design sliding polymer composite liner (Figure 32) such as to obtain the desired friction coefficient. The period does not change if the structure weight is different than that assumed (2.49).

This frictional interface also generates a dynamic friction force that acts as a damping system in the event of an earthquake. This lateral displacement greatly reduces the forces transmitted to the structure even during strong magnitude earthquakes. This type of system also possesses a re-centering capability, which allows the structure to center itself by the concave surface of the bearings and gravity, if any displacement occurs during a seismic event.

3.4. Examples of Seismic Isolation with friction pendulum system

San Francisco's International Airport Terminal was designed to resist a magnitude 8 earthquake that could occur because of the San Andreas fault. The 267 Friction Pendulum bearings protect this building from the severe ground shaking that occurs during major earthquakes.

Figure 33: The arrangement of the Friction Pendulum during the construction phases of San Francisco's International Airport, www.earthquakeprotection.com.

The isolated system provides a 3 seconds isolated period, it also reduces earthquake force exerted on the building by 70%. Each bearing can displace up to 20 inches (50.8 cm) in any direction while supporting loads of up to 6 million pounds (~27 MN). Seismic isolation provideds the lowest construction cost, still achieving the desired seismic performance. Moreover, the use of friction Pendulum bearings as compared to rubber bearings, allowed a reduction of column and bean sizes, and saved an additional amount of structural steel, and this construction cost.

Another important and well-known place where FPS has been put in used is in the retrofitting of U.S. Court of Appeals in San Francisco (see Figure 6). This is a 350,000 sq ft building listed in the National Register of Historic Places. A total of 256 Friction Pendulum, installed between the existing foundation and columns, make the structure one of the largest seismically isolated buildings in the United States. Engineering analyses and testing show that the isolators reduce the seismic loads caused by a magnitude 8 earthquake by 80 %. These reductions in seismic loads and drift protect the historic architectural finishes and structure from earthquake damage. Built in 1905, the main building consists of a steel frame with un-reinforced granite masonry clay tile. The building has intricate granite exterior, interiors of marble, decorative plaster and hardwoods, and hand painted murals make this building one of the most decorated Federal building in West America. The structure was damaged in the 1989 Loma Prieta earthquake, and was immediately closed. Different proposals were submitted by suppliers of Lead-Rubber bearings, High dampening Rubber hearings, and Friction Pendulum Bearings in order provide a seismic rehabilitation to repair the damage and protect the structure from future earthquakes. After detailed engineering studies, the

Friction Pendulum Bearings were found to more effectively enhance the building's seismic performance.

Figure 34: A view of the Friction Pendulum Bearing used in U.S. Court of Appeals in San Francisco retrofitting [source: www.vsl.com].

Greater reductions in seismic shear forces were achieved, with practical size hearings. The smaller size bearings, and practical installation details, reduced the installed costs by allowing the existing footings and columns to he used with minimum changes.

The isolators reduce the earthquake forces on the structure by deflection (via pendulum motion) and by absorbing the energy of the earthquake (via friction). Extensive testing carried out at the National Center for Earthquake Engineering Research supported the performance of the bearings. State University of New

York at Buffalo and at the Earthquake Engineering Research Center, University of California at Berkeley.

3.5. Friction coefficient: Effect of Apparent Pressure and Sliding Velocity

First studies about the friction pendulum devices have been carried out since 1987 (Zayas 1987, Mostaghel and Khodaverdian 1987, Fan et al. 1988). These theoretical pioneer works evaluated the seismic performance of sliding isolation system demonstrating the feasibility of these devices. In these first studies, friction coefficient have been evaluated accordingly with the simplified Coulomb model, in which the force of friction is directly proportional to the applied load, independent of the apparent area of contact and of the sliding velocity. These assumptions lead to a rectangular friction coefficient-displacement loop, independent from the level of applied load.

In the literature there is few data on the frictional properties of PTFE bearings at large sliding velocities. Tyler (1977) was the first to report such data and focused his study on the breakaway friction under high rate of motion, he also reported data on the sliding friction. These data are in general agreement with the data of Mokha et al. [48] who conducted tests for a wider range of conditions.

Mokha et al. [48] conducted a series of test on sheet type Teflon (PTFE) sliding bearing, obtaining measurements of the breakaway (static) and sliding (kinetic) coefficients of friction. They noticed that the results of these experiments were in disagreement with the theoretical studied conducted before. Their analysis

of the shape of the loops indicated major effects related to the frictional performance of the devices that generated distortion of the Coulomb's rectangular loop.

The developed model of friction studied by Mokha [48] exhibits a behavior that deviates significantly from that of Coulomb. Results show that under certain conditions the Coulomb's model may provide reliable estimates of the forces imparted to the isolated structure.

The first characteristic of this model is the dependency of the frictional force on the velocity of sliding. Other features of this model are the dependency of the frictional force on bearing pressure and condition of interface (type of Teflon and roughness of stainless steel).

Furthermore, the effect of breakaway friction on the behavior of sliding isolation systems is assessed. At initiation of sliding, the structure is subjected to high frictional forces. These forces are significant for sliding systems for which the Teflon-steel interfaces operate at low velocity.

The series of test conducted by Mokha et al. were carried out with sliding surfaces composed with unfilled or glass filled PTFE with 15% and 25% of the weight, and in contact with polished ASTM A240 type 304 polished stainless steel, having a roughness surface between 0.03 μm and 0.04 μm. Bearing pressure at the interface was ranging between 6.9 to 44.9 MPa. Motion at the interface was either sinusoidal or with constant velocity, where the peak value of sliding velocity was between 0.25 and 50 cm/s.

First observations on the friction behavior were made with this experimental test, and they are summarized below:

- The breakaway and sliding friction coefficient are related with the bearing pressure and the condition of the interface.
- The sliding value of the coefficient of friction increases with an increase in the sliding velocity
- Breakaway friction coefficient is substantially larger than the sliding value.
- Interfaces subjected by a run, show a lower breakaway coefficient in subsequent test. This may be explained by the existence of a film of PTFE on the stainless steel surface which was deposit in the previous tests
- The effect of acceleration of sliding at the interfaces is minimal.

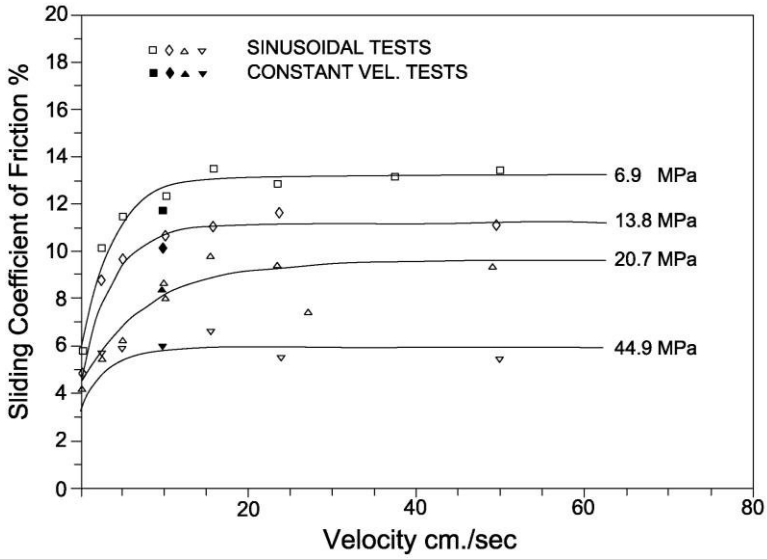

Figure 35: Variation of Sliding Coefficient of Friction with velocity of glass-filled PTFE for different pressure values [48].

In Figure 35 it is shown the sliding coefficient of friction upon division by the breakaway friction coefficient as function of sliding velocity. Mokha proposes the following equation for approximate the experimental data,

$$\mu_s = f_{max} - Df \exp(-a|\dot{u}|) \tag{3.9}$$

Where f_{max} represents the coefficient of friction at high velocity of sliding, Df the difference between f_{max} and the sliding value at very low velocity while a is a constant related with the bearing pressure and condition of interface.

The frictional force, F_f, at a sliding interface, could be described with this equation:

$$F_f = \mu_s W \operatorname{sgn}(\dot{u}) \tag{3.10}$$

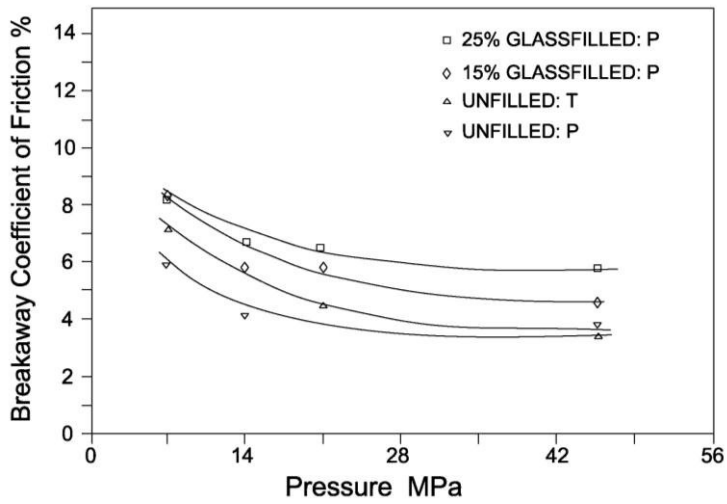

Figure 36: Effect of beating pressure on Breakaway coefficient of Friction for glassfilled and unfilled PTFE stainless steel surfaces [Mokha et al., 1990].

Mokha noticed and confirmed experimentally the theoretical studies of Tabor [73] (see section 3.2, equation (3.6)). In Figure 35 and in Figure 36 it is clear how the coefficient of sliding friction decreases with increasing pressure. Moreover, the rate of reduction of the sliding coefficient of friction with increasing pressure has a strong correlation with the sliding velocity. As illustrated in Figure 36, breakaway coefficient of friction reduces its modulus with increasing pressure.

Frictional properties of the PTFE composite used in FPS bearing have been studied by Constantinou et al. [25] and Tsopelas et al. [75]. The values of the sliding coefficient of friction were obtained in shake table testing of a bridge model with either FPS bearings (Constantinou et al., 1993) or with flat sliding bearings (Tsopelas et al., 1994). The data were extracted from either displacement controlled tests (open circle and square symbols, Figure 37) or seismic motion tests (dark symbols, Figure 37).

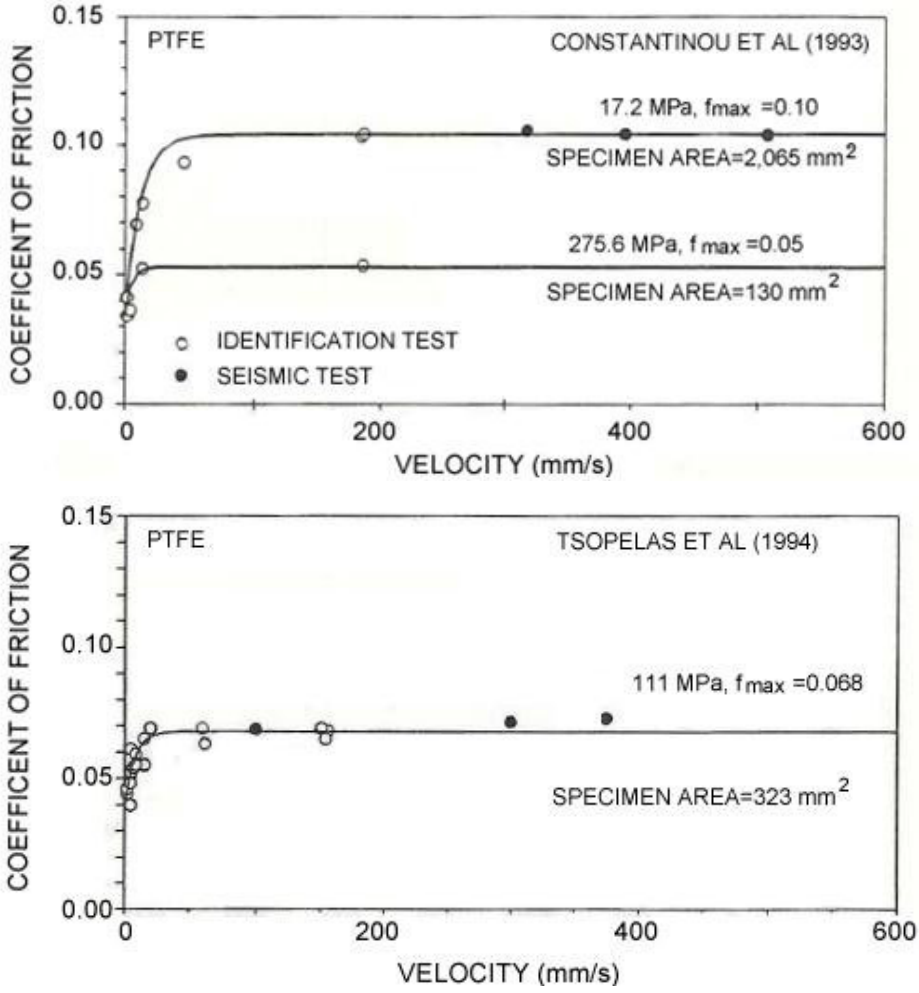

Figure 37: Coefficient of Sliding Friction of Unfilled PTFE-Polished Stainless Steel Interfaces [25].

In general, for a fixed value of the apparent pressure the sliding coefficient of friction, depends on the velocity, v, in a relation that can be described by eq. (3.9)

[48]. Figure 37 describes the observed dependency of the sliding coefficient of friction on velocity.

Parameters of eq.(3.9) control the transition of the coefficient of friction from its minimum value to its maximum value at high velocity of sliding. Figure 38 illustrates the effect of parameter a for two values of the ratio f_{max}/f_{min}, 2.5 and 5.

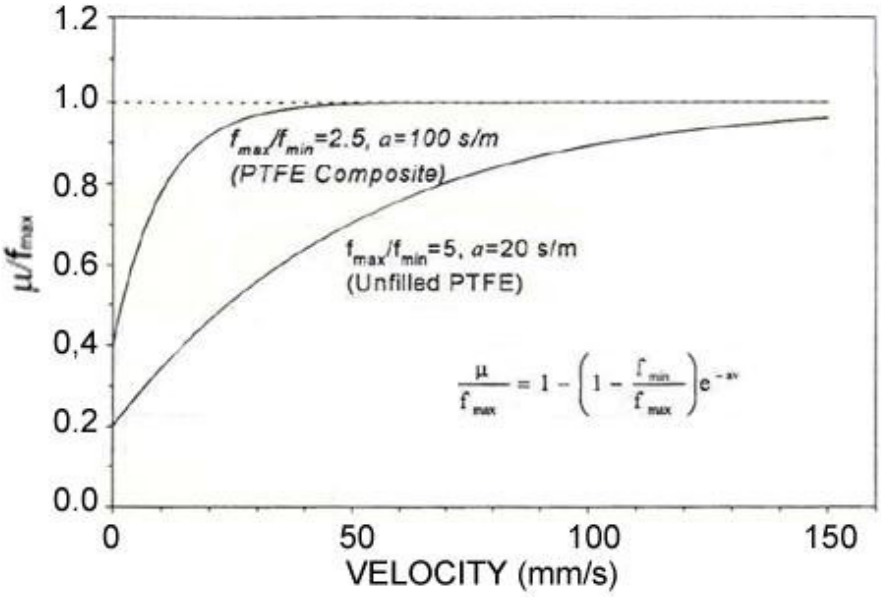

Figure 38: Schematic illustration of the effect of parameter 'a' in the coefficient of Friction with velocity [25].

Recently Bondonet and Andre Filiatrault [11] conducted experimental tests to evaluate the frictional response of PTFE Sliding Bearing at high frequencies.

Sinusoidal tests were done on sheet-type Teflon- stainless steel interfaces at bearing pressures of 5, 15, 30, and 45 MPa, at frequencies of 0.02, 0.2, 1.0, 2.0,

and 5.0 Hz, and at displacement amplitudes of ± 10 mm and ±70 mm. A maximum sliding velocity of 82 cm/s was reached during the tests. The steel portion of the interface was made of stainless steel plates, 1.6 mm thick, which were welded on 10mm mild steel plates. A grade-eight mirror finish was used for the stainless steel. The direction of the predominant surface pattern (surface lays) was parallel to the excitation direction in all tests. The PTFE portion of the interface was made of Teflon disks having a diameter of 128 mm and a thickness of 5 mm. Three different types of Teflon material were considered: unfilled Teflon, glass-filled Teflon at a composition of 15% per weight, and carbon-filled Teflon at a composition of 25% per weight.

The test showed a reliable performance during the test series and the interfaces between glass-filled Teflon and carbon-filled Teflon exhibited minor damages in their surfaces. Only the unfilled surface suffered more damage under higher confining pressures between 30 and 45 MPa.

Two thermocouples were installed on the edges of the stainless steel plate for monitoring the variation of temperature during and after the tests. The rises of temperature are reported in Table 1.

Table 1: Maximum Temperatures Recorded.

Displacement [mm]	Teflon	Maximum Temperature [°C]
±70	unfilled	70
±70	15% glass filled	110
±70	25%carbon filled	130
±70	unfilled	<30
±70	15% glass filled	<30
±70	25% carbon filled	<30

The frictional response of the unfilled Teflon with 30 MPa of confining pressure is reported in Figure 39.

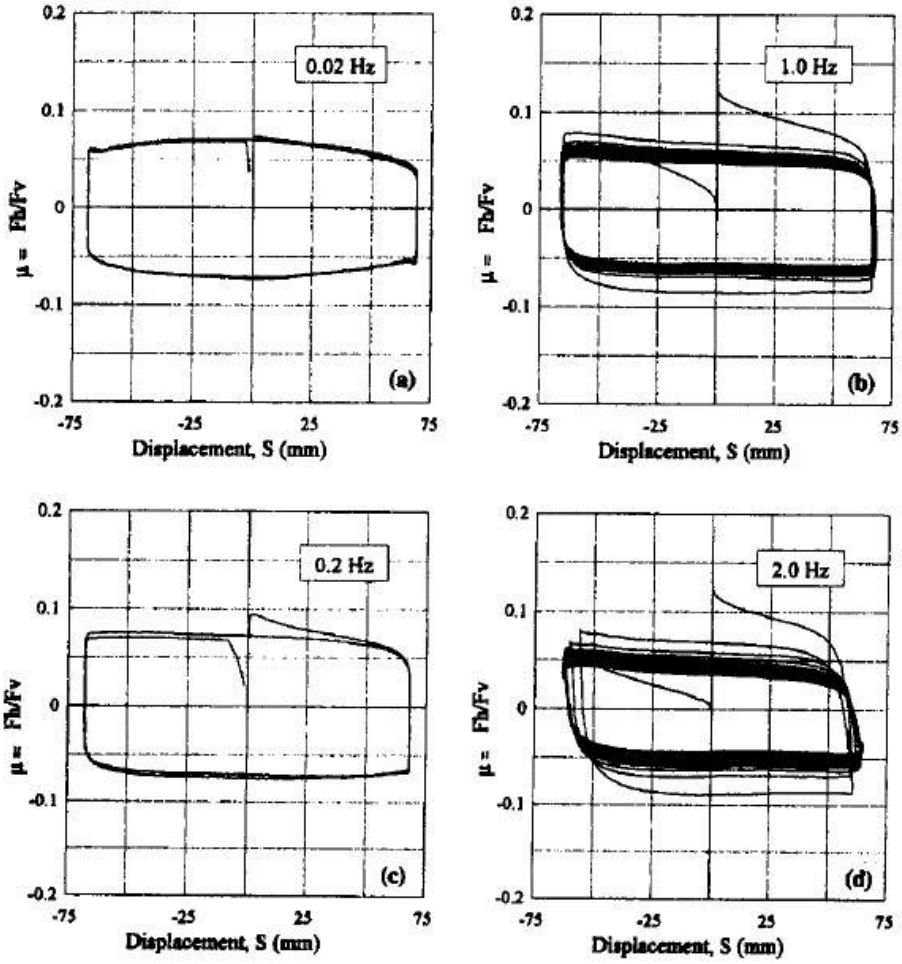

Figure 39: Experimental Hysteresis Loops for Unfilled Teflon under confining pressure of 30 MPa [11].

The friction coefficient depicted in figure 39 is given by the ration between the horizontal applied force, F_H, and the vertical force, F_v.

For each test it is clearly distinguished the initial coefficient of friction, μ_i, which occurs at the first peak of the first cycle when the frictional involved forces are under static conditions. In the experimental hysteresis loops for low excitation frequencies, the initial coefficient of friction it is almost equal to the steady state coefficient of friction, μ_{ss}, while for high frequencies a transient response is observed between μ_i and μ_{ss} and the gap value between the two coefficients of friction is significant.

In figure 40 is illustrated the variation of the initial coefficient of friction, μ_i, and the peak velocity impressed during the sinusoidal input. The experimental result could be direct with the eq (3.9) [48]:

$$\mu_{\mathrm{i}} = \mu_{\mathrm{i\,max}} - \left(\mu_{\mathrm{i\,max}} - \mu_{\mathrm{i\,min}}\right) e^{-\alpha_{\mathrm{i}} \left| \dot{S}_{\mathrm{max}} \right|} \tag{3.11}$$

The equation reveals the relation between velocity and coefficient of friction. In eq. (3.11) μ_{imin} and μ_{imax} represent the minimum and maximum initial coefficient of friction, while α_i it is an empirical exponential constant with units of inverse velocity.

The result reported in figure 40 presents the initial coefficient of friction tendency to decrease when the confining pressure increases. This is also shown in figure 41.

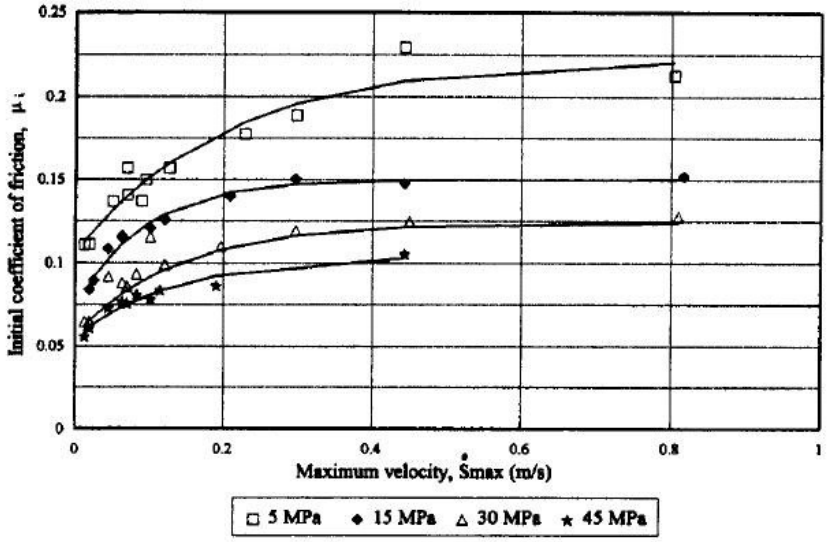

Figure 40: Variation of Initial Coefficient of Friction with Absolute Maximum Velocity [11].

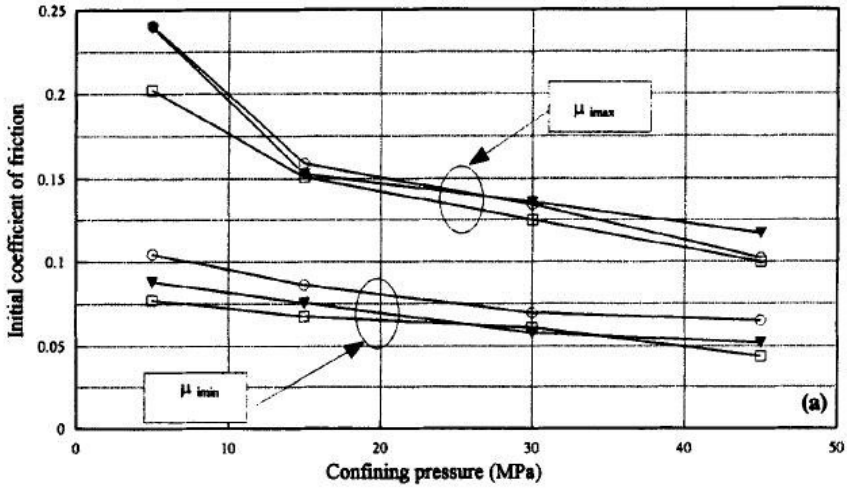

Figure 41: Influence of Confining Pressure on initial Coefficient of Friction [11].

In recent studies of Dolce, Cardone and Croatto [31] with a large experimental investigation on steel-PTFE interfaces, aimed at evaluating the effect of sliding velocity and contact pressure, proposed a calibrated mathematical models in order to validate the model proposed by Constantinou (1990). In that research more than 300 tests have been carried out on steel-PTFE interfaces with bearing pressures of 9.36, 18.72 and 28.1 MPa , varying temperatures of 10, 20 and 50° C, sliding velocities changing from 1 mm/s to about 300 mm/s, and displacements amplitudes ranging from 10 to 50 mm.

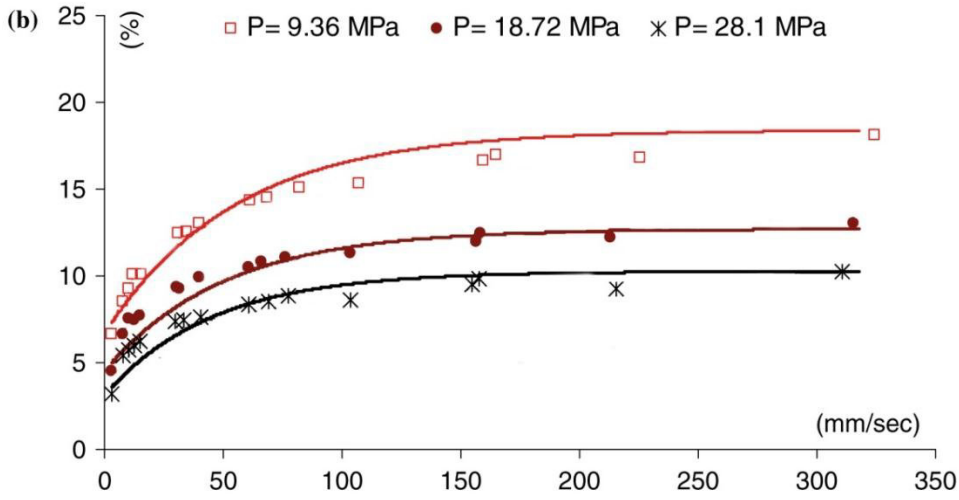

Figure 42: Variation of the friction coefficient with sliding velocity and bearing pressure. Comparison between analytical laws and experimental results.

Dolce et al. [31] pointed out that the sliding friction coefficient increases rapidly with velocity, up to a certain velocity value, beyond which it remains almost constant. In figure 42 it is shown how this value is around 150mm/s. From the same experimental picture it is also possible to evaluate the behavior of the

coefficient of friction versus the variation of contact pressure. As known from Mokha et al. the sliding friction coefficient of steel PTFE interfaces reduces while increasing pressure. The rate of reduction of the friction coefficient is practically constant and insensitive to sliding velocity.

3.6. Friction coefficient: Effect of Room Temperature

Campbell et al. [19] reported data on the effect of temperature on the breakaway and the low velocity sliding friction of un-lubricated unfilled, glass filled and PTFE in contact with highly polished stainless steel at apparent pressure of 20.7 MPa. Table 2 presents the results of Campbell et at. [19].

Table 2: Effect of the Bulk Temperature on the Breakaway and sliding coefficient of Friction.

Temperature °C	Breakaway Coefficient of Friction	Sliding Coefficient of friction V=1 mm/s
20	0.066	0.016
10	0.125	0.016
0	0.132	0.020
-10	0.149	0.039
-15	0.154	0.057
-20	0.136	0.074
-25	0.157	0.086

Constantinou et al. (1995) have conducted tests on unfilled PTFE and the PTFE composite over a wide range of sliding velocities and temperatures in the range of 50°C to -50°C. The tests were conducted at apparent pressure of 20.7

MPa for the unfilled PTFE and of 69 MPa for the PTFE composite. The stainless steel utilized in these tests was ASTM A240, Type 304 with a measured surface roughness of 0.03 μm.

Figure 43 presents the measured breakaway friction, the minimum sliding friction, f_{min}, and the sliding friction at three different velocities, this as a function of the temperature at the start of each experiment. Figure 43 demonstrates the substantial effect of temperature on the low velocity, f_{min}, and breakaway friction and the much less effect on the high velocity friction. The values of friction in this figure are consistent with those reported by Campbell et al. [19] (see Table 2).

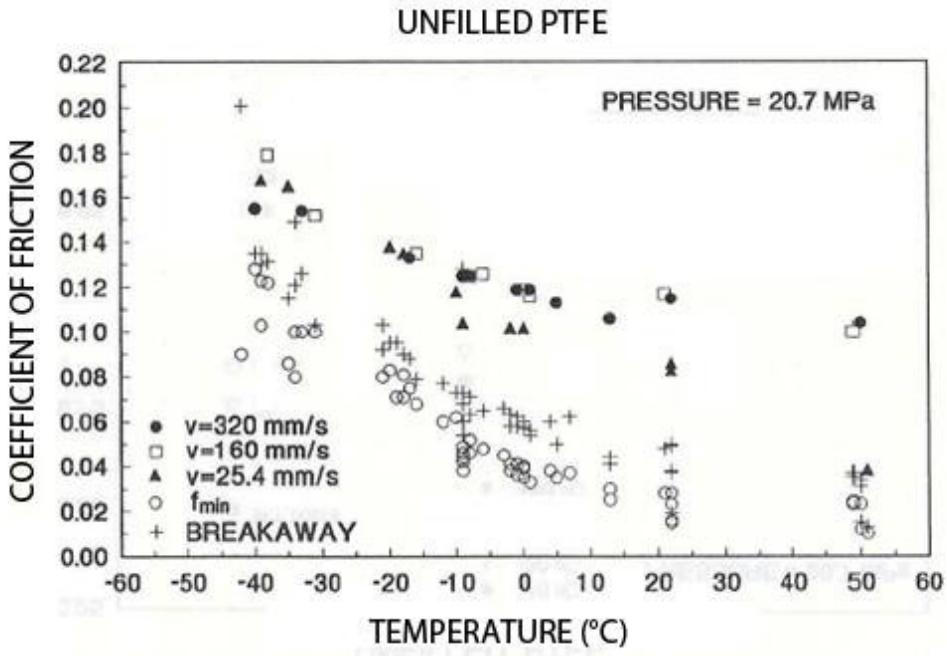

Figure 43: Friction PTFE-based composite-Polished stainless Steel Interfaces as Function of Bulk Temperature [Constantinou et al., 2005].

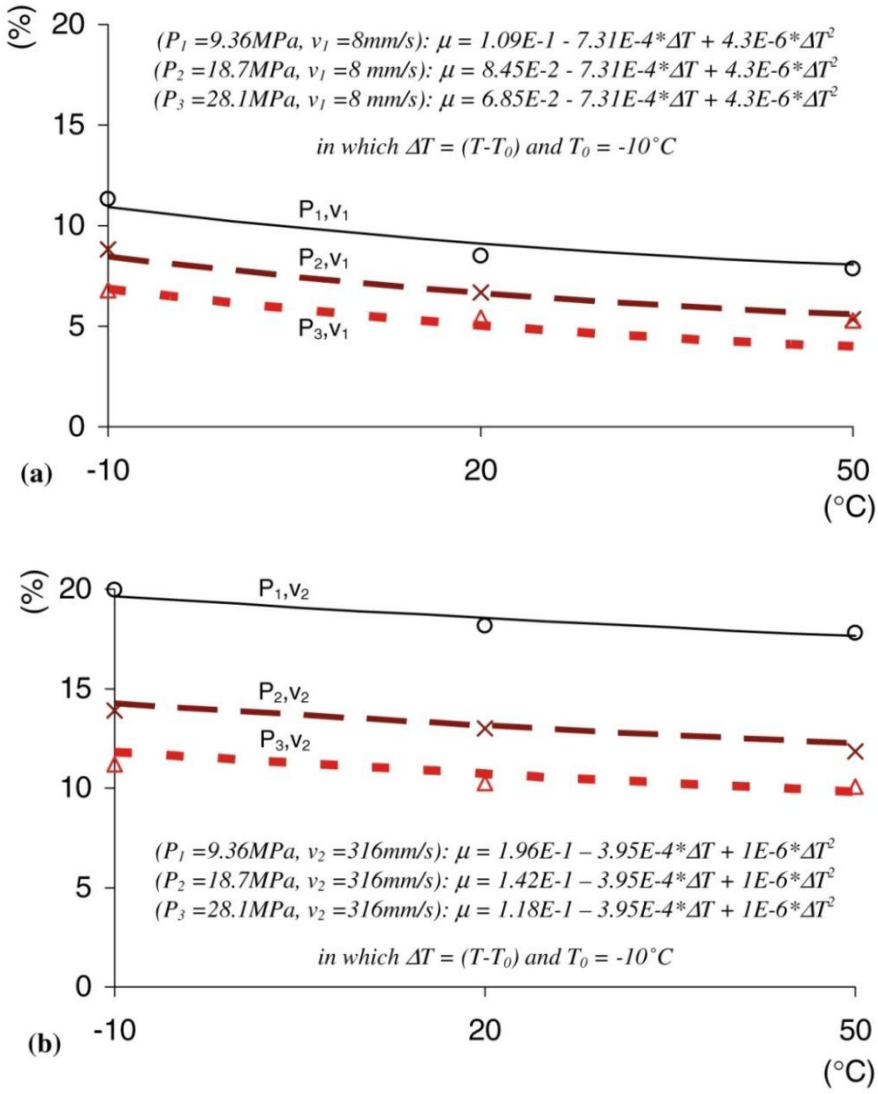

Figure 44: Sliding friction coefficient at (a) very low and (b) very high velocities (i.e. 8 and 316 mm/s, respectively) as function of air temperature, for three different normal pressure values (i.e. 9.36, 18.72 and 28.1 MPa, respectively). Comparison between experimental results and model predictions. [Dolce et al., 2005].

As mentioned in the previous section, Dolce et al. [31], with a large experimental investigation on steel-PTFE interfaces, studied the dependency of mechanical behavior of these devices considering even the effect of the air temperature. These result are shown in figure 44.

In figure 44 is reported the friction coefficient at very low (i.e. 8 mm/s) and very high (i.e. 316 mm/s) sliding velocities, as a function of air temperature, for three different contact pressure values. Dolce at al. provided a second-order polynomial law having the expression (3.12):

$$\mu = a \cdot T^2 - b \cdot T + c, \quad \text{with } a\ b\ c > 0 \tag{3.12}$$

Based on experimental results of Dolce et al., the sliding friction coefficient decreases when air temperature increases. The rate of reduction depends on the sliding velocity, while is almost independent from contact pressure (the three curves in figure 44 are likely parallel). Moreover, the sliding coefficient of friction results to be greater when passing from low to medium temperatures than when passing from medium to high temperatures. At 8 mm/s the average reduction from -10 to 20 °C is 0.77%/°C, while is 0.33%/°C when passing from 20 to 50°C.

The variation of air temperature influences the friction coefficient with respect to the reference temperature (20°C). The AASHTO defined two system property modification factor, $\lambda_{max,t} = 1.2$ and $\lambda_{min,t=2}$, which quantify the effects of temperature variations on the nominal value of the friction coefficient at 20°C reference temperature. They are defined as the ration of the friction coefficient at the highest and at the lowest expected temperature. Dolce et al. provided from the whole set of experimental data that the coefficients of friction are 1.17 and 0.89, respectively slightly different with the AASHTO estimations.

3.7. Friction coefficient: Recent studies on high strength *polymers stainless steel contact surfaces, effect of 'cycling effect'.*

Applications of exponential models in the analysis of a sliding isolation system have been reported in (Constantinou et al., [24]; Mokha et al., [50]; Deb and Paul, [44]), mainly with the scope of evaluating the effects of bearing pressure, sliding velocity, breakaway friction and bi-directional motion on the seismic response of base-isolated buildings.

A phenomenological model of practical use is able to represent the reduction of the friction developed by the sliding system along the travelled path (cycling effect) was still needed for design and assessment purposes.

In a study of 2012 carried out by Benzoni e Lomiento [44], a model that allows the prediction of the friction cyclic degradation, as well as the load and velocity effects, valid for low friction sliding devices was proposed.

The model of used to defined the friction coefficient is shown below,

$$\mu(W, T_f, v) = f_w(W) \cdot f_c(c) \cdot f_v(v) \tag{3.13}$$

where f_W, f_c and f_v are functions representing the dependency on the vertical applied load W (load effect), the cycling variable c (cycling effect), and instant-velocity v (velocity effect) respectively. In this study, each function has been defined and calibrated with experimental data. The devices were tested at the Caltrans SRMD Testing Facility at the University of California San Diego campus with full-scale experimental tests.

The SRMD testing facility consists of a 6 DOFs shake table specifically designed for full scale testing of isolators and energy dissipators [Benzoni and Seible, 1998].

The tests are divided in three categories: tests at low, medium and high vertical loads. Specifically, the vertical loads W of 3263 KN, 6525 KN and 13050 KN, were applied, corresponding to pressure values p of 15, 30 and 60 MPa, respectively.

For each set of loads, tests were completed at peak velocity V ranging from 0.254 mm/s to 800 mm/s. Two fully reversed sinusoidal cycles, with displacement amplitude D=200 mm were applied for all the tests.

To assess the relationship between applied vertical load (pressure) and friction coefficient, low velocity tests results were used in order to minimize the influence of velocity and cycling effects. In the proposed model, the load effect is expressed as function of the coefficient of friction coefficient μ_{s0}, the applied vertical load W and a load reference value W_{ref}:

$$f_w(W) = \mu_s e^{-W/W_{ref}} \tag{3.14}$$

The values of μ_{s0} and W_{ref} were determined with a least squares regression over the experimental coefficients of friction extracted from slow motion tests.

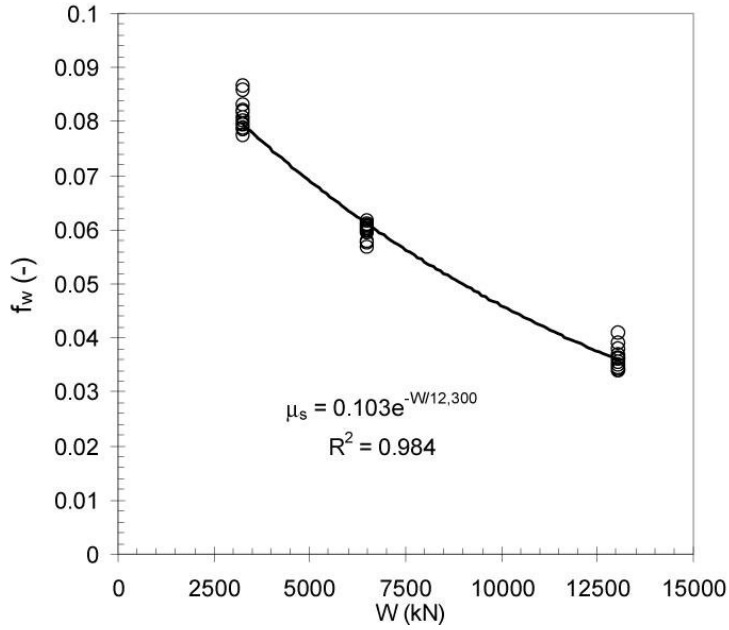

Figure 45: Variation of slow-velocity friction coefficient f_W with the appliet load W (Load effect) [Lomiento et al.. 2012].

A determination factor R^2=0.984 was found to predict the experimental values. For the particular data set, the value of μ_{s0} =0.103 and W_{ref}=12300 kN provided the best agreement between numerical and experimental results [44].

The effect of repetition of reversal motion consists in a progressive reduction of the coefficient of friction with distance traveled. A continuous drop of the kinetic friction coefficient was detected by Mokha et al. (1990) also for PTFE-steel sliding surfaces but not further investigated. The temperature rise is related to the heat flux generated by the frictional forces, equal to the power dissipated per unit area. For the sliding isolator the heat source is the contact surface between the slider and the sliding concave surface and the heat flux is expressed as:

(3.15) $$q = \frac{\mu W|v|}{\pi a^2}$$

where μ is friction coefficient, W is the applied load, v is the sliding velocity, and a is the radius of the contact surface, i.e. the radius of the slider. This heat flux varies in intensity and position during the sliding motion. For short duration motion, the temperature rise on the surface is directly related to the cumulative heat flux acting on the surface from the beginning of the sliding motion. During the time interval dt , the heat source moves from the position u to the position u + du , distributing its heat flux over the grey surface with area 2a · du represented in figure 46, which is a portion of the whole area πA^2 of the sliding surface. This statement assumes that the curvature radius of the concave sliding surface R is significantly greater than the radius A of the projection of the surface on the horizontal plan.

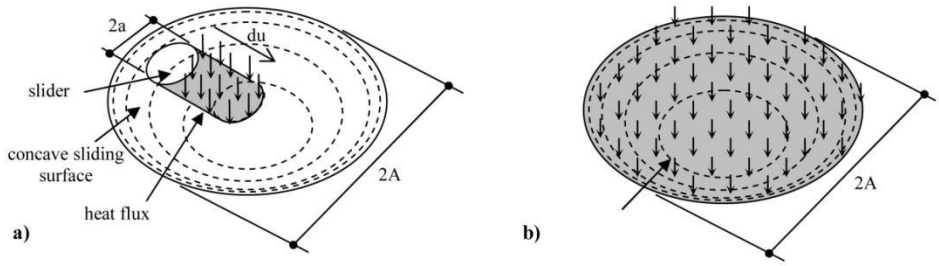

Figure 46: Actual (a) and equivalent uniformly distributed (b) heat flux in the time interval dt [44].

Being a quantity related to the whole sliding surface of the isolator, the uniformly distributed heat flux that crosses the surface during the time interval ($t-t_0$) can be cumulated as:

$$\bar{q} = \frac{2}{a\pi^2 A^2}\int_{t_0}^{t} \mu W v^2 dt \tag{3.16}$$

The cumulative uniformly distributed heat flux is dependent on the geometry of the isolator by means of the radius a of the slider, the radius A of the sliding surface, the applied vertical load W, the instant sliding velocity v, and the coefficient of friction μ. In order to describe the degradation of the friction coefficient with the temperature rise due to cycling, a new variable obtained by excluding μ from $q(t)$ was introduced by Lomiento et al. [44]:

$$f_c(c) = e^{-(c/c_{ref})^{\beta}} \tag{3.17}$$

where c_{ref} is a reference value of the parameter c and β represents the frictional degradation rate. The values c_{ref} and β were determined by means of a least squares regression on the experimental data. For the performed tests the values c_{ref}= 6600 kN/ms and β = 0.5 were identified.

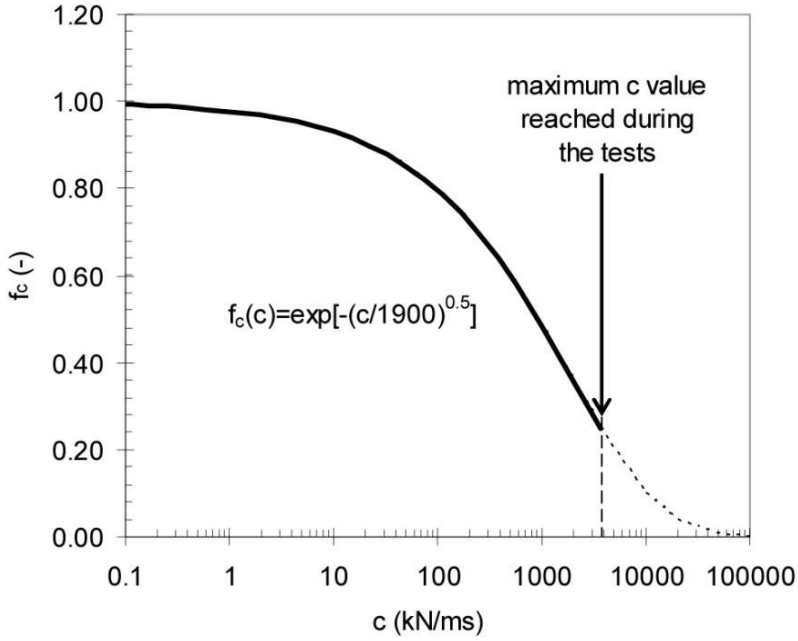

Figure 47: Reduction of the coefficient of friction predicted. [44]

Many research groups Mokha et al. 1990, Constantinou et al. 1990, Bondonee et al. 2002, Dolce et al. 2005] have documented an increment of the coefficient of friction with increasing sliding velocity, in the operational range of these devices. In his study Lomiento et al. (2012) correlated the experimental data with a method that allows to reduce the mentioned effects that concurs together to the assessment of the friction. Therefore the experimental data were opportunely processed in order to reduce the cross correlation between the variables.

Experimental data were well correlated with the exponential law:

$$f_v(c) = \gamma + (1-\gamma)e^{-|v|/v_{ref}} \tag{3.18}$$

where v is the sliding instant velocity, v_{ref} is a reference velocity, and $\gamma \geq 1$ express the ratio between the fast motion and the slow-motion coefficient of friction. The values $\gamma = 1.4$ and $v_{ref} = 10$ mm/s have been found to fit the experimental data.

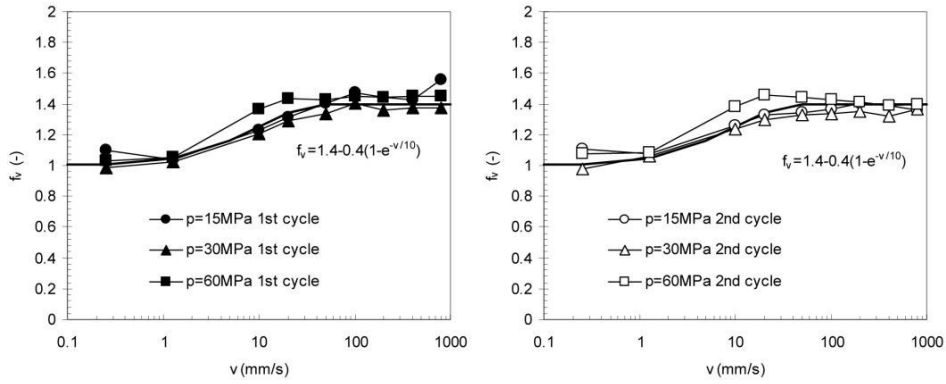

Figure 48: Variation of the coefficient of friction with the velocity v (velocity effect): a) 1st cycle, b) 2nd cycle [44].

The three functions previously defined were combined, through (3.18), and (3.14), into the proposed model of the friction parameter:

(3.19)

$$\mu(W, T_f, v) = f_w(W) \cdot f_T(T_f) \cdot f_v(v) = \mu_s e^{-W/W_{ref}} \cdot e^{-(c/c_{ref})^{\alpha}} \cdot \left[\gamma + (1-\gamma) e^{-|v|/v_{ref}}\right]$$

The experimental parameters were compared, and they are shown in figure 49 with coefficients of friction predicted by (3.19).

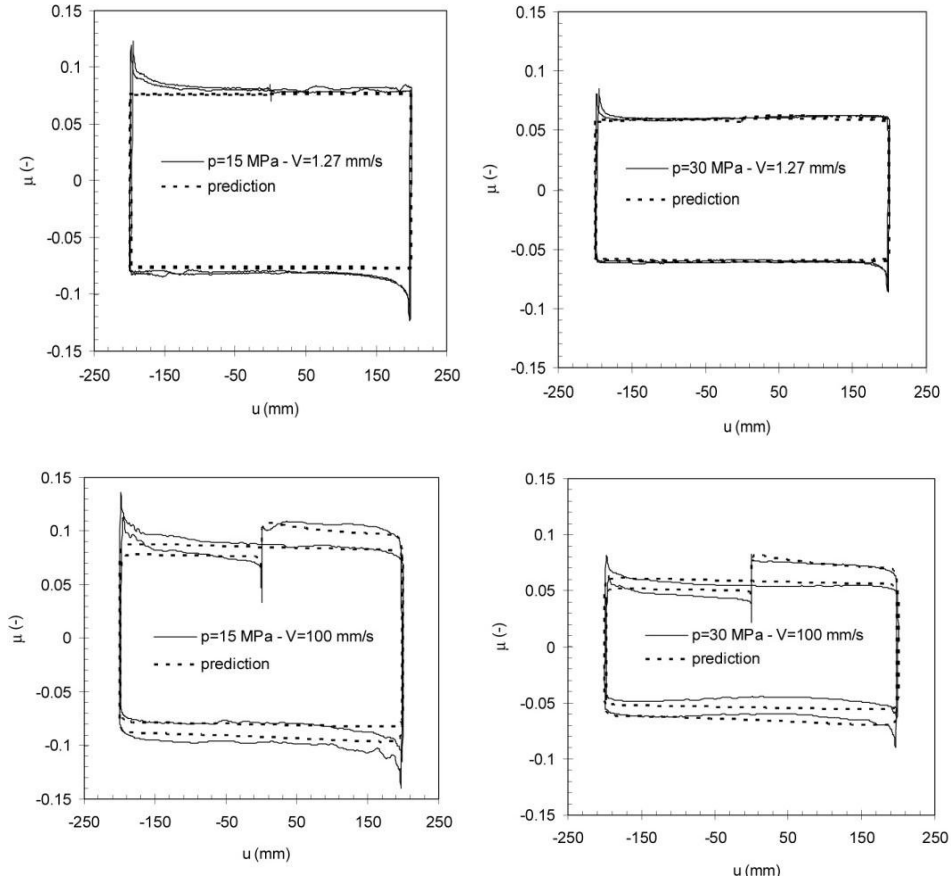

Figure 49: Experimental and predicted (load + cycling + velocity effect) friction coefficient -displacement loop: 1st picture, p=15 MPa v=1.27 mm/s, 2nd picture, p=30 MPa v=1.27 mm/s, 3rd picture, p=15 MPa v=100 mm/s, 4th picture, p=30 MPa v=100 mm/s.

The proposed friction model designed to include the cycling degradation together with the effects of load and velocity is the first model able to describe the experimental behavior of the isolators having a low friction high strength polymer stainless steel sliding surface. The variable included in the degradation law were

based on the equivalent uniformly distributed heat flux investing the sliding surface and assumes the hypothesis of uniform temperature over the whole surface.

The comparison of the experimental data with values predicted by the friction model with and without the degradation law showed the importance of the cyclic degradation in the prediction of the force displacement loop and introduced for the first time the importance of the study of dissipation of dissipative characteristic of friction pendulum due to the thermal effect.

The studies reported in this chapter represent the state of art of the phenomenological behavior of friction pendulum. Even though different studies have been carried out over the last twenty years, there are still important phenomenological characteristics of friction pendulum system that were not considered in the design of this device.

In fact the effect of cumulated motion of the sliding surface, as well as the temperature rise on the contact surface have not been studied, or even considered, in full-scale experimental testing.

Furthermore, the behavior of the PTFE-stainless steel or chromium surfaces even though has been widely studied is not always suitable for application with friction pendulum is not optimal for many reasons. In fact, it has a very low friction coefficient, not suitable to get great energy dissipation, which is subjected by further reduction of the friction coefficient due to the heat generated by the energy dissipation with a consequently great reduction of the bearing capacity due to the heating. In addition to that, composite materials based on PTFE after severe dynamic tests showed some time separation of particles due to the deterioration of the binder for the effect of heat.

The continuous development of new materials as high strength polymers used to improve the degradation rubbing of the sliding surfaces and the frictional characteristics makes it essential to study the mechanical characteristics of these new devices with enhanced characteristics in order to determine their reliability and proper functioning.

The studied report in the next parts of this thesis provides an insight about the effect of the rise of temperature due to the mechanical work done to overcome the friction forces involved during the motion in a single friction pendulum bearing, is given. An experimental approach to evaluate live temperature rise during the motion is studied in chapter 5 and a prediction model for evaluating the friction coefficient of dissipative characteristics of high strength polymer friction pendulum bearing is provided in chapter 7.

Chapter 4

4. Theory of frictional Heating

The sliding motion which occurs in polymer- stainless steel surfaces is coupled with a frictional heating basically due to the mechanical work done for overcome the friction forces involved during the motion.

In this chapter the classic work of Carslaw and Jeager is introduced to understand the basic theory of frictional heating. The theory reported will be used in chapter 6 to make a comparison between the experimental results described in chapter 5 and the analytical model explained here.

4.1. Frictional Heating Nomenclature

In applying the frictional heating concept it is important understand which parameters are involved during the sliding motion, which occurs in friction pendulum bearings. In this first section it is reported a nomenclature list to explain the most important parameters that are involved in this work.

Bulk, Contact, and Flash Temperature (Temperature rise). The bulk temperature is defined as the average temperature of the body prior to frictional heating, the bulk temperature,T_b, remains constant in the body at some distance from the location of frictional energy dissipation. Upon frictional heating, the surface temperature ascends from this bulk temperature to a contact temperature,

T_c, at each point comprising the real area of contact. This temperature increase is commonly referred to as the flash temperature, T_f. Therefore:

(4.1) $$T_f = T_c - T_b$$

Heat Partition Factor**.** When two surfaces engage in sliding over a given contact area, the thermal energy generated per unit time, q, is assumed to be distributed such that part of the heat, namely $q_1 = \gamma_1 q$ penetrates body 1, as the remainder, $q_2 = \gamma_2 q$, enters body 2. The coefficients γ_1 and γ_2 are known as heat partition factors.

As a function of the thermal properties, bulk temperatures, and relative speeds of the respective components, expressions for γ_i have been developed recognizing that:

(4.2) $$\gamma_1 + \gamma_2 = 1$$

and that the contact temperature at each point on the interface is identical for both surfaces. Typically, only the maximum or mean surface temperatures within a given contact area are equated to ease the analysis.

Thermal conductivity. Thermal conduction is the phenomenon by which heat is transported/transferred from high to low temperature regions. The property that characterizes the ability of a material to transfer heat is the thermal conductivity,

(4.3) $$q = -k\left(\frac{\partial T}{\partial n}\right)$$

where q denotes the heat flux, or heat flow, per unit time per unit area, k is the thermal conductivity, and $\partial T/\partial n$ is the temperature. The units for q and k are W/m^2 and W/(m°·C), respectively. (Values for stainless steel and PTFE are given

in Table 3). It should be noted that the above equation is valid for only steady-state heat flow, that is, for situations in which the heat flux does not change with time.

Table 3: Thermal Properties of PTFE and Stainless Steel

	Thermal Conductivity W/(m°C)	Thermal diffusivity (mm^2/s)
Unfilled PTFE	0.24	0.010×10^{-5}
18%Cr,8%Ni Steel	16.3	0.444×10^{-5}
15% Cr, 10% Ni Steel	19	0.526×10^{-5}

The specific heat is the amount of heat per unit mass required to raise the temperature by one degree Celsius. The relationship between heat and temperature change is usually expressed in the form shown below where c is the specific heat. The relationship does not apply if a phase change is encountered, because the heat added or removed during a phase change does not change the temperature, but changes the physical state of the molecules, by increasing their kinetic energy.

$$q = c_p m \Delta T \tag{4.4}$$

the specific heat capacity are J/(kg°C).

Thermal diffusivity (usually denoted α, but κ and D are also used) is the thermal conductivity divided by density and specific heat capacity at constant pressure. It has the SI unit of m²/s:

$$D = \frac{k}{\rho c_p} \tag{4.5}$$

where k is the thermal conductivity (W/(m·K)), ρ is the density (kg/m³) and c_p is the specific heat capacity (J/(kg·K)). Diffusivity values for various metals are in Table 4.

Thermal diffusivity is the measure of thermal inertia. In a substance with high thermal diffusivity, the heat moves rapidly through it because the material conducts heat quickly relative to its volumetric heat capacity.

Table 4: Thermal diffusivity of various metals.

Material	Thermal diffusivity (m^2/s)	Thermal diffusivity (mm^2/s)
Silver, pure (99.9%)	1.6563×10^{-4}	165.63
Gold	1.27×10^{-4}	127
Copper at 25°C	115×10^{-6}	255
Aluminium	8.418×10^{-5}	84.18
Steel, 1% carbon	1.172×10^{-5}	11.72
Steel, stainless 304A	4.2×10^{-6}	4.2
Steel, stainless 310 at 25°C	3.352×10^{-6}	3.352
Iron	2.3×10^{-5}	23

Péclet number, P_e, is a dimensionless number defined as,

$$P_e = \frac{\rho c_p v_c u_c}{k} = \frac{v_c u_c}{D} \tag{4.6}$$

Where ρ is the density, c_p is the specific heat at constant pressure, v_c is the velocity, u_c is a characteristic length and k is the thermal conductivity. It represents the thermal energy transported by the movement or convection of the medium, to the thermal energy conducted away from the region where the frictional energy is being dissipated.

4.2. Theory of frictional Heating

To evaluate the temperature rise at the sliding interface the Carslaw and Jaeger Theory (1959) has been typically used. These authors analyzed the problem of a semi-infinite solid subjected by a constant heat flux q (Figure 50).

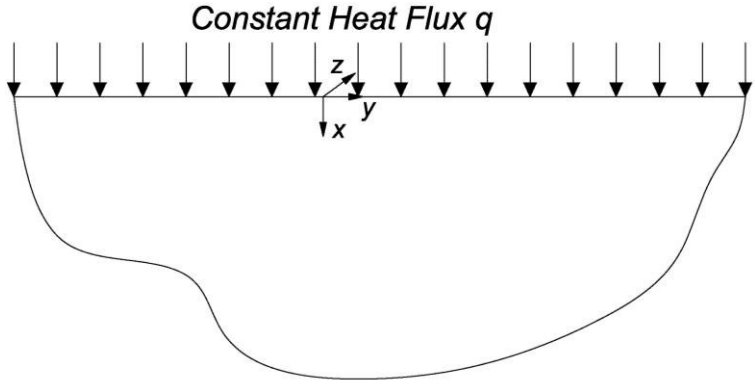

Figure 50: Semi-infinite Solid with constant heat flux at the surface x=0.

The sliding contact may be considered as two solid bodies, of which one or even both move at uniform speed past heat source, which represents the sliding contact surface. This source has a heat flux distribution, q, with an average value of q_{av}. A schematic illustration of the problem is given in figure 51.

The maximum contact temperature, T, will occur at the surface of either body and it could be evaluated with equation (4.1). The temperature rise respect the bulk temperature, will occur at the surface of both bodies and it is evaluated as,

$$T_s = F\frac{\gamma q_{av}}{b}\sqrt{t} \tag{4.7}$$

Where t represents the time during which any points on the surface is exposed to heat, $b = \sqrt{c_p \rho k}$ is a thermal contact coefficient. F is dependent on the form of the heat flux distribution, q. For a square heat source with uniform distribution $q = q_{av}$, $F = 2/\pi^{1/2}$, which is a close approximation for a semielliptical distribution while γq represents the portion of heat entering to the body for which the heat partition factor is referred. With different notation, and considering reasonable that the portion $q_1 = 0$ and $q_2 = q$ the equation (4.7) could be written as:

$$T_s = \frac{2q}{k}\left(\frac{Dt}{\pi}\right)^{1/2} \tag{4.8}$$

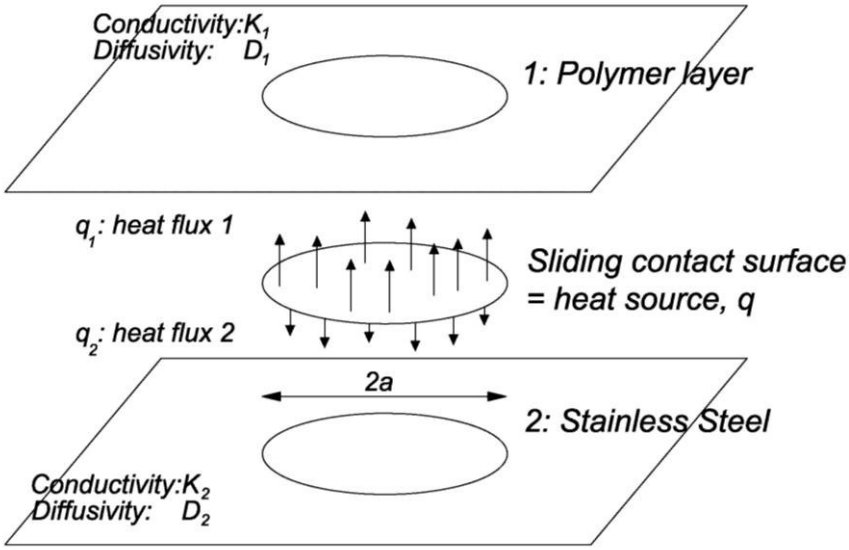

Figure 51: Schematic illustration of the sliding contact surface problem.

In applying equations (4.7) and (4.8) it must be pointed out that the solution is valid for a half-space with heat flux over the entire free surface (see figure 50), whereas the study case has a finite plan dimensions and depth. The approximation $q = constant$ is not, in general, true because the heat flux generated by friction is dependent on the variation of time and space, of the friction forces, and of the normal load distribution. Furthermore they're not considered the effects of radiation and convection because the problem is limited for short time intervals. For longer time these factors could play an important role, and eventually a steady condition may be reached.

Considering the case, in which a constant velocity motion is applied on the body 1 or 2 with a maximum displacement $u_c < a$ for a total time exposure t,

$$t = \frac{4u_c}{v_c} N \tag{4.9}$$

Where N represents the number of cycles. Let's consider an average heat flux evaluated as the total energy dissipated in N cycles divided by the area A and time t,

$$q_{av} = \frac{4NF_f u_c}{tA} = \frac{F_f v_c}{A} = \mu p v_c \tag{4.10}$$

where F_f represents the friction force, μ the coefficient of sliding friction, and p the apparent pressure. Appling eq. (4.9) (4.10) in (4.8) we obtain the flash temperature for a constant velocity motion.

$$T_s = 2.26N^{1/2} \frac{\mu p u_c v_c}{k} \left(\frac{D}{u_c v_c} \right)^{1/2} \tag{4.11}$$

The quantity under root square $u_c v_c/D$ is the Péclet number. If we consider a sinusoidal input, as shown in figure 53, combining eq.(4.8) with

$$t = \frac{2\pi N}{\omega}, \tag{4.12}$$

and

$$q_{av} = \frac{2\mu p u_s \omega}{\pi} \tag{4.13}$$

The flash temperature for a sinusoidal motion it is obtained,

$$T_s = 1.8 N^{1/2} \frac{\mu p u_s^2 \omega}{k} \left(\frac{D}{u_s^2 \omega} \right)^{1/2} \tag{4.14}$$

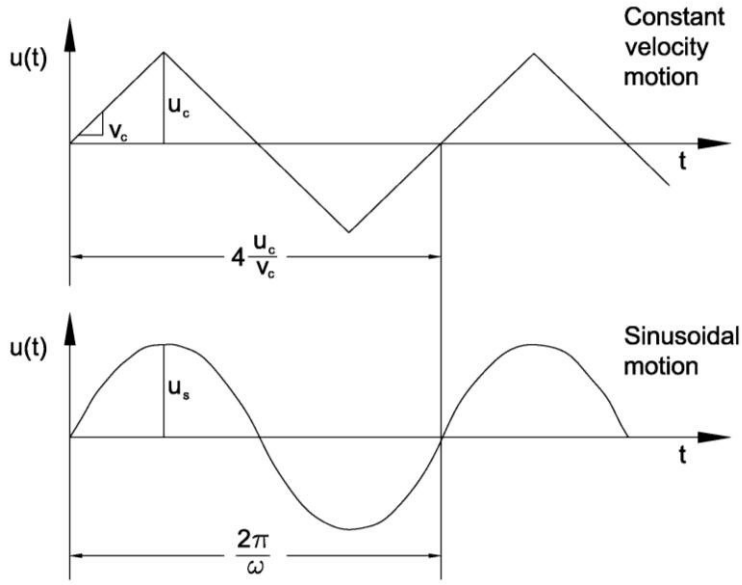

Figure 52: Motions considered in the sliding contact problem.

When the amplitude of motion is larger than the radius a of the apparent contact area . $u_c > a$ (see figure 53), equation (4.11) became,

$$T_s = \frac{2qD^{1/2}}{\pi^{1/2}k}\left\{t^{1/2} - (t-\bar{t})^{1/2}\right\} \tag{4.15}$$

Where $\bar{t}$ represents the duration of contact between body 1 and body 2.

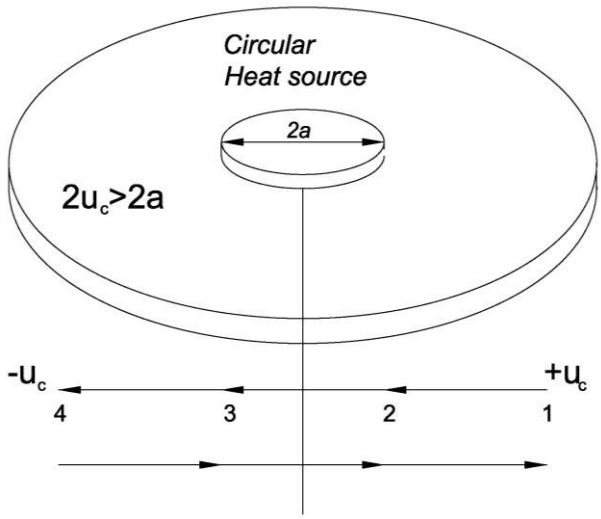

Figure 53: Sliding contact problem for large displacement $\boldsymbol{u_c > a}$.

In eq. (4.15) $\bar{t}$ is less that $2a/v_c$, because the apparent contact area is circular and not square. In particular considering a circular heat source described by the well known equation $y^2 + z^2 = a^2$ the time for cross along the y axis with a constant velocity called exposure time is given by eq. (4.16) and the average distance traveled during this time is $\pi a/2$.

$$\bar{t} = \frac{1}{a}\int_{-a}^{a}\frac{\left(a^2 - z^2\right)^{1/2}dz}{v_c} = \frac{\pi a}{2v_c} \tag{4.16}$$

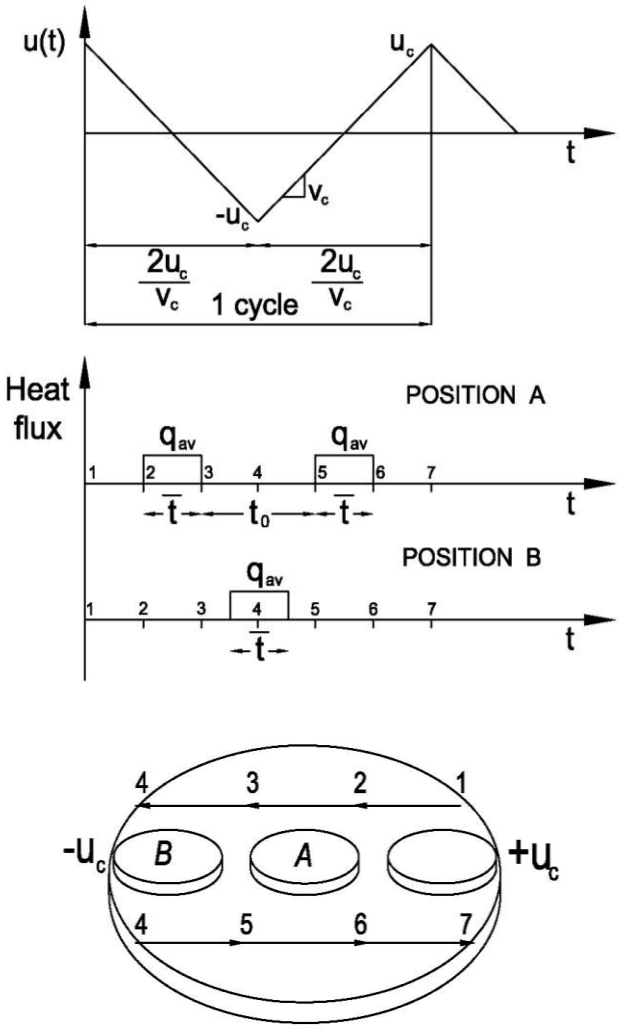

Figure 54: History of heat flux in a large motion with a constant velocity v_c for the position A and B.

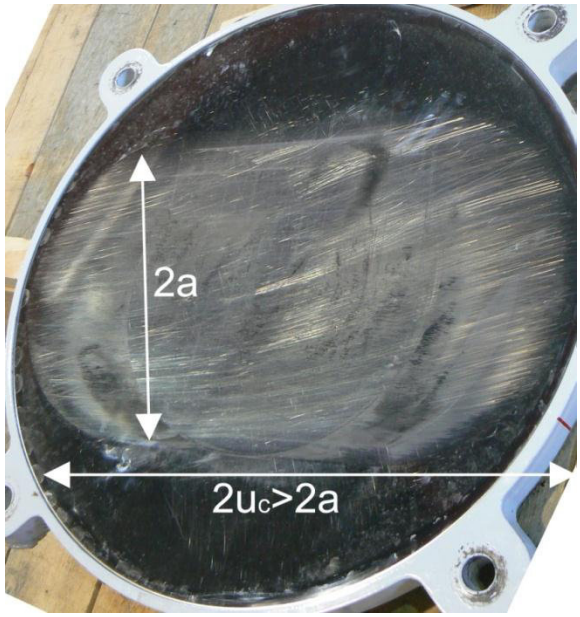

Figure 55: The stainless steel surface after a test in a friction pendulum bearing. Stainless steel sliding surface shows a superficial orientation in the part subjected by the motion $\boldsymbol{2u_c}$. In some spots there are polymer portions which come from the polymer layer.

Equations (4.11), (4.14) and (4.15) are similar in form to equations used by tribologists to estimate the flash temperature. This last case represents the typical situation in sliding seismic isolator bearings.

These equations may be written for the temperature rise at depth $x > 0$. Moreover, a general solution for the problem of the semi-infinite body with heat flux $q(t)$ at $x = 0$ may be deduced from the solution of the problem of constant heat flux and use of Duhamel's theorem (Carslaw and Jaeger, 1959).

$$T_f(x,t) = \frac{D^{1/2}}{\pi^{1/2} k} \int_0^t q(t-\tau) \exp\left(-\frac{x^2}{4Dt}\right) \frac{d\tau}{\tau^{1/2}} \tag{4.17}$$

Where T_f is the temperature distribution, x is the depth below the contact surface and t is the time of analysis.

Eq. (4.17) will be used for the evaluation of an analytic flash temperature in chapter 6. The results will be used for a comparison between the experimental and analytical data.

Chapter 5

5. Experimental Investigation

The sliding motion of FPB involves mechanical work to overcome the friction forces which are transformed into thermal energy. The heat source created in the contact surface produces a temperature rise which could affect the dynamic response of these devices. The assessment of the current temperature rise of the sliding bearing during the motion represents an important step for developing a confident phenomenological theory capable of evaluating the degradation of dissipative characteristics of the contact surface due to thermal effects.

In this section the sliding contact problem of a friction pendulum has been investigated. In this device the contact surface is given by the concave stainless steel surface and a high strength polymers liner. In particular, the heating developed on the whole sliding surface during laboratory tests has been investigated with a thermographic camera, and the data collected have been analyzed according to the temperatures measured with thermocouples. The spatial distribution of the temperature variation is described and the temperatures recorded during sinusoidal tests with different applied normal loads and peak velocities are extrapolated and represented for 3 particular points of the concave surface.

The presented procedure is useful for investigating the frictional heating involved during motion on the whole sliding surface by means of a non-invasive instrument such as an infrared thermographic camera.

5.1. Experimental Campaign and Test Facility

A set of sliding bearings, with concave surfaces, was tested under three values of vertical load for a three-cycle sinusoidal input with fixed displacement range and three different peak velocities. The effective radius of the concave surface of these specific bearings is 4000 mm, and the low friction material that interfaces the stainless steel concave surface is a high strength polymer composite having a compressive strength of 220 MPa, more than twice that of PTFE.

Therefore the peculiar characteristic of these bearings consist of reducing the dimension of the device.

The devices were tested at the Caltrans SRMD Testing Facility at the University of California San Diego campus equipped with a 6 DOFs shake table specifically designed for full scale testing of isolators and energy dissipators (Benzoni and Seible, 1998).

The system has been designed to perform four primary situations which could occur for the majority of SMRD test specimens.

- Simulate the relative seismic motion at the interface of a full-scale SRMD bearing specimen by applying large horizontal shearing displacements in real-time.
- Concurrently apply any associated vertical displacement.

- React against the associated horizontal shearing forces.
- Simulate the bridge's dead weight by applying large, static, vertical compressive loads

A schematic perspective view of SRMD Test System is given in Figure 56.

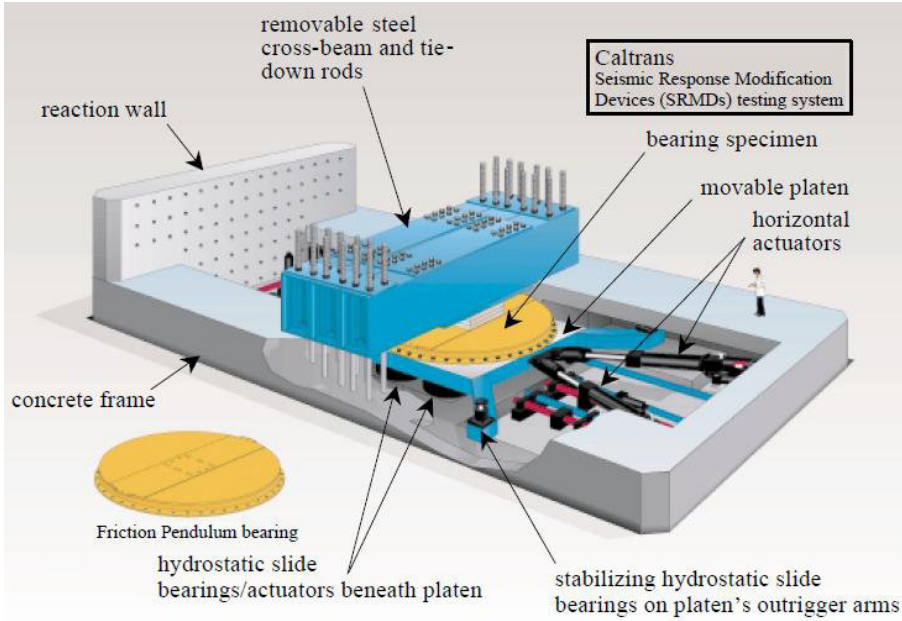

Figure 56: Perspective view of SRMD Test System.

The system includes a pre-stressed concrete box , a removable steel cross beam and an interchangeable steel-concrete platens. SRMD bearing specimens are installed between a movable (3550 mm x 4880 mm) steel-concrete composite platen and the steel cross-beam. The devices move from one side providing the relative shearing displacements being installed to the steel plate on the bottom portion. The upper part of the device is fixed with the steel cross beam and

remains fixed during testing. The vertical and horizontal displacements are accomplished by 12 hydraulic actuators.

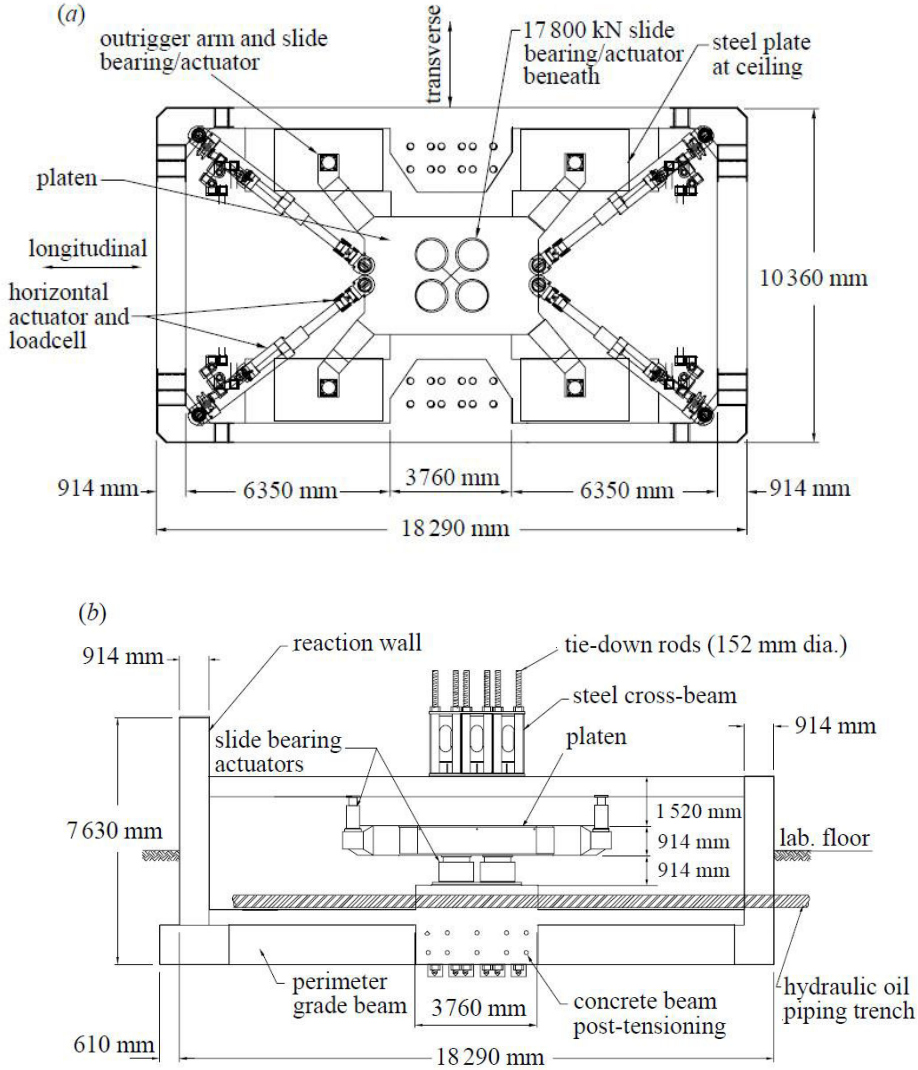

Figure 57: Plan and cross-section views of SRMD Test System.

The large lateral displacements required of the platen are accomplished via four horizontal actuators, extending from the corners of the concrete frame to the platen.

These non-orthogonal actuators can each swivel up to 10° in the horizontal and up to 2° in the vertical plane. They each have a stroke of• ±1220 mm, a piston diameter of 510 mm, and a compression force capacity of 7100 kN.

Figure 58: Four horizontal actuators can accommodate large lateral displacements.

These four actuators can accommodate a very large range of combined longitudinal, transverse and rotational (yaw) motions. The horizontal forces from these actuators are resisted by the post-tensioned walls of the concrete frame. The concrete frame transfers the net horizontal force to the steel cross-beam, which in turn reacts against the top of the bearing specimen. Hence, the system forms a completely self-reacting horizontal frame, as seen in figure 3. Inertial loads associated with dynamic testing are transmitted into the surrounding foundation.

Simultaneously, large vertical compressive loads must be applied to the bearing specimen. The traditional multi-axis shaking-table configuration including

vertical actuators with swivels at each end would have required extremely long-stroke actuators and a very deep foundation. Instead, the system's platen slides over a group of four stationary hydrostatic sliding bearings/actuators, fixed to the concrete frame beneath the platen. Each actuator is 810 mm in diameter and is capable of applying up to 17.8 MN of compression at a hydraulic oil pressure of 34 MPa. Each bearing also has a stroke of• ±120 mm to accommodate the vertical, roll and pitch degrees of freedom. The polished underside of the steel platen slides over these four hydrostatic actuators with very little frictional resistance.

Figure 59: Four stationary hydrostatic sliding bearings/actuators, fixed to the concrete frame beneath the platen.

Above the platen, the vertical force is transmitted through the bearing specimen and into the removable steel cross-beam. This steel cross-beam is, in turn, anchored to the concrete frame with 24 post-tensioned 152 mm diameter steel tie rods extending to the bottom of the concrete frame. Hence, the system forms a second self-reacting frame in the vertical plane, as illustrated in Figure 60.

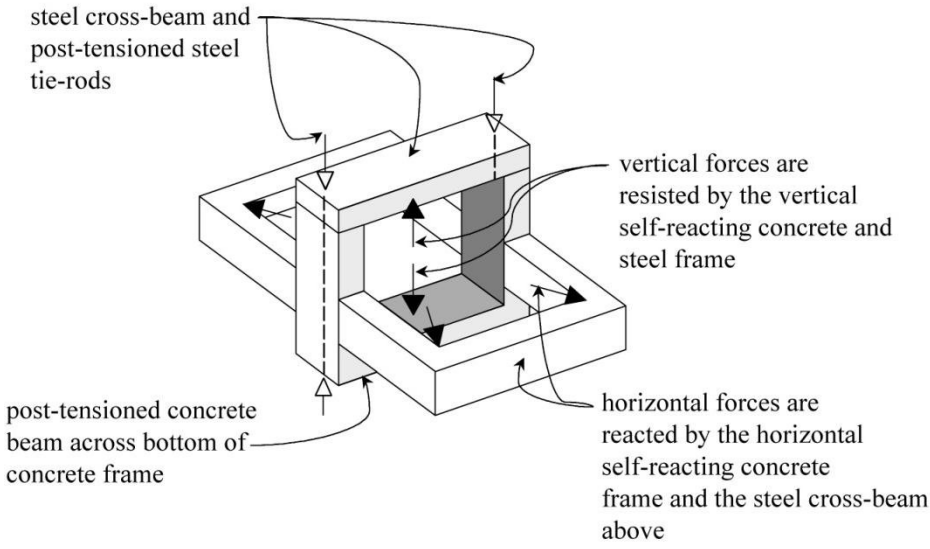

Figure 60: Schematic of horizontal and vertical self-reacting frames.

The system is completed by a heavily reinforced and two-way post-tensioned reaction wall at the end of the concrete frame. This provides the necessary reaction structure for testing SRMD dampers and lock-up devices.

The need to apply substantial vertical compressive loads while undergoing large lateral displacements presents new challenges for a seismic system. SRMD bearing specimens will often either increase or decrease in height as they undergo lateral displacement. Since the vertical compression load must be maintained throughout a test, the vertical degree of freedom must be controlled for both displacement and load, concurrently. This is accomplished by a hybrid control loop in the vertical degree of freedom, with adjustable priorities on each parameter. The remaining five degrees of freedom are typically controlled solely by displacement.

5.2. Description of Thermographic camera

A thermal imaging camera is a reliable non contact instrument which is able to scan and visualize the temperature distribution of entire surfaces of machinery and electrical equipment quickly and accurately. A thermographic camera has been used during the test for evaluating the temperature rise in the stainless steel concave surface. The thermographic camera is able to detect the infrared energy of the object observed and evaluate the intensity by means of an infrared detector. For the test campaign a high performance Infrared imaging and measurement system was used that is suitable for advanced thermal analysis. The technology of the thermographic camera allows an outstanding image stability and uniformity, and it is ideal where precision temperature measurements from -20°C to 2000°C and high sensitivity are required.

Figure 61: The thermographic camera used in the experimental tests.

The technical specifications of the thermographic camera are collected in Table 5.

Table 5: Technical specifications of the thermographic camera used in the experimental campaign.

IMAGE PERFORMANCE	
Field of view/min focus distance	20° x 15° / 0.3m
Image frequency	50/60 Hz
DETECTOR	
Type	GaAs, QWIP 320x240 pixels
Spectral range	8 to 9 µm
MEASUREMENT	
Temperature range	-20°C to +1500°C (-4°F to 2732°F)
Accurancy	±1% or ±1°C (for measurement ranges up to +150°C)
	±2% or ±2°C (for measurement ranges above +150°C)
Automatic emissivity correction	Variable from 0.1 to 1.

Some theoretical concepts of IR Thermographic camera technology are provided in the following sub section.

5.2.1. IR Thermography

Although infrared radiation (IR) is not detectable by the human eye, an IR camera can convert it to a visual image that depicts thermal variations across an object or scene. IR covers a portion of the electromagnetic spectrum from approximately 900 to 14,000 nanometers (0.9–14 μm). IR is emitted by all objects at temperatures above absolute zero, and the amount of radiation increases with temperature. Thermography is a type of imaging that is accomplished with an IR camera calibrated to display temperature values across an object or scene. Therefore, thermography allows one to make on-contact measurements of an objects temperature.

IR camera construction is similar to that of a digital video camera. The main components are a lens that focuses IR onto a detector, plus electronics and software for processing and displaying the signals and images. Typically, IR cameras are designed and calibrated for a specific range of the IR spectrum. This means that the optics and detector materials must be selected for the desired range.

The intensity of the emitted energy from an object varies with temperature and radiation wavelength. If the object is colder than about 500°C, emitted radiation lies completely within IR wavelengths. In addition to emitting radiation, an object reacts to incident radiation from its surroundings by absorbing and reflecting a portion of it, or allowing some of it to pass through (as through a lens). From this physical principle, the Total Radiation Law is derived, which can be stated with the following formula:

$$W = \alpha W + \rho W + \tau W \tag{5.1}$$

which can be simplified to:

$$1 = \alpha + \rho + \tau \tag{5.2}$$

The coefficients α, β, and τ describe the object's incident energy absorption (α), reflection (ρ), and transmission (τ). Each coefficient can have a value from zero to one, depending on how well an object absorbs, reflects, or transmits incident radiation. For example, if $\rho = 0$, $\tau = 0$, and $\alpha = 1$, then there is no reflected or transmitted radiation, and 100% of incident radiation is absorbed. This is called a perfect blackbody. In the real world there are no objects that are perfect absorbers, reflectors, or transmitters, although some may come very close to one of these properties.

Nonetheless, the concept of a perfect blackbody is very important to the science of thermography, because it is the foundation for relating IR radiation to an object's temperature. Fundamentally, a perfect blackbody is a perfect absorber and emitter of radiant energy. This concept is stated mathematically as Kirchhoff's Law. The irradiative properties of a body are denoted by the symbol ε, the emittance or emissivity of the body.

Kirchhoff's law states that $\alpha = \varepsilon$, and since both values vary with the radiation wavelength, the formula can take the form $\alpha(\lambda) = \varepsilon(\lambda)$, where λ denotes the wavelength. The total radiation law can thus take the mathematical form $1 = + \rho + \tau$, which for an opaque body ($\tau = 0$) can be simplified to $1 = \varepsilon + \rho$ or $\rho = 1 - \varepsilon$ (i.e., reflection = 1 – emissivity). Since a perfect blackbody is a perfect absorber, $\rho = 0$ and $\varepsilon = 1$.

From Planck's law, the total radiated energy from a blackbody can be calculated. This is expressed by a formula known as the Stefan-Boltzmann law,

$$W = \sigma T^4 \quad \left(W / m^2\right), \tag{5.3}$$

where σ is the Stefan-Boltzmann's constant (5.67×10^{-8} W/m^2K^4). The radiative properties of objects are usually described in relation to a perfect blackbody (the perfect emitter). If the emitted energy from a blackbody is denoted as W_{bb}, and that of a normal object at the same temperature as W_{obj}, then the ratio between these two values describes the emissivity (ε) of the object,

$$\varepsilon = \frac{W_{obj}}{W_{bb}} \tag{5.4}$$

Thus, emissivity is a number between 0 and 1. The better the irradiative properties of the object, the higher its emissivity. An object that has the same emissivity ε for all wavelengths is called a greybody. Consequently, for a greybody, Stefan- Bolzmann's law takes the form

$$W = \sigma T^4 \quad \left(W / m^2\right) \tag{5.5}$$

which states that the total emissive power of a greybody is the same as that of a blackbody of the same temperature reduced in proportion to the value of ε for the object.

Still, most bodies are neither blackbodies nor greybodies. The emissivity varies with wavelength. As thermography operates only inside limited spectral ranges, in practice it is often possible to treat objects as greybodies. In any case, an object having emittance that

varies strongly with wavelength is called a selective radiator. For example, glass is a very selective radiator, behaving almost like a blackbody for certain wavelengths, whereas it is rather the opposite for other wavelengths.

The radiation that impinges on the IR camera lens comes from three different sources. The camera receives radiation from the target object, plus radiation from its surroundings that has been reflected onto the object's surface. Both of these radiation components become attenuated when they pass through the atmosphere. Since the atmosphere absorbs part of the radiation, it will also radiate some itself (Kirchhoff's law).

Given this situation, we can derive a formula for the calculation of the object's temperature from a calibrated camera's output. The emission from the object is equal to $\varepsilon \cdot \tau \cdot W_{obj}$, where ε is the emissivity of the object and τ is the transmittance of the atmosphere. The reflected emission from ambient sources is $(1 - \varepsilon) \cdot \tau \cdot W_{amb}$, where (1 – ε) is the reflectance of the object. While the emission from the atmosphere $(1 - \tau) \cdot W_{atm}$, where $(1 - \tau)$ is the emissivity of the atmosphere.

The total radiation power received by the camera can now be written:

$$W_{tot} = (1-\tau)\cdot W_{obj} + (1-\varepsilon)\cdot \tau \cdot W_{amb} + (1-\tau)\cdot W_{atm} \quad (5.6)$$

where ε is the object emissivity, τ is the transmission through the atmosphere, T_{amb} is the (effective) temperature of the object's surroundings, or the reflected ambient (background) temperature, and T_{atm} is the temperature of the atmosphere.

Therefore to arrive at the correct target object temperature, it is necessary to evaluate the emissivity of the object and evaluate the contributions given by ambient sources and the emission from the atmosphere. The only emission from the object could be obtained simply by subtracting the total radiation power received by the camera from the effect of ambient sources and the reflectance of the object.

$$W_{obj} = aW_{tot} - bW_{amb} - cW_{atm} \quad (5.7)$$

5.3. Description of Specimen

A set of 3 sliding bearings, with concave surfaces, has been tested under three values of vertical load and 4 different peak velocities.

The tests are divided into two categories in fact the two different types of excitations were used, triangular (sow tooth curve) or sinusoidal wave respectively.

The tests characterized by the triangular shape have been executed in order to evaluate the breakaway friction coefficient and the possibility of slip-stick phenomena.

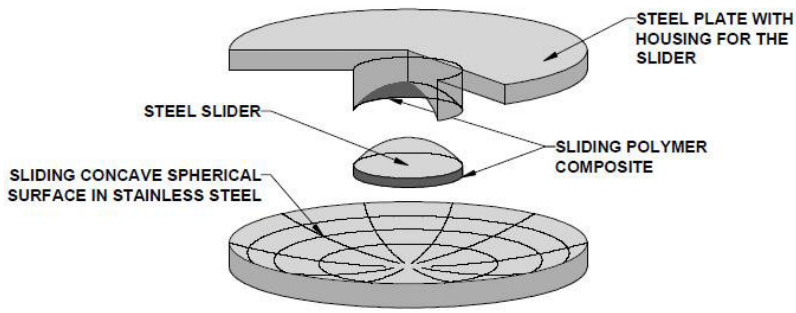

Figure 62: Schematic illustration of the Friction Pendulum Bearing tested.

A schematic view of the devices tested in this campaign is shown in Figure 62 while in Table 6 is reported the protocol test.

As shown in Figure 63 three full cycles are applied for all the tests, with a displacement amplitude of 260 mm. The sinusoidal tests have been executed with the main purpose of evaluating the dynamic friction coefficient and its dependency to variables such as the sliding velocity, the applied normal load and its decay with

the performed motion. Since the velocity characterizing the starting and final point of a sinusoidal displacement is the peak velocity, it has been necessary to apply a displacement history in order to start and end the sinusoidal loop with the required applied velocity. In this way it was possible to avoid problems of instability due to the application of impulsive forces to the device. Therefore for sinusoidal tests the bearing starts moving with a very low velocity and reaches a displacement of approximately 150 mm. Then the motion is inverted and the bearing is accelerated up to the peak velocity of the sinusoidal motion, that is reached when the relative displacement is zero.

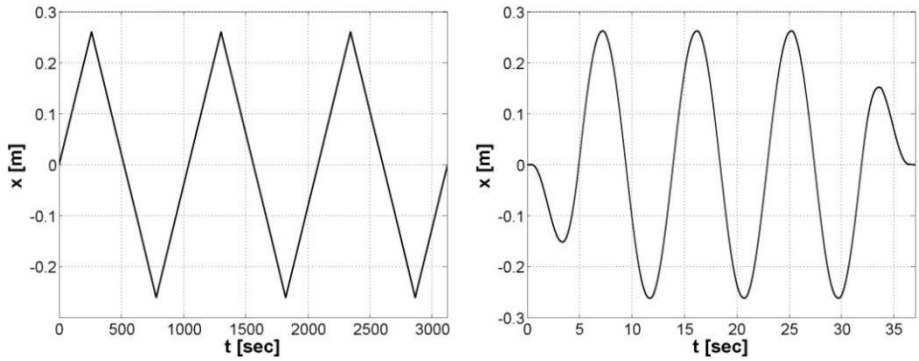

Figure 63: Triangular and sinusoidal input used in the tests.

The test have been carried out with low, medium and high vertical loads, applying verticals loads W of 500, 1000 and 2850 kN which correspond respectively to pressure p of 8, 16 and 45MPa. For each pressure, tests with a sinusoidal input have been carried out with a peak velocity of 182 mm/s, 260mm/s and 338mm/s. For triangular tests only a low velocity of 1 mm/s was used (see table below).

Table 6: Protocol test

Test	Frequency	Velocity	Disp	Vertical Load	Cycles	Input
		[m/s]	[m]	[kN]	[]	
201	0,00096	0,001	0,26	2820	3	triangular
202	0,00096	0,001	0,26	1000	3	triangular
203	0,00096	0,001	0,26	500	3	triangular
204	0,15915	0,26	0,26	2820	3	sinusoidal
205	0,11141	0,182	0,26	2820	3	sinusoidal
206	0,2069	0,338	0,26	2820	3	sinusoidal
207	0,15915	0,26	0,26	1000	3	sinusoidal
208	0,11141	0,182	0,26	1000	3	sinusoidal
209	0,2069	0,338	0,26	1000	3	sinusoidal
210	0,15915	0,26	0,26	500	3	sinusoidal
211	0,11141	0,182	0,26	500	3	sinusoidal
212	0,2069	0,338	0,26	500	3	sinusoidal
301	0,00096	0,001	0,26	2820	3	triangular
302	0,00096	0,001	0,26	1000	3	triangular
303	0,00096	0,001	0,26	500	3	triangular
304	0,15915	0,26	0,26	2820	3	sinusoidal
305	0,11141	0,182	0,26	2820	3	sinusoidal
306	0,2069	0,338	0,26	2820	3	sinusoidal
307	0,15915	0,26	0,26	1000	3	sinusoidal
308	0,11141	0,182	0,26	1000	3	sinusoidal
309	0,2069	0,338	0,26	1000	3	sinusoidal
310	0,15915	0,26	0,26	500	3	sinusoidal
311	0,11141	0,182	0,26	500	3	sinusoidal
312	0,2069	0,338	0,26	500	3	sinusoidal
401	0,00096	0,001	0,26	2820	3	triangular
402	0,00096	0,001	0,26	1000	3	triangular
403	0,00096	0,001	0,26	500	3	triangular
404	0,15915	0,26	0,26	2820	3	sinusoidal
405	0,11141	0,182	0,26	2820	3	sinusoidal
406	0,2069	0,338	0,26	2820	3	sinusoidal
407	0,15915	0,26	0,26	1000	3	sinusoidal
408	0,11141	0,182	0,26	1000	3	sinusoidal
409	0,2069	0,338	0,26	1000	3	sinusoidal
410	0,15915	0,26	0,26	500	3	sinusoidal
411	0,11141	0,182	0,26	500	3	sinusoidal
412	0,2069	0,338	0,26	500	3	sinusoidal

5.4. Thermal experiments

Various instruments were used during the tests to monitor the variation of temperature in the energy dissipating elements of the friction pendulum. The most common method consisted of measuring the temperature with thermocouples which are embedded at the center of a stainless steel plate at depth of 1.5-2 mm from the contact area.

In this case the temperature rise which occurs during the tests was investigated with a thermographic camera and the data collected analyzed according to the temperatures measured with thermocouples.

For each test, the measurement of the temperature was carried out before the run and at 50 sec. and 5 minutes after the run in order to evaluate the thermal configuration of the stainless steel concave surface in the stationary condition before each run and the unsteady state after each run. In particular the thermocouple was applied on 3 different points, called since now, slider ‘s’, middle ‘m’, and border ‘b’, indicating the correspondent position reported in Figure 64.

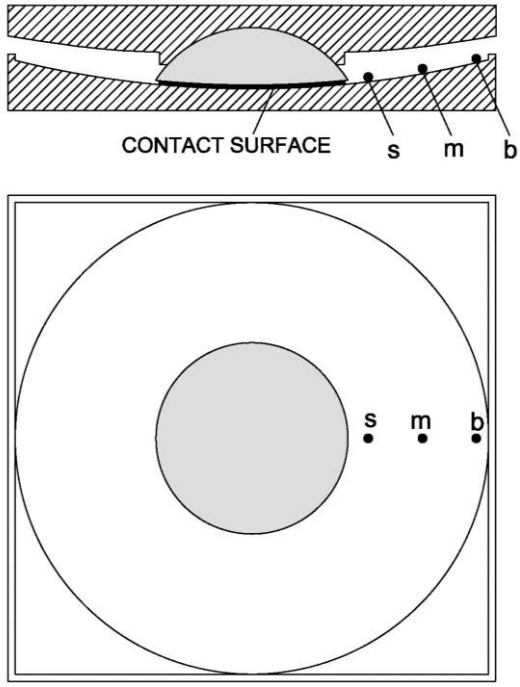

Figure 64: Selected spots for temperature measurement with thermocouple.

At the same time, an acquisition with thermographic camera was carried out starting a couple of seconds before the start of the test up to the end of the input displacement. A additional registration was recorded right after the run, in order to evaluate the IR radiations in the stationary configuration of null displacement and room temperature . The sampling frequency of thermal data is 59.9Hz for sinusoidal test, and it is 1Hz for triangular tests and even for the data acquisition conducted right after the end of each test.

Table 7: Recorded temperature measured with thermocouple in the spots ‘s’, ‘m’ and ‘b’.

		Pre Test			50 sec.			300 sec.		
Test	Room Temp.	Slider	Mid	Border	Slider	Mid	Border	Slider	Mid	Border
[n°]	[°C]	[°C]	[°C]	[°C]	[°C]	[°C]	[°C]	[°C]	[°C]	[°C]
201	21,7	21,2	21,2	21,2	30,0	26,8	24,0	24,3	24,0	23,2
202	22,8	22,5	22,5	22,6	27,6	24,5	24,0	22,5	22,4	22,3
203	21,7	22,5	22,5	22,4	27,6	24,5	24,0	23,8	23,2	22,8
204	22,5	22,3	22,3	22,3	43,0	37,8	27,3	28,5	29,0	24,2
205	23,7	23,0	22,9	22,9	45,8	46,5	32,0	31,5	33,4	26,1
206	23,2	22,2	22,2	22,2	46,7	46,3	30,1	31,3	30,5	28,0
207	23,4	23,1	22,7	22,7	43,0	43,2	28,0	32,4	32,0	26,2
208	23,4	23,2	23,0	23,1	50,0	48,0	30,0	34,0	32,5	28,0
209	23,6	22,1	21,9	21,8	52,0	47,0	26,2	34,0	34,5	26,0
210	20,3	21,2	21,1	21,0	46,0	40,8	26,0	28,6	30,5	23,2
211	21,4	21,6	21,6	21,6	48,0	43,0	26,0	28,5	30,5	23,4
212	21,6	22,5	22,5	22,5	44,8	42,8	28,0	32,0	28,3	23,5
[n°]	[°C]	[°C]	[°C]	[°C]	[°C]	[°C]	[°C]	[°C]	[°C]	[°C]
301	21,6	21,6	21,6	21,6	23,3	23,3	23,1	22,9	22,9	22,9
304	22,2	22,9	22,9	22,9	51,3	53,0	35,0	31,2	35,5	27,0
305	22,8	22,9	22,8	22,8	53,0	52,8	32,5	34,0	35,4	30,0
306	22,5	22,9	22,7	22,7	48,2	51,2	38,0	31,7	32,9	29,7
307	23,5	22,7	22,6	22,7	47,0	46,0	39,8	27,9	32,0	27,9
308	22,7	23,3	23,3	23,3	43,3	44,0	33,3	31,0	31,8	29,0
309	22,3	22,3	22,3	22,3	49,5	47,0	38,5	28,0	33,9	28,1
310	23,0	23,5	23,3	23,3	36,2	40,0	28,2	25,9	27,9	25,9
311	23,7	23,3	23,3	23,3	40,8	40,1	33,0	28,3	30,3	27,3
312	22,9	23,8	23,8	23,2	40,3	46,3	35,3	31,5	31	29,1
[n°]	[°C]	[°C]	[°C]	[°C]	[°C]	[°C]	[°C]	[°C]	[°C]	[°C]
401	24	24,1	24,1	24,1	26,1	26,1	26,1	\	\	\
404	25,2	24,1	24,1	24,1	42,5	43,2	30,5	28,0	28,8	26,6
405	23,2	24,1	24,1	24,1	41,8	41,0	29,8	28,2	30,2	24,2
406	24,5	24,4	24,4	24,2	42,5	39,5	31,5	30,4	30,4	27,3
407	22,7	22,0	22,0	22,0	35,5	34,5	29,5	27,8	29,0	25,2
408	22,8	23,1	22,8	22,9	40,6	36,8	26,0	30,2	29,0	25,5
409	22,5	23,5	23,4	23,4	29,8	30,1	25,5	26,5	26,5	25,4
410	22,7	24,3	24,1	24,1	43,0	36,7	28,7	30,5	30,2	26,0
411	23,9	23,5	23,3	23,5	36,4	34,5	26,5	28,8	28,7	25,1
412	23,7	23,6	23,6	23,6	38,0	34,0	26,5	29,9	28,0	25,8

Approximately 50 seconds and 5 minutes after the end of the tests the increase in temperature due to the frictional behavior of the device was directly measured with thermocouples.

Considering that the imposed maximum displacement is equal for each test, the final temperature variation only depends on the applied normal load, the sliding velocity and the friction coefficient involved during the performing of motion.

The variation of temperatures can be expresses as the product between the applied normal load and the peak velocity of motion. Figure 65 illustrates the variation of temperatures with the product of normal load and peak velocity of the referred test for point "s".

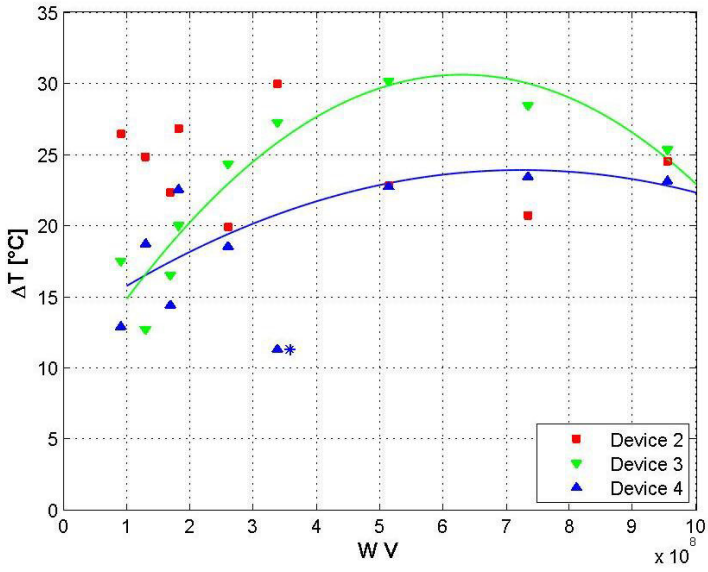

Figure 65: Temperatures recorded on point "s" at approximately 50 sec after the end of tests. The value with * marker has not been considered in the interpolation curve.

The heat flux involving the concave surface is given by the product of the friction coefficient μ, the applied normal load W and the sliding velocity V. The data reported in the previous figure are in good agreement with the referred theory, since on the left side of the graph the values of temperature variation generally increase as the product WV increases. For higher values of the product WV, the temperature variation shows a stabilization or a decrease. The above phenomenon can be explained by considering that the friction coefficient decreases with the energy thermally dissipated during each test. Therefore the heat flux imposed to the sliding surface does not increase linearly with the product WV because of the simultaneous decay of the friction coefficient.

The graph previously reported indicates a considerable degradation of the "flash temperatures" with time. The deviancy can be explained considering that the dissipation of the accumulated thermal energy is associated with both the heat conduction through the concave stainless steel surface and the convection heat transfer, which could be affected by external factors that could influence the analyzed parameters.

5.5. Elaboration of Thermal Data and Calibration of Thermographic camera

The output file elaborated by the thermographic camera is a binary file containing matrices of 320x240 pixels. These matrices contain the recorded value of the infrared radiation (IR). The number of matrices reported in the output depends on the frequency of data acquisition and on the time of acquisition. These

parameters are set according to peak velocity of the referred test. The selected frequency of acquisition of thermal data is 59,9Hz for sinusoidal tests and 1Hz for triangular tests.

Accordingly to the image resolution, the thermographic camera is able to measure the temperature at one single spot. The bigger the image resolution, the smaller the dimension of the spot analyzed and the relative temperature detected. The thermographic camera used in this test has a 320 x 240 pixels of resolution (see Figure 66).

Figure 66: Thermo-camera SC 3000 used during pre-test on a scaled double pendulum bearing.

For the arrangement of the thermographic camera a 3D modeling study has been performed before the tests. The inclination and the field of view of the device has been set to point the camera to the concave sliding surface and catch the temperature rise during the motion of the test. According with the test protocol (??) it was convenient to install the thermographic camera as illustrated in Figure 68. The thermographic camera is fixed to (?) a rigid stainless steel frame which was then bolted to the cross beam plate. This system is arranged in parallel to the motion imposed to the device. In this way it was possible to point the camera against the whole concave surface except the portion of the slider covered by the slider of the device (see Figure 67).

Figure 67: The left picture illustrates a field of view of the thermographic camera with the arrangement showed in the right picture.

Figure 68: Final setup of the camera supported by a frame bolted to the bottom plate of the steel cross beam.

The output file elaborated by the thermographic camera is a binary file containing matrices of 320x240 pixels. These matrices contain the recorded value of the infrared radiation (IR). The number of matrices reported in the output depends on the frequency of data acquisition and on the time of acquisition. These parameters are set according to the peak velocity of the referred test. The selected frequency of acquisition of thermal data is 59.9Hz for sinusoidal tests and 1Hz for triangular tests.

The radiation that impinges on the IR camera lens comes from the target object and from its surroundings that have been reflected onto the object's surface. Therefore IR radiations are affected by external lights reflected in the test facility environment. Generally the radiations due to external lights are reflected on the stainless steel surface and their magnitude is always higher than the magnitude of the radiations due to the temperature rise only. For instance in Figure 67 are

visible the ambient sources which reflect on the polished stainless steel concave surface.

Consequently, it is not convenient to associate the data recorded with thermocouples directly with the total values of the IR radiations since this the calibration of the thermographic camera would result affected by the IR emissions reflected from ambient sources.

In the present study, the variations of temperature measured with thermocouples have been used to calibrate the variations of the IR radiations recorded at the end of each test with respect to the IR radiations obtained before the corresponding test. Such approach will prove useful in investigating the variations of temperature obtained during the test. In order to avoid the affection of the infrared energy detected with the reflected portion of the surface and to evaluate the correct target object temperature. is necessary to evaluate the emissivity of the object and to evaluate the contributions given by ambient sources and the emission from the atmosphere. The only emission from the object could be obtained by simply subtracting from the total radiation power received by the camera the effect of ambient sources and the reflectance of the object using the statement explained in the IR thermography section and the abstract from equation (5.7).

Therefore the variation of IR radiations will be evaluated by subtracting the recorded values measured during each test with the IR radiations recorded during a very slow velocity test in which the temperature rise is negligible. In fact, the external lights reflected on the stainless steel surface are approximately coincident for both tests compared since the subtraction is carried out for the same displacement configurations.

$$\Delta W_{obj} = W_{tot\_1} - W_{tot\_2} \tag{5.8}$$

Where W_{tot_1} is the total energy evaluated by the thermographic camera during each run and W_{tot_2} is the total energy in a low velocity test considered as the baseline for the calibration, respectively, in agreement with equation (5.6).

The ΔW_{obj} matrix obtained for each of the selected configurations will present values different by zero in those pixels effectively involved by heating, and approximately null values for the other pixels.

In the present section, the calibration of the relationship between the ΔW_{obj} radiations and the variation of temperatures recorded with the thermocouples will be discussed and validated.

The first step is to define a "baseline" matrix of the device, positioned in the configuration of null displacement, carried out before the start of the considered test. Since the IR radiations acquisitions started, for each test, approximately 2 seconds before the imposed motion, there are many frames describing the initial configuration of the device before the imposed motion. The cited frames are always characterized by some noisy fluctuations and so the first 5 frames of each test record have been averaged in order to obtain the required baseline representing the IR configuration before heating.

The next figure represents the matrix obtained after averaging the first 5 frames of the registration conducted for test 307.

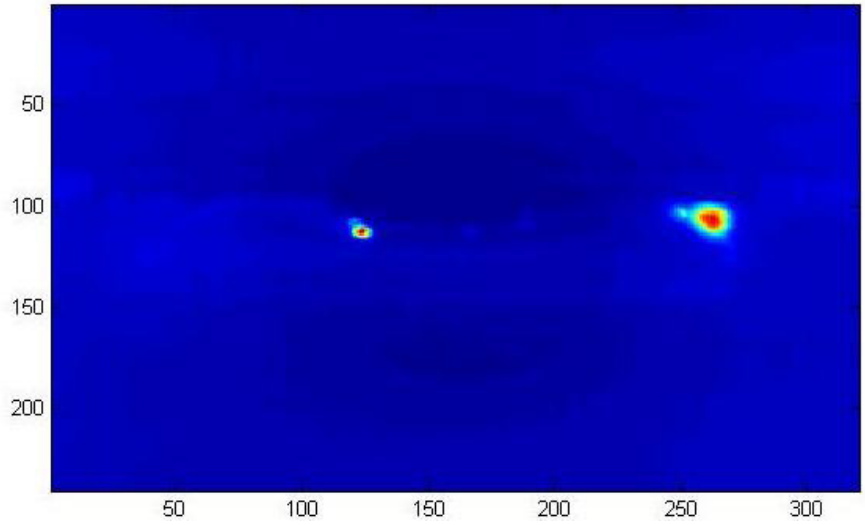

Figure 69: Thermographic camera image's before the run of test 307. It represents the matrix W_{tot_2}.

The image shown in Figure 69 refers to a null displacement configuration of the concave surface before the run of test 304. Obviously the contact surface does not involve friction and head generation, so the sinusoidal motion and the temperature rise consequently generated is null. The sliding stainless steel surface is at room temperature. In the same picture, it is possible to locate the headlights used during the tests.

It is evident that the representation of the total values of IR radiations would result in images impossible to read and analyze. These images would present many different reflections of lights due to the spatial motion of the device.

The following image illustrates the device disposed in the same spatial position after 50 seconds by the end of the applied motion.

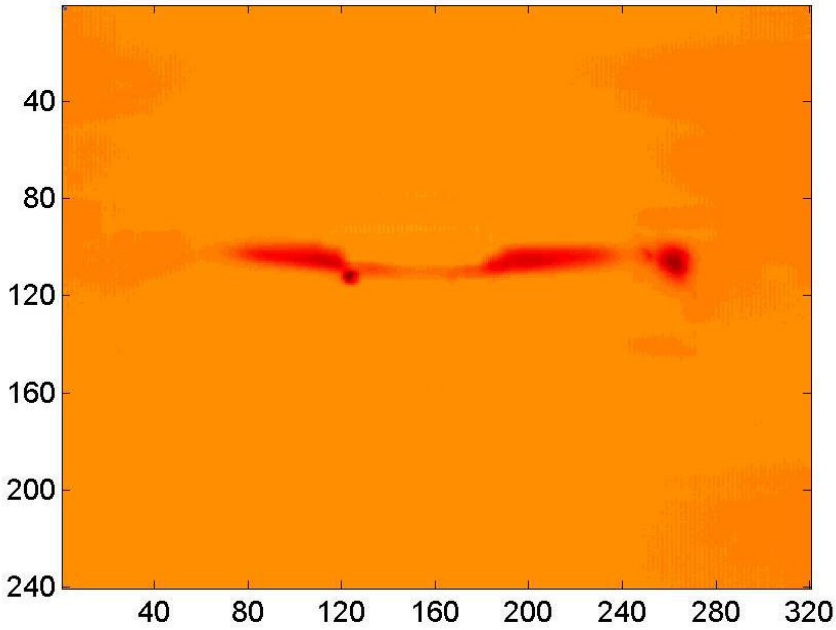

Figure 70: Static image of W_{tot_1} (total radiations with temperature rise of the object) taken 50 seconds after the end of test 304.

Figure 70 has been extrapolated 50 seconds after the end of the test because it corresponds to the last moment before which the operator started to record the thermocouple data, corrupting in this way the quality of the data registered. In Figure 71, the matrices previously shown have been subtracted and the resulting image is shown.

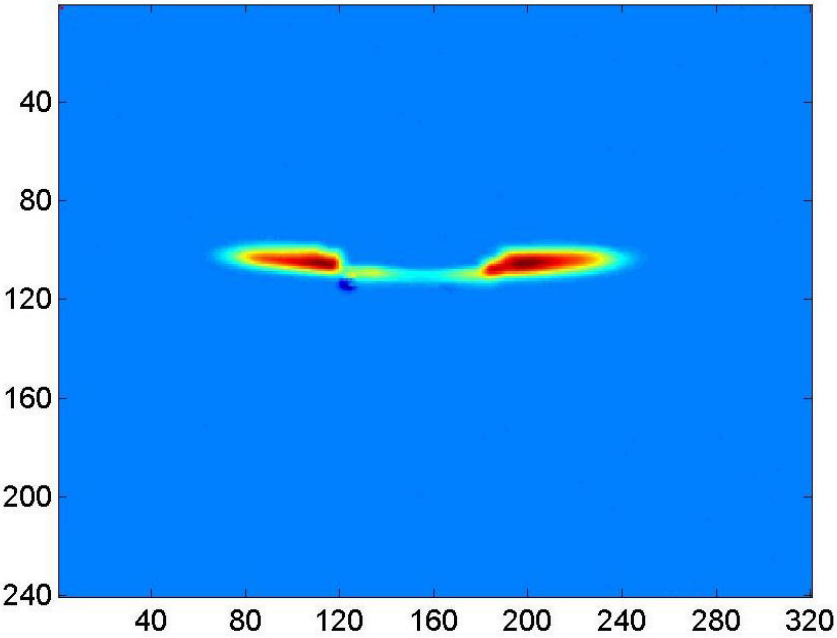

Figure 71: Representation with a contour plot of the ΔW_{obj} (variation of IR Radiations of the object) before and after test 304.

The image reported shows, with good definition and resolution, the spatial distribution of the variation of ΔW_{obj}, or rather the IR radiations on the concave surface.

It is important to observe that the variation is not exactly equal to zero for those pixels corresponding to the positions occupied by the slider. These positions should be covered and the corresponding variation of infrared radiation should be equal to zero. This can be described considering that the heat generated during motion is partially conducted through the depth of the materials involved in contact and the portion between the slider and the sliding surface located in the central part of Figure 71 is not blue.

In order to define the relationship between the ΔW_{obj} radiations and the temperatures registered with thermocouples, a statistical elaboration has been performed of ΔW_c, ΔW_m and ΔW_b extrapolated by small areas of 3x3 pixels corresponding respectively to the points at which the temperatures have been recorded. The referred areas, that are coincident to the points "s", "m", "b" previously defined, belong to the strips reported in Figure 72.

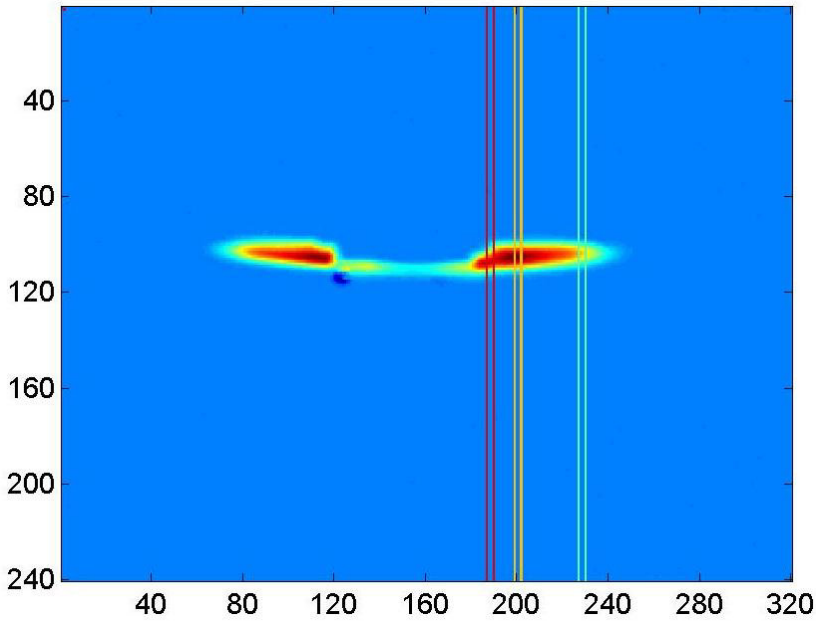

Figure 72: Position of selected areas on the concave surface.

The values of IR radiations, corresponding to 9 pixels for each of the 3 defined points, have been carried out for each frame belonging to the period 30-50 seconds after the start of registration. This data has been averaged with a standard deviation evaluated for every frame recorded in the defined period. The value of IR radiation selected has been obtained by the summation of two times the

standard deviation to the average value of the referred parameter. The resulting values of IR radiation have been combined with the corresponding values obtained from the elaboration of the baseline data, previously described.

The result is the following graph showing the decay of the variation of IR radiations in the range 1-70 seconds for all the points and tests elaborated:

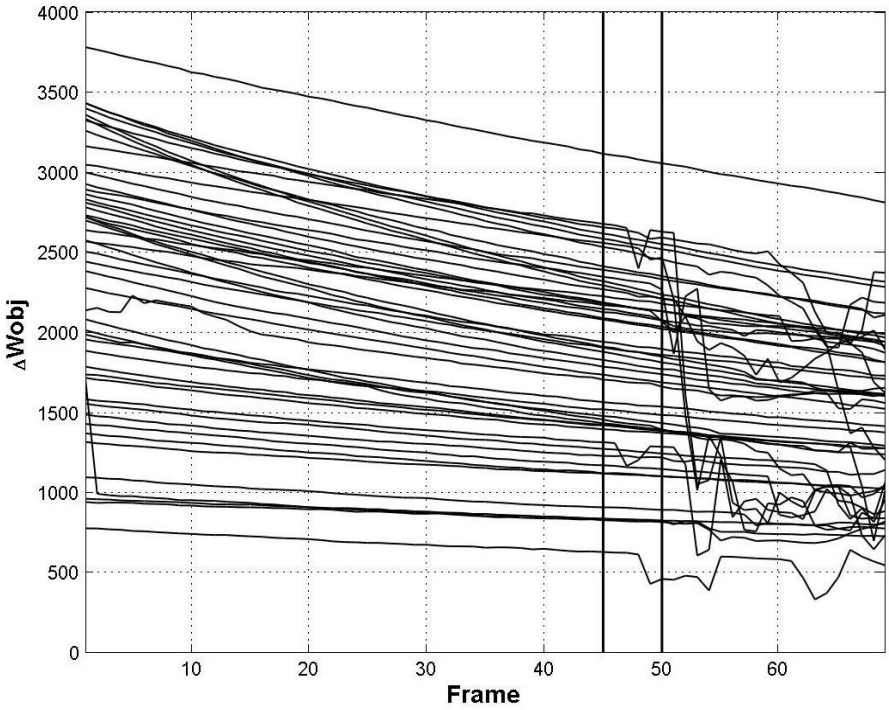

Figure 73: Variation of ΔW_{obj} from 1 up to 70 seconds after each test

It is evident that, for the selected time period, the values of the referred parameter have not been affected by the presence of the operator. After 50 seconds, however, the fluctuation of the curves are due to the disturbance caused by the operators.

The temperature rise recorded for each test for the selected points has been represented according to the corresponding value of DIR radiation.

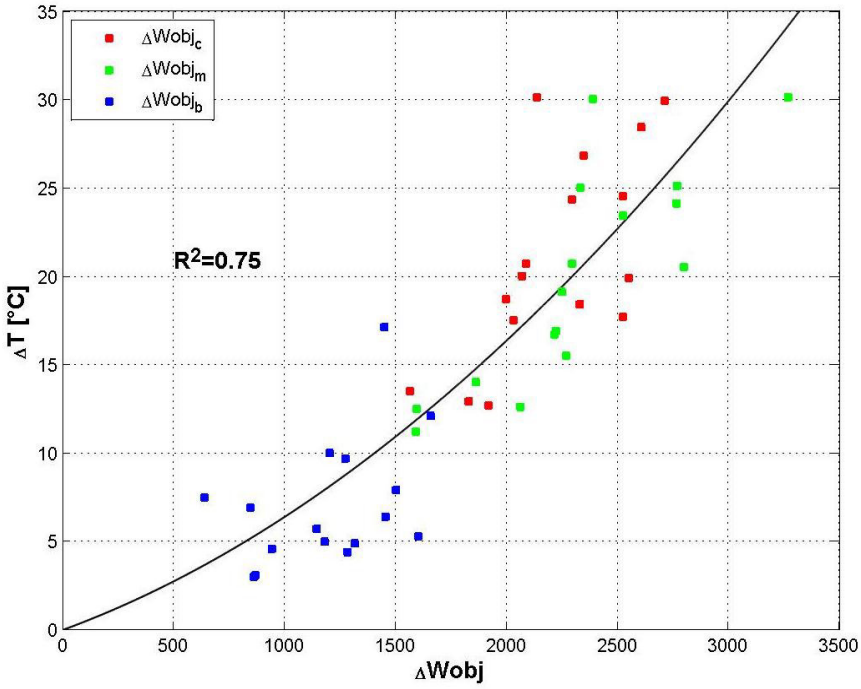

Figure 74: ΔW_{obj} - ΔT relationship and interpolation function.

The selected interpolating curve is the following second order polynomial function:

$$\Delta T = 0.0046 \cdot \Delta W_{obj} + 2.17 \cdot 10^{-6} \cdot \Delta W_{obj}^{\ 2} \qquad (5.9)$$

The determination factor R^2 between the experimental data and the values obtained with the previous equation is 0.75.

5.6. Characteristics of the tests executed and the Testing procedure

The calibration of equation (5.9) is used for converting the IR radiations data (ΔW_{obj}), obtained during each test by means of the thermographic camera, to the corresponding values of temperature rise involved during the motion.

Given the calibration of the relationship between the temperature rise and the corresponding variation of infrared radiations, the preliminary step of the present procedure requires the selection of a defined number of frames corresponding to particular positions of the slider moving on the concave surface. It is necessary to select frames both from the referred test and from a test ("baseline") that doesn't involve variations of temperatures.

Since the test selected as "baseline" is supposed to be very slow, and according to equations (4.10) and (4.11) the flash temperature is directly proportional to the velocity, it is considered reasonable to choose the triangular tests characterized by slow constant velocity and negligible temperature rise.

In fact, frames corresponding to particular displacements have to be selected from a sinusoidal test, characterized by particular values of sliding velocity and total testing time, and from the triangular "baseline" test which has a different shape, constant sliding velocity, and a different testing time (see Figure 63). Since the maximum imposed displacement is equal for all the executed tests, the selected frames correspond to the slider displaced of multiples of 1/20 of the maximum imposed displacement.

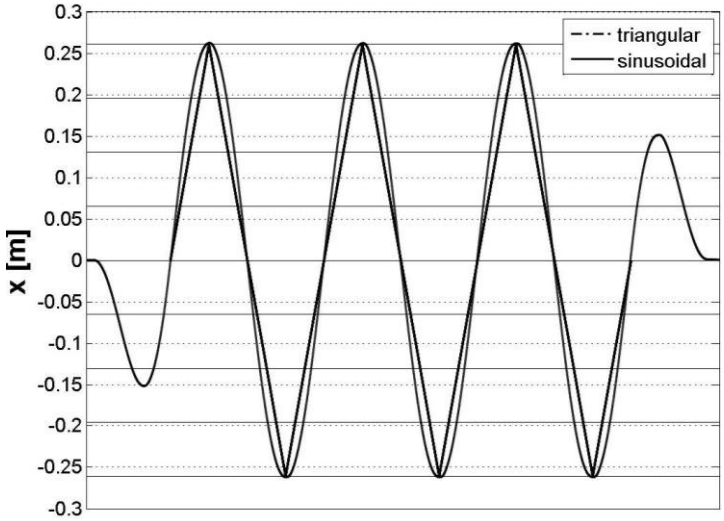

Figure 75: Example of selection of frames from tests of different shapes.

In order to make the above picture readable, the "sections" imposed to the displacement functions correspond to multiples of 1/4 of the total displacement.

Once the frames corresponding to the enter and exit displacement histories have been removed from the data associated with the sinusoidal tests, the matrices corresponding to the selected positions are subtracted and the DIR radiations obtained are converted to variations of temperatures by means of equation (5.9).

The frames selected from the 3 cycles of test 304 are presented below in order to describe the temperature variation that occurred during the corresponding test.

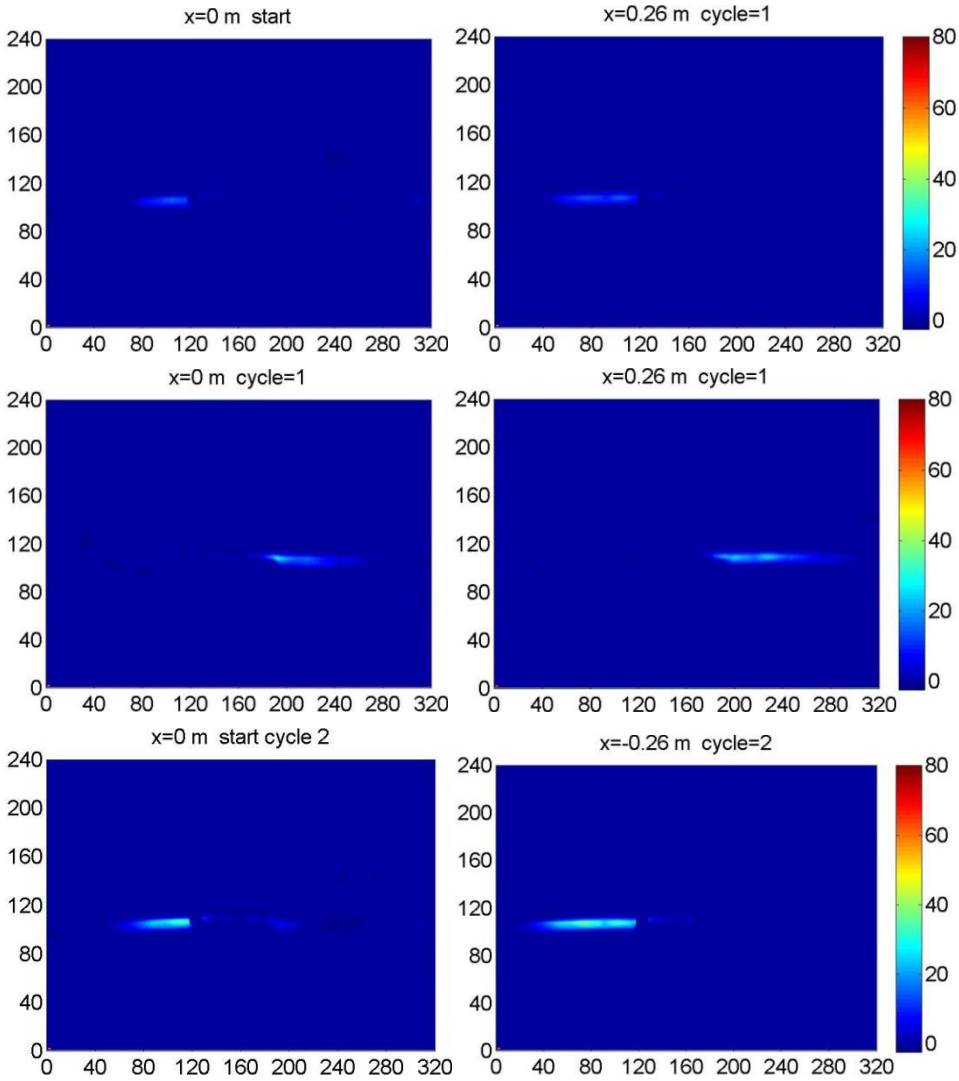
x=0 m start
x=0.26 m cycle=1
x=0 m cycle=1
x=0.26 m cycle=1
x=0 m start cycle 2
x=-0.26 m cycle=2
0 40 80 120 160 200 240 280 320
0 40 80 120 160 200 240
0 20 40 60 80

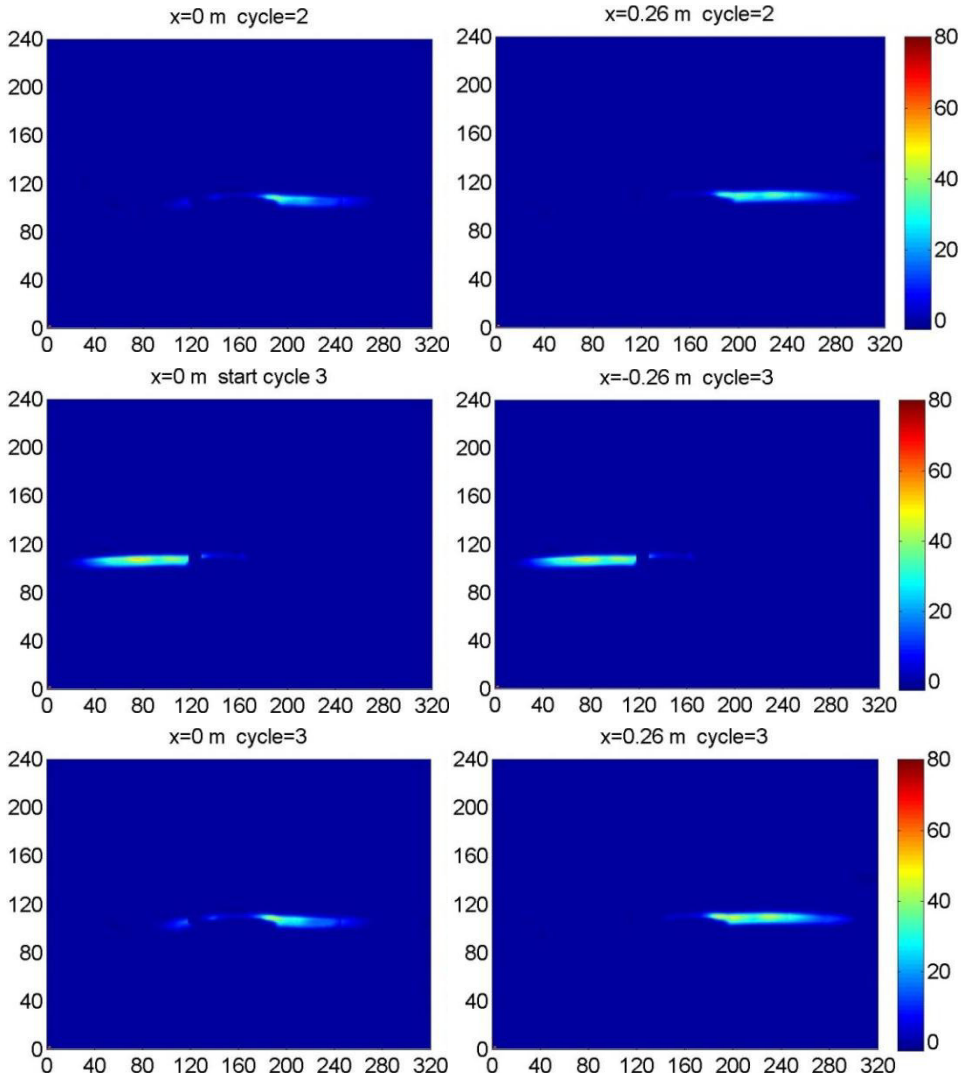

Figure 76: Temperature extrapolated from the thermographic camera. From the upper left frame to the downer right frame are reported three whole cycles of the test 304.

5.7. Results of Thermal Experiments

The present section describes the main features of the frictional heating of the experimental investigation according to the presented elaboration of the thermographic camera data.

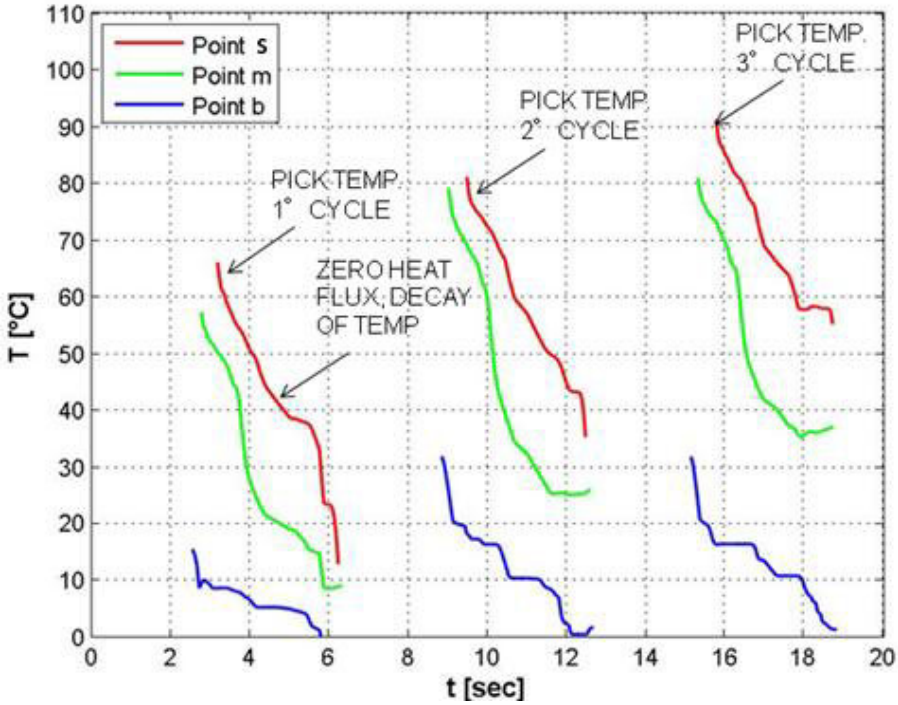

Figure 77: Thermographic camera data corresponding to point ”s” , “m”, “b” for test 304.

Figure 77 shows thermographic camera data corresponding to points ”s” , “m”, “b” for test 304. As the slider moves away from the observed point and opens up the thermographic camera’s field of view, the flash temperature is detected by the instrument and the curves start with a first value in the y axis. As

shown in Figure 77 the flash temperature rapidly increases in any spot of the sliding surface especially for the spot closer to the center of the isolator (point ‘s’). When the slider moves away the flash temperature appears to decay according to an irregular behavior.

This phenomenon can be explained considering the numerical evaluation of the pixels selected in order to describe the required temperature variation. In fact, according to the reported testing procedure, the sinusoidal movement is directly applied to the concave surface while the slider and the upper portion of the device are restrained with respect to the horizontal movement. For this reason, it has been necessary to automatically change the observed pixels according to the instant position of the surface on the screen. The pixels selected for each of the elaborated frames have been marked in Figure 78. The pixels observed present some fluctuation with respect to the expected one.

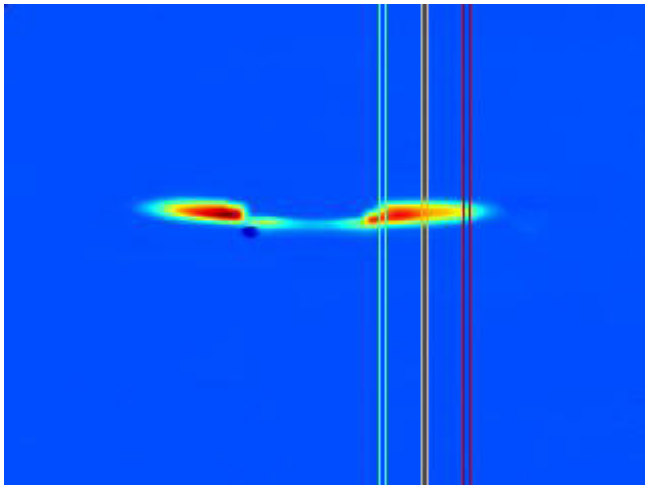

Figure 78: Selected pixel in the sliding surface for the evaluation of the experimental flash temperature.

In Figure 77, is possible to identify a pick value and a decay of temperature for each curve. The pick value represents the flash temperature in 's', 'm' and 'b' points of the sliding surface when it comes out of contact with the polymer liner. Since the points lose contact with the rubbing surface they show a relevant decrease of flash temperature. During the motion the temperature gradient between the top and the bulk of the stainless steel layer increase as long as the contact is maintained, reaching the pick value represented in picture. Afterwards for the first cycle it drops from 68°C to 12°C from 58°C to 10°C and from 15°C to 0°C for points 's', 'm' and 'b', respectively. It is noticed that this drop of temperature $T_{f,pick,i} - T_{f,min,i}$ decreases cycle by cycle and that $T_{f,pick,1cycle} > T_{f,pick,2cycle} > T_{f,pick,3cycle}$ .This effect can be considered as a cumulating effect of the heat transfer coupled with a consequent increment of bulk temperature of the stainless steel layer.

Figure 79 illustrates the temperature histories referred to the central point "s" for 3 different tests:

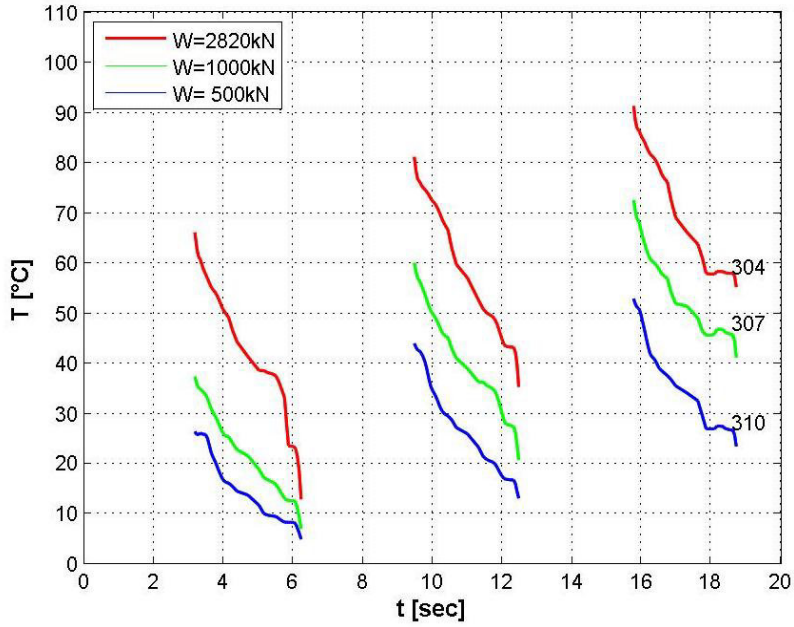

Figure 79: Thermographic camera data corresponding to point "s" for tests 304-307-310.

Figure 79 shows the variation of the maximum temperatures according to the imposed normal load. The red line corresponds to test 304 which is characterized by the maximum applied load of 2820kN corresponding approximately to 45MPa. The peak velocity of the referred test is 260mm/s. The green and the blue lines describe the variation of temperature on the same position during tests that have applied normal loads of 1000kN and 500kN respectively. Figure 79 clearly denotes how the temperature rise is strictly related with the pressure applied on the sliding surface. In fact, as reported in Table 6, the three tests represented in Figure 79 have the same sinusoidal input, the same instant velocity and consequently the time test. The only difference is given by the applied pressure. Therefore the flash

temperature has a relationship with the pressure that appears in the experimental curves.

In Figure 80 the temperature variation of point “s” is described for 3 tests carried out according to the same values of vertical load and different peak velocities.

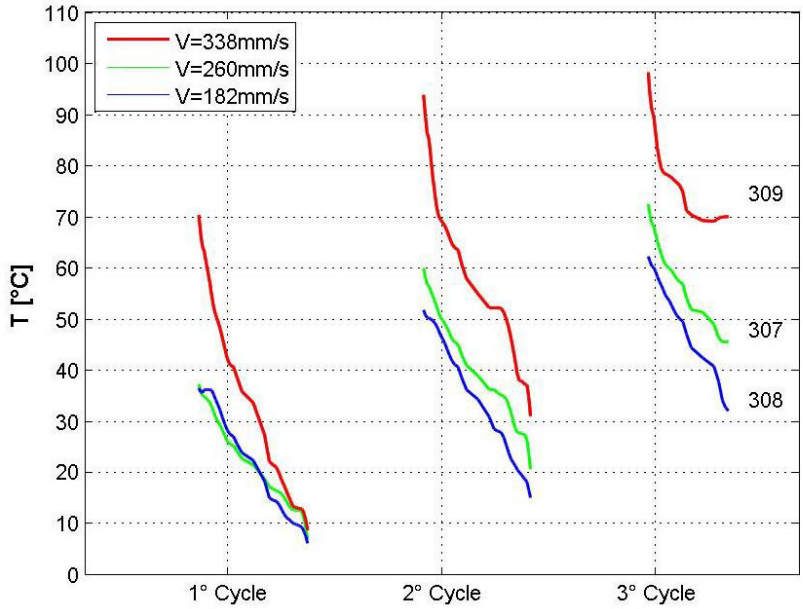

Figure 80: Thermographic camera data corresponding to point ”s” for tests 307-308-309.

To better understand the dependence of the temperature rise with the pick velocity in Figure 80 the curves have a ‘x’ axis shifted. This graph shows that the temperature rise is strictly dependent on the variation of the sliding velocity and the applied normal load. As these parameters are increased, the thermally dissipated energy per unit time increases and the temperature variation becomes more evident.

Figure 80 indicates that, for a given applied normal pressure, the variation of temperature is mainly due to the sliding velocity. The temperature rise evaluated for point “m” is very close to the corresponding one calculated for point ”s” because the variation of the sliding velocity of the slider passing through the above mentioned points is less relevant than the velocity imposed to the slider while it passes through the point “b”.

The flash temperature picks for the three points of the slider surface (‘b’, ‘m’ and ‘s’) have been selected from the graphs shown above, and then have been collected in Table 8. To allow a comparison between the maximum flash temperature values, Table 9 outlines the flash temperature picks selected for 1°,2° and 3° cycles for the point ‘s’ with the result being the point most subjected to the heat transfer.

Table 8: Flash temperatures pick selected for 1°,2° and 3° cycle obtained with thermographic camera elaboration for series 300 and 400 and for points ‘s’ ‘m’ ‘b’.

	1° Cycle			2° Cycle			3° Cycle		
Test	**Border**	**Mid**	**Slider**	**Border**	**Mid**	**Slider**	**Border**	**Mid**	**Slider**
[n°]	[°C]	[°C]	[°C]	[°C]	[°C]	[°C]	[°C]	[°C]	[°C]
304	15,5	59,5	66,0	31,9	79,0	81,0	31,8	80,8	91,1
305	22,4	37,0	37,1	10,1	47,0	53,9	5,9	48,8	66,8
307	11,0	30,3	37,3	16,8	48,7	59,9	17,6	50,4	72,4
308	14,7	32,6	36,7	13,5	44,4	50,1	12,9	48,9	59,0
309	20,1	56,1	59,5	30,7	73,4	91,8	33,9	82,7	104,3
310	8,6	18,7	26,4	14,0	31,4	43,9	14,5	33,5	52,8
404	21,6	56,8	45,3	36,2	88,3	67,7	38,2	108,9	83,8
405	12,5	48,1	52,1	14,0	77,3	74,7	13,0	94,5	91,7
406	14,5	76,0	83,0	13,7	115,0	110,2	14,5	116,9	131,4
407	34,2	43,3	40,6	43,0	63,4	60,2	47,4	86,3	77,6
408	21,4	24,2	30,6	12,5	55,7	65,5	11,9	72,7	79,8
410	5,7	30,6	30,2	8,5	63,7	54,3	10,0	80,7	68,0
411	4,5	25,4	30,4	6,3	49,9	45,3	6,4	59,9	52,4

Table 9: Flash temperature picks selected for 1°, 2° and 3° cycle obtained with thermographic camera elaboration for series 300 and 400 and for points 's'.

		T_{f_slider} 1° Cycle [°C]			T_{f_slider} 2° Cycle [°C]			T_{f_slider} 3° Cycle [°C]		
Series	V (mm/s)	p=8 MPa	p=16 MPa	p=45 MPa	p=8 MPa	p=16 MPa	p=45 MPa	p=8 MPa	p=16 MPa	p=45 MPa
300	182	\	36,7	37,1	\	50,1	53,9	\	59,0	66,8
	260	26,4	37,3	66,0	43,9	59,9	81,0	52,8	72,4	91,1
	338	\	59,5	\	\	91,8	\	\	104,3	\
400	182	30,4	30,6	45,3	45,3	65,5	67,7	52,4	79,8	83,8
	260	30,2	40,6	52,1	54,3	60,2	74,7	68,0	77,6	91,7
	338	\	\	83,0	\	\	110,2	\	\	131,4

Data collected in Table 8 and Table 9 have been represented in a graph in order to evaluate a qualitative relationship between the increase of flash temperature and the mechanical parameters of the tests.

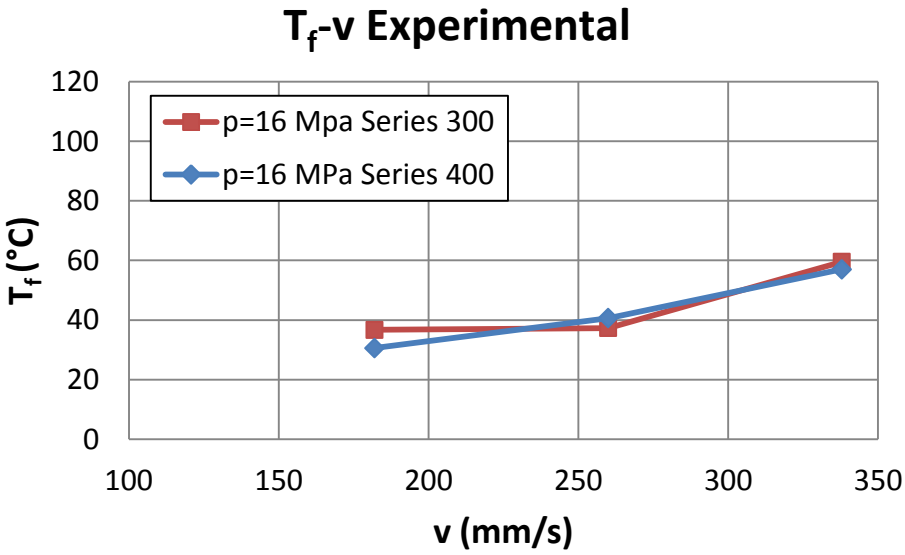

Figure 81: Experimental dependency of Flash Temperature on velocity.

Figure 81 depicts the trend of flash temperature versus the instant pick velocity with a constant apparent pressure of 16 MPa for test series 300 and 400. The experimental Flash temperature evaluated with the thermographic camera shows a dependency on the velocity of the test according with equation (4.13).

In accordance with this equation, Figure 82 show the experimental dependency of flash temperature with apparent pressure. At high pressures (45 MPa), the flash temperature is double that measured with low pressure test (8 MPa).

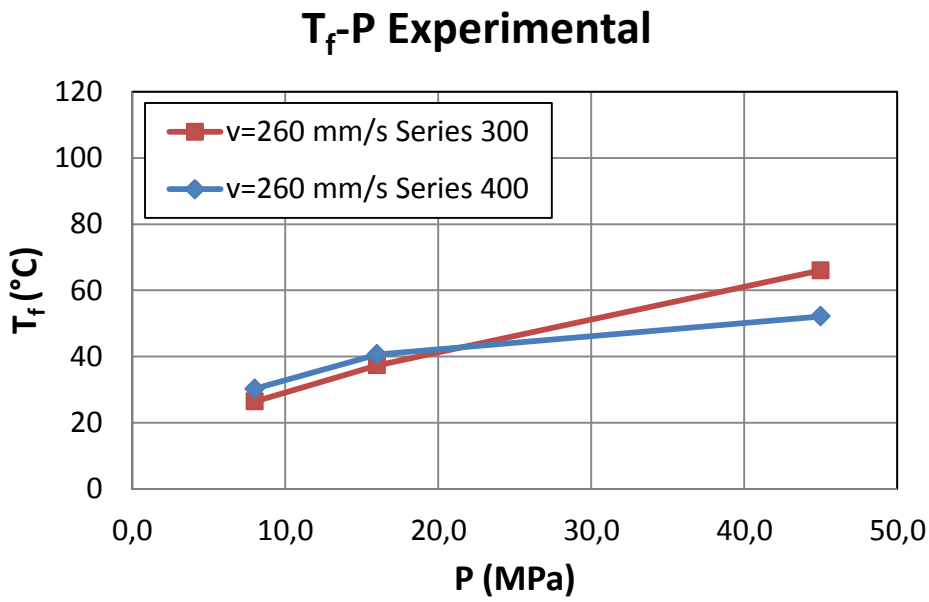

Figure 82: Experimental dependency of Flash Temperature on apparent pressure.

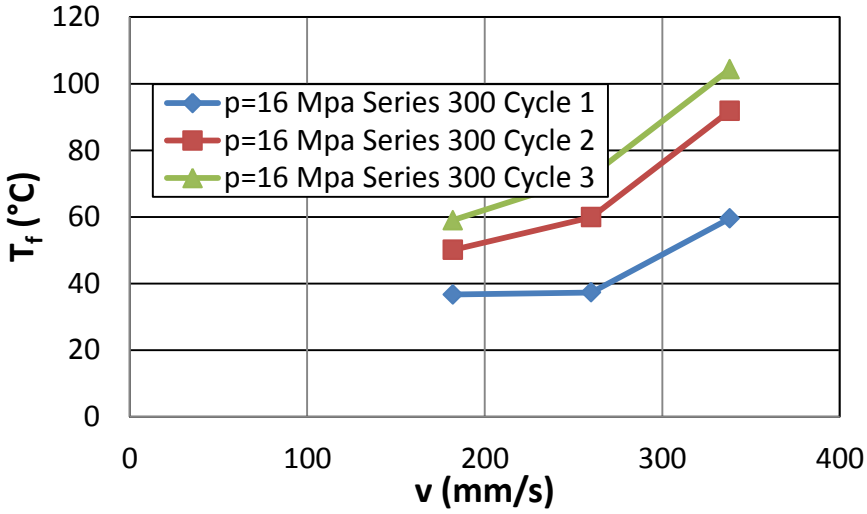

Figure 83: Effect of velocity and cumulated motion to Flash Temperature.

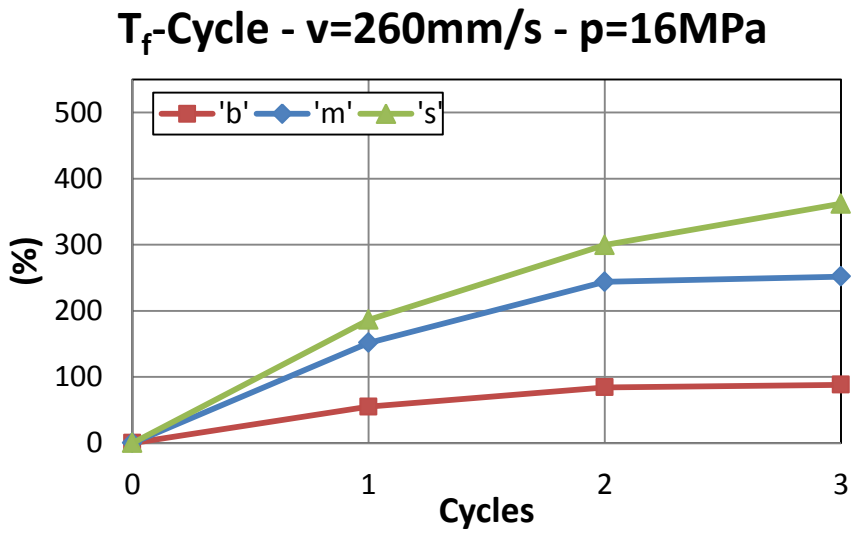

Figure 84: Effect of cumulated motion to Flash Temperature in % referred to the initial condition room temperature = 20°C.

Figure 83 shows the effect of cumulated short motion. The rubbing of the high strength polymer liner with the selected spots ‘b’, ’m’ and ‘s’ produces a cycling effect due to the accumulation of heat in the stainless steel layer which changes, cycle by cycle, the thermodynamic boundary condition of the problem at the start of a new cycle. For that reason it is expected an increment of bulk temperature of stainless steel layer. In Figure 84 is represented the increment in % of the flash temperature for p=16 MPa and v = 260mm/s versus the cycle. The room temperature for each test is considered equal to 20°C. As shown in Figure 84 the rate of increment decreases cycle by cycle and 50% of increment is concentrated in the first cycle.

The instant velocity on the contact surface of the friction pendulum changes because of the sinusoidal shape of the input. This means that only when the slider passes through the central point of the sliding surface does the velocity reach its peak value. Conversely when the slider reaches the maximum displacement of 260mm the velocity is zero Figure 85 shows the flash temperature in three different spot of the sliding surface for different max pick velocities. In ‘s’ the dependency of the flash temperature to the instant velocity is more marked, as expected. On the border of the slider, even though the rate of the increment is less than in ‘m’ and ‘s’, there is an increment of the flash temperature for a test with a higher instant pick velocity. This could mean that either the deceleration or the stick slip, or both effects together, generate substantial eccentricity and overturning moments on the slider, and so, an extra pressure on the contact surface arises, in the outer part of the slider.

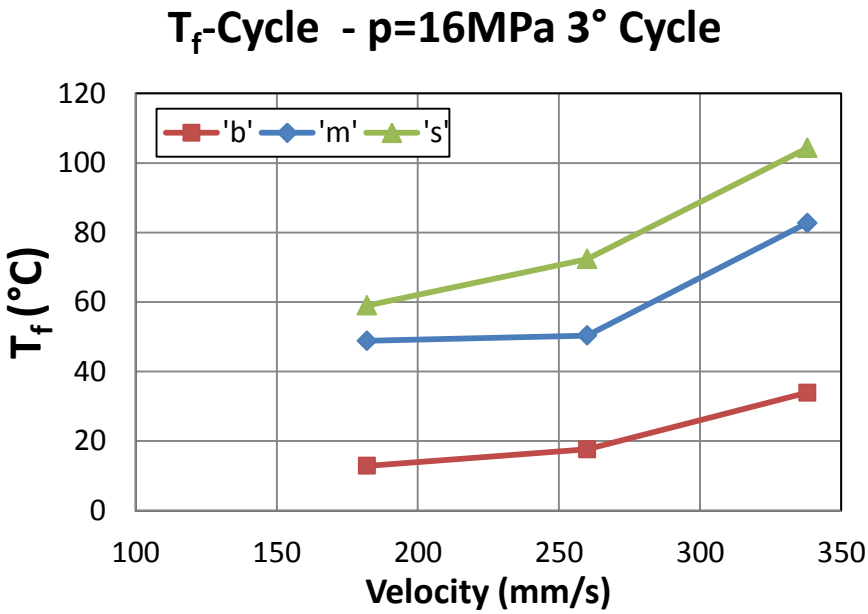

Figure 85: Maximum variation of the flash temperature (3rd Cycle) in 'b', 'm' and 's' versus velocity.

By using the measured temperature at the three different points shown in Figure 86 and assigning $x_{border} = 85mm$, $x_{medium} = 174mm$ and $x_{slider} = 261\ mm$, it is possible to represent the flash temperature profile along the sliding surface (Figure 87, Figure 88 and Figure 89).

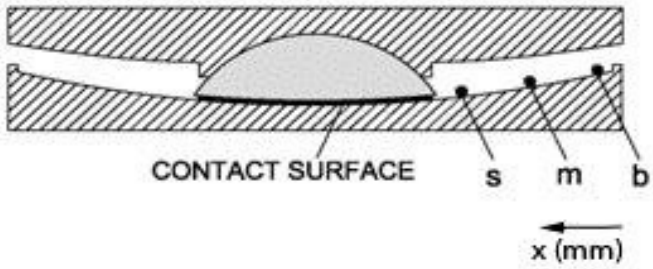

Figure 86: Position of the selected points in the sliding surface 's', 'm' and 'b'.

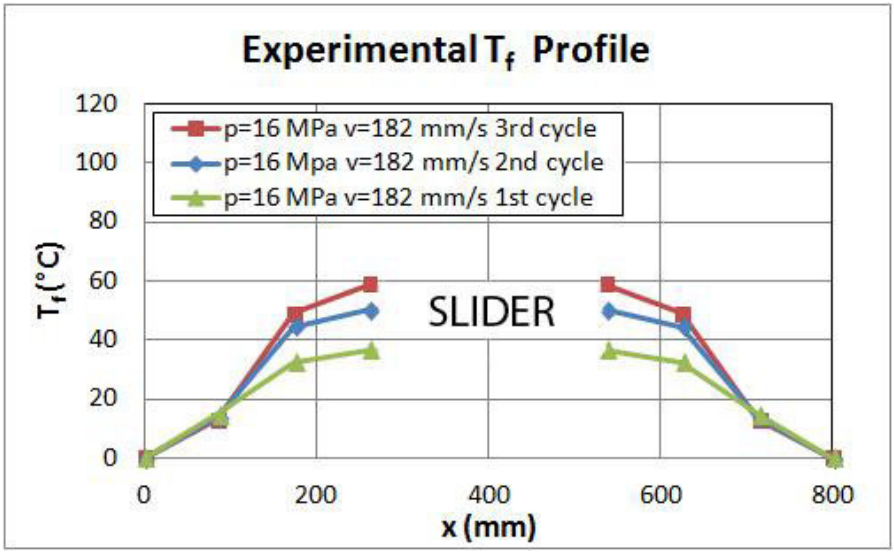

Figure 87: Experimental Temperature profile on the slider surface at the end of each cycle for p=16 MPa and v=182 mm/s.

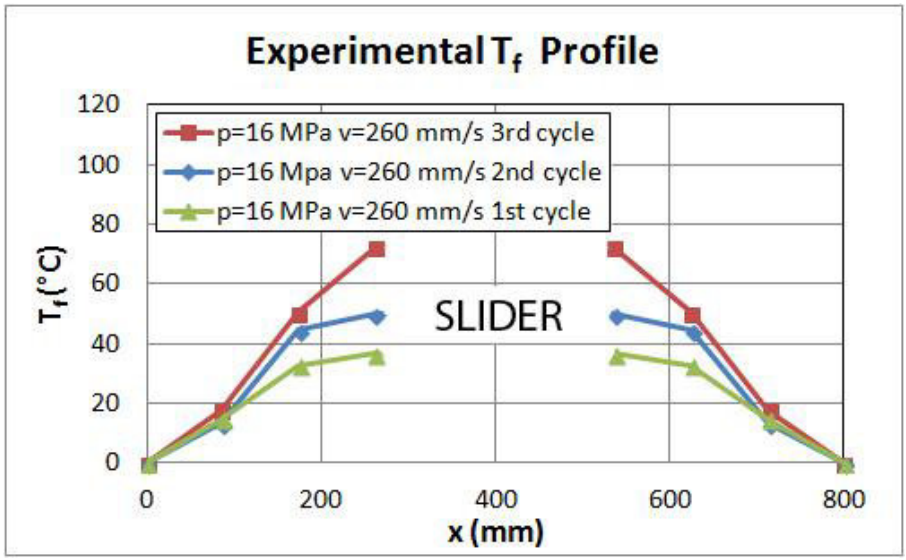

Figure 88: Experimental Temperature profile on the slider surface at the end of each cycle for p=16 MPa and v=260 mm/s.

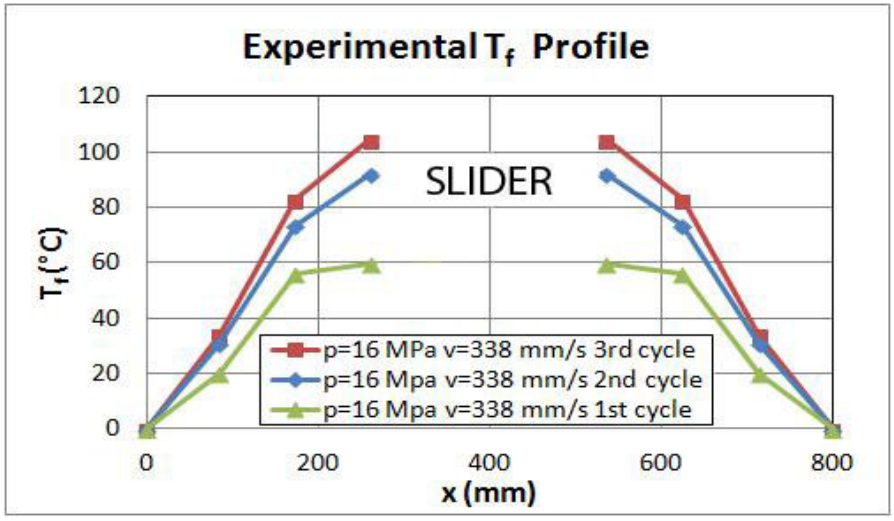

Figure 89: Experimental Temperature profile on the slider surface at the end of each cycle for p=16 MPa and v=338 mm/s.

From the analysis of these experimental results is possible to make a number of important statements that are valid for high strength-stainless steel contacts surface and for the parameters used in this experimental analysis.

- The experimental flash Temperature evaluated with the thermographic camera depends on pressure and velocity with a rate reported in Figure 81 and Figure 82.
- The flash temperature significantly increases with higher velocity and higher pressure. The maximum value reached in the test series is 131.4 °C.
- Cumulative short motion causes an accumulation of heat on the slider and on the sliding surface and, as a consequence, the parameter T_f is subjected to a 'cycling effect'. The rate of increment decreases cycle by cycle, and 50% of the increment is concentrated in the first cycle (Figure 84).
- The increment of temperature is not constant along the sliding surface and is more pronounced in the central part of the slider rather than in the border of the sliding surface. This is basically due to the variation of instant velocity in the contact surface (Figure 85).

In the central part it was not possible to evaluate the flash temperature because of a blind spot due to the dimension of the slider. A further increment of T_f in this central area of the sliding surface is expected according with the trend reported in Figure 87-Figure 89

.

Chapter 6

6. Comparison between experimental and analytical test

The theory of Carslaw and Jeager explained in Chapter 4 is in this section applied with the experimental test described in Chapter 5. Therefore, in order to validate the prediction reliability of this theory measured experimental flash temperatures (see Table 7) have been used here.

As shown in chapter 4, the equation (4.17) is used to estimate the flash temperature on the top of the sliding surface ($x = 0$):

$$T_f(x,t) = \frac{D^{1/2}}{\pi^{1/2} k} \int_0^t q(t-\tau) \frac{d\tau}{\tau^{1/2}} \quad \textbf{(6.1)}$$

In the test protocol the maximum displacement of the sinusoidal input is $u_s = 260\,mm$, the diameter of the plane projection of the sliding surface is $810\,mm$ while the plane projection of the slider is $2a = 275mm$. These conditions are referred to large displacement $u_c > a$ as represented in figure 53. The temperature rise at the sliding contact depends on the heat flux q generated, given by eq.(4.10). The heat flux history is evaluated at the same fixed position in the sliding steel surface considered in Figure 64. The heat flux history at the selected fixed spots of the steel part depends on the history of the displacement and the size of the apparent contact area. Therefore, for all the intervals of time in

which the contact area moves away of the selected fixed area, the heat flux will be zero according to this condition:

(6.2) $$\text{cond.} = \sqrt{\left(x - \bar{x}_i\right)^2 + \left(y - \bar{y}_i\right)^2} \le A_s / 2 \quad \text{cond.} = 1$$

$$\text{cond.} > A_s / 2 \quad \text{cond.} = 0$$

Where $(\bar{x}_i, \bar{y}_i)$ represents the coordinate of 's', 'm' and 'b' spots on the sliding surface and a the projection of the diameter of the slider on the horizontal plane.

For those intervals in which the resultant displacement u_s is larger than a (the radius of sliding surface $a = 137{,}5\ mm$) the condition (6.2) is not satisfied and the heat flux is zero ($q \cdot cond = 0$).

Figure 92 presents the analytical evaluation of flash temperature in the three spots 's' 'm' and 'b'. The large displacement condition in these tests ($u_c/a = 1.89$) are those of intermittent heat flux for which the history of temperature has consecutive build-up and decay intervals.

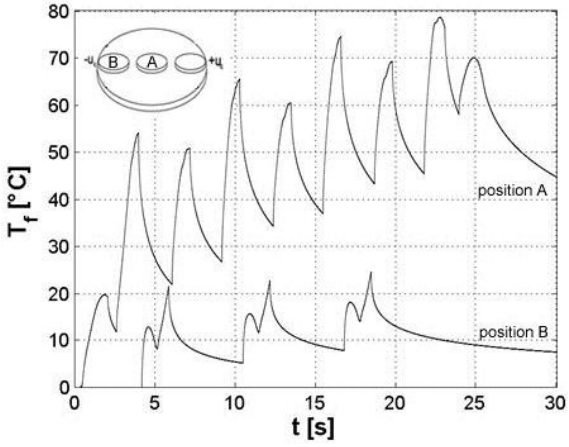

Figure 90: Comparison between temperature for a central position A and a border position B on the sliding surface.

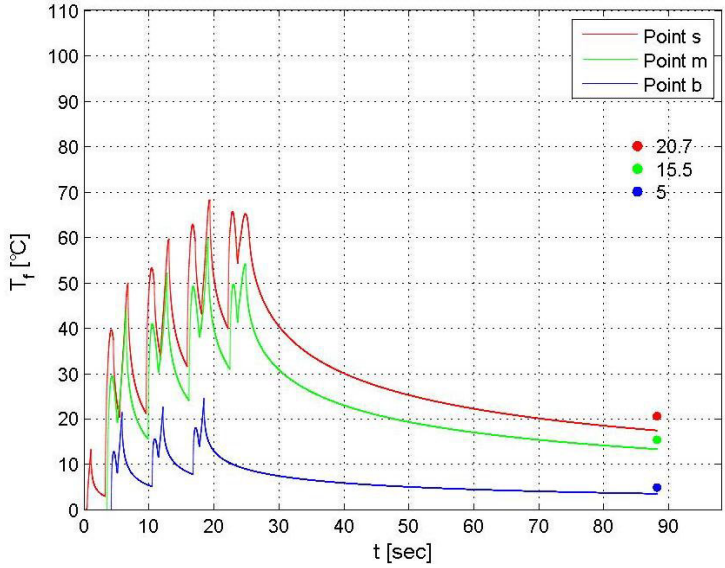

Figure 91: Analytical evaluation of temperature rise of the controlled points in test 204.

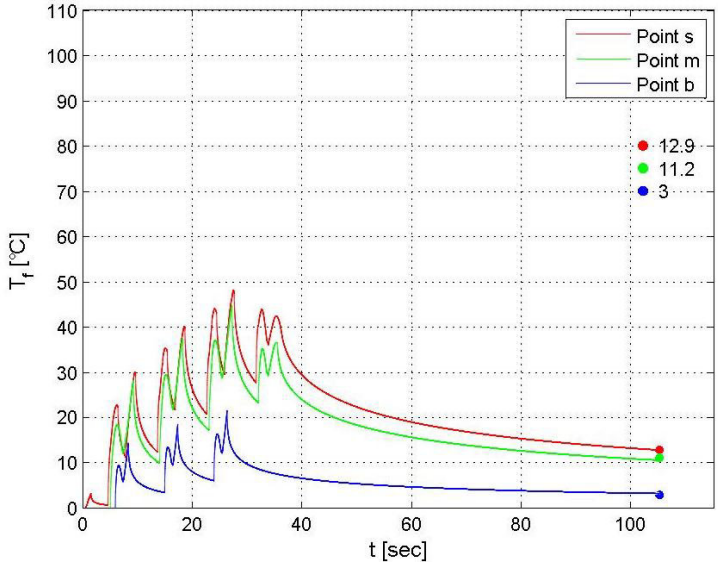

Figure 92: Analytical evaluation of temperature rise of the controlled points in test 411.

The prediction of the temperature has been made considering three different sinusoidal input and apparent pressure respectively. The heat flux was calculated using the measured coefficient of friction during the test.

In Figure 92 are depicted rounded markers which represent the flash thermocouple temperature measured at 50s after the end of the test. The comparison of the continuous lines at $t_{test} + 50s$ and these spots demonstrates that the calculation predicts reasonably well the measured temperature, although in some cases it overestimates and in other cases it underestimates the measured value. The discrepancies between the analytical temperature and the experimental one it could be referred of the loading arrangement and the actual pressure distribution at the contact surface with is not constant like assumed in the theory. The measurement of the thermocouple is made in a single point and it is unknown whether this point is representative of the average conditions at the surface.

With respect to the thermal images carried out with the thermographic camera, the analytical representation of the temperatures rise involved during motion appears to be very useful because it allows the understanding of the temperature variation even when the slider is positioned on the selected points. In this way, the variation of temperature is carried out for each instant and an evaluation of the relationship between the variation of temperatures and the decay of friction coefficient is allowed.

The results obtained through the application of the described theory are in good agreement with the results illustrated in Constantinou et al. [1995]. The average errors affecting the analytical results with respect to the experimental data are of the magnitude of 30% in both cases. The Flash temperatures picks selected for 1°,2° and 3° cycle obtained with analytical test are reported in Table 10.

Table 10: Flash temperatures picks selected for 1°,2° and 3° cycle obtained with analytical test.

	1° Cycle			2° Cycle			3° Cycle		
Test	**Border**	**Mid**	**Slider**	**Border**	**Mid**	**Slider**	**Border**	**Mid**	**Slider**
[n°]	[°C]	[°C]	[°C]	[°C]	[°C]	[°C]	[°C]	[°C]	[°C]
204	21,5	44,3	49,9	22,7	52,1	62,9	24,6	59,8	68,2
205	17,0	33,6	37,2	18,8	46,5	59,3	21,9	55,0	64,4
206	20,8	42,3	47,8	23,3	56,9	72,8	26,4	65,2	76,8
207	15,6	30,8	32,5	16,0	37,6	47,3	17,6	45,4	51,4
208	11,2	23,2	25,4	12,9	33,0	41,7	15,0	39,4	45,4
209	13,9	28,5	31,1	16,9	41,5	51,7	19,4	48,6	55,1
210	9,9	18,3	20,5	11,4	25,3	31,1	12,9	29,9	33,2
211	8,6	15,1	16,6	10,5	23,9	29,2	12,3	28,6	31,5
212	11,3	20,8	22,2	13,3	30,2	36,4	15,7	35,0	37,5
Test	**Border**	**Mid**	**Slider**	**Border**	**Mid**	**Slider**	**Border**	**Mid**	**Slider**
[n°]	[°C]	[°C]	[°C]	[°C]	[°C]	[°C]	[°C]	[°C]	[°C]
304	41,0	69,8	71,9	40,0	74,8	79,5	40,8	80,5	84,7
305	34,2	59,9	62,5	35,2	68,1	74,4	37,5	75,3	80,4
306	41,6	81,2	87,3	43,5	88,4	97,1	13,6	42,5	91,4
307	27,1	48,4	50,7	29,4	57,1	61,2	31,8	64,1	67,8
308	23,9	44,2	47,3	26,4	52,3	57,2	28,8	58,5	63,0
309	31,9	57,6	60,3	33,3	65,6	73,0	35,3	72,0	77,0
310	20,4	36,2	37,3	22,1	42,6	44,7	23,9	48,3	50,8
311	17,2	31,6	33,1	18,8	37,1	40,5	20,7	41,9	44,5
312	23,2	43,3	45,6	25,0	50,2	55,1	27,2	56,9	61,1
Test	**Border**	**Mid**	**Slider**	**Border**	**Mid**	**Slider**	**Border**	**Mid**	**Slider**
[n°]	[°C]	[°C]	[°C]	[°C]	[°C]	[°C]	[°C]	[°C]	[°C]
404	45,8	63,4	61,4	43,2	72,3	76,6	44,7	80,7	82,4
405	29,1	52,1	56,8	34,3	65,0	76,3	38,3	74,4	80,6
406	36,8	63,3	68,3	42,1	77,9	92,4	47,0	87,0	92,4
407	22,3	42,0	48,8	25,1	51,2	59,7	27,9	59,1	68,5
408	17,2	37,3	42,8	22,8	48,7	59,2	27,2	57,5	65,2
409	24,4	46,9	52,9	30,1	59,3	70,1	35,5	68,5	75,1
410	16,6	32,5	35,0	20,6	41,2	48,5	23,9	49,4	53,8
411	14,5	28,3	30,1	18,6	37,6	44,1	21,7	44,7	48,1
412	19,2	36,2	39,4	24,0	46,5	54,2	27,5	53,2	57,4

In Figure 93-Figure 96, the analytical temperature history is compared with the experimental data obtained with the thermographic camera. Figure 93 shows a comparison with respect to the analytical evaluation for test 304:

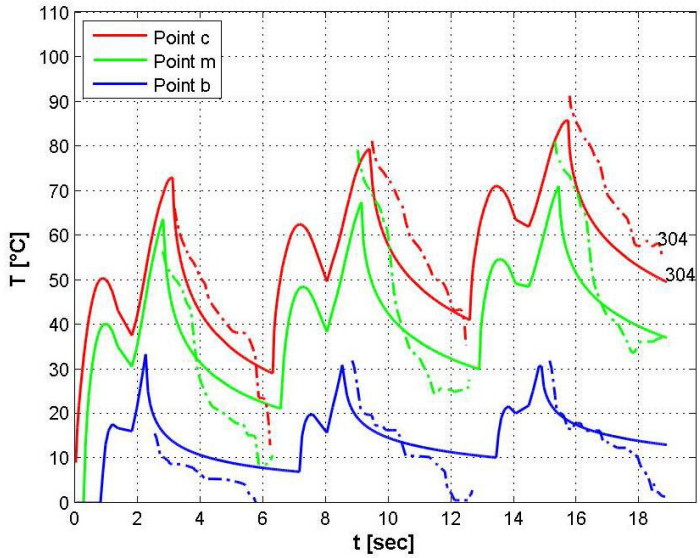

Figure 93: Analytical evaluation of temperature rise history of the controlled points during test 304 and comparison with the thermographic camera data.

Figure 93 shows that the results obtained analytically are in good agreement with the experimental data. The temperatures recorded by means of thermographic camera are consistent with the theoretical ones.

The described error can be attributed to the evaluation of the relationship between the recorded temperatures and the infrared radiations recorded with the thermographic camera.

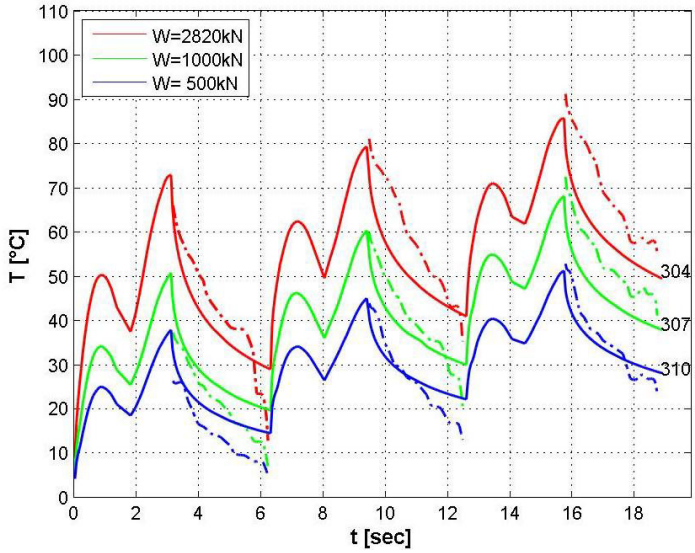

Figure 94: Thermographic camera data corresponding to point ”s” for tests 304-307-310 compared with the analytical evaluation of the temperature rise.

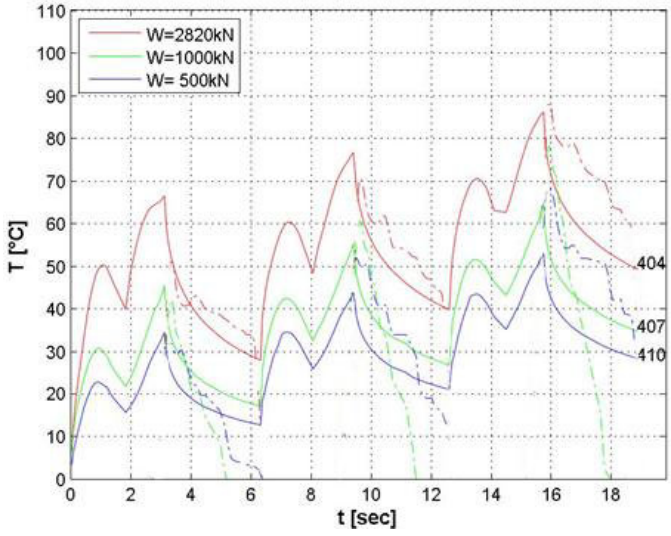

Figure 95: Thermographic camera data corresponding to point ”s” for tests 404-407-410 compared with the analytical evaluation of the temperature rise.

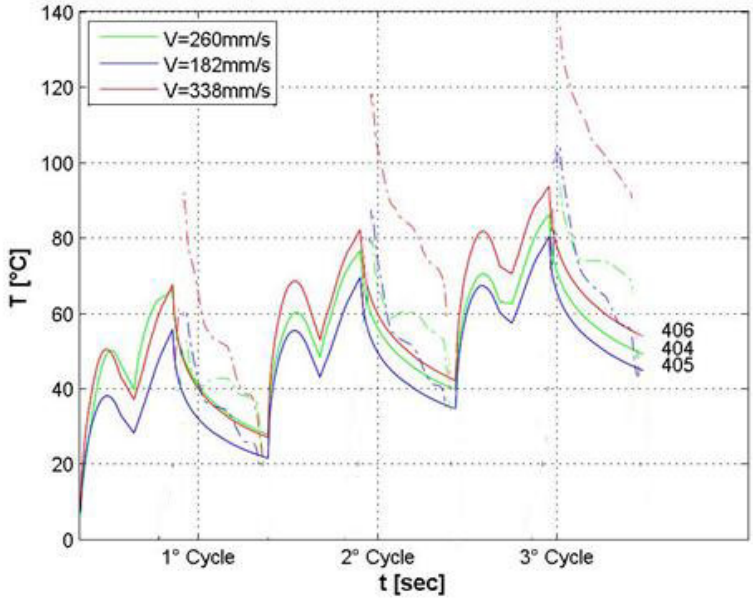

Figure 96: Thermographic camera data corresponding to point ”s” for tests 404-405-406 compared with the analytical evaluation of the temperature rise according with Carslaw and Jaeger’s theory.

The analytical prediction made with Carslaw and Jeager’s theory, is agreement with both the peak temperature values and the trends in the histories of temperature although there is a small difference between analytical and experimental values of time at which the peak temperature occurs.

In the graph there are differences in the measured histories of temperatures during the intervals of zero heat flux. In Table 11 are represented the errors between analytical and experimental flash temperatures in term of percentage and the values range between -20% and +20%.

Table 11: Errors between Analytical and Experimental flash temperature in %.

		Analytic-Experimental Err. values 1° Cycle [%]			Analytic-Experimental Err. values 2° Cycle [%]			Analytic-Experimental Err. values 3° Cycle [%]		
Series	V (mm/s)	p=8 Mpa	p=16 Mpa	p=45 Mpa	p=8 Mpa	p=16 Mpa	p=45 Mpa	p=8 Mpa	p=16 Mpa	p=45 Mpa
400	182	-1,0	28,5	20,2	-2,6	-9,6	11,3	-8,2	-18,3	-3,8
	260	13,7	16,8	14,7	-10,7	-0,8	2,5	-20,9	-11,7	-10,1
	338	\	-7,2	-17,7	\	\	-16,2	\	\	-29,7

Chapter 7

7. Friction Model for Sliding Bearing

Through experimental tests were carried out with single pendulum bearings (see chapter 5) in order to obtain a phenomenological model able to access the real performance of the friction pendulum and access the variation of the friction coefficient with temperature rise.

In this section, an extension of the degradation model based on Lomiento et al. 2012 described in section 3.3 is given. This study provides a model that takes into account mechanical variables such as apparent pressure, instant velocity, and also the degradation of dissipative characteristics of a friction pendulum due to the flash temperature that increases in the contact surface during dynamics conditions.

For the evaluation of the decay of the dissipative characteristics of friction pendulum due to thermal effects the experimental part explained on chapter 5 and 6 has been used in this section.

7.1. Friction coefficient

The analysis of the shape of the loops of the test described in section 5.3 indicates four major effects related to the frictional performance of the devices that generates distortion of the Coulomb's rectangular loop:

- a “load effect”, consisting in the reduction of the friction coefficient due to increments of the applied load.
- a “cycling effect”, that appears as a continue reduction of the friction coefficient occurring with the cycling, greater for higher velocity tests (see Figure 97).
- a “velocity effect”, that manifests itself as a rounding of the shape of the loops, usually more evident for the high velocity tests. In these cases the isolator is reaching the maximum displacement, the sliding velocity is decreasing, and at the same time the coefficient of friction is decreasing too, suggesting that for higher velocity the friction is higher.
- a “breakaway” effect appearing as a sudden increase of coefficient of friction at the beginning or at each inversion of the motion. This effect encloses two phenomena, one at the start of sliding, the other at every motion reversal. The increased friction coefficient detected in the first phenomenon is generally properly referred as breakaway friction coefficient, also known as static friction coefficient, to distinguish it from the sliding (kinetic) friction coefficient. The second phenomenon, generally referred to as stick-slip (see section 3.1), corresponds to a short duration increase of the frictional force, followed by a rapid decrease. Both the phenomena can be related to a momentary sticking of the interfaces and to the acceleration impulse occurring at the start of the test and at every motion reversal. The breakaway effect is clearly visible in all the tests.

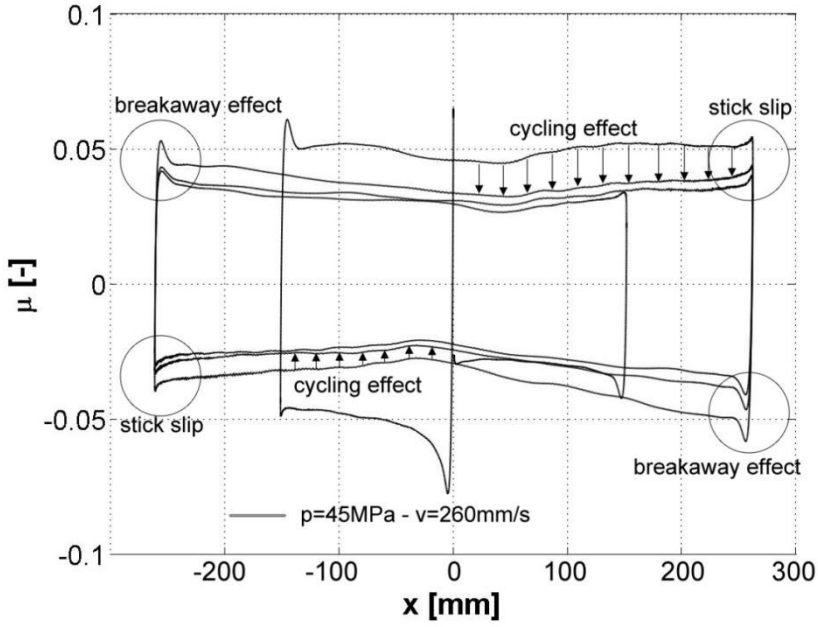

Figure 97: Experimental friction coefficient-displacement loop p=45MPa and v=260mm/s.

The 'Velocity' slightly influences these experimental tests. The sliding friction coefficient increases rapidly with velocity, up to a certain velocity value, beyond which it reaches steady state condition and it remains almost constant [11], [31], [48]. In literature this velocity threshold ranges between 150-200 mm/s. Since the experimental tests in this study are carried out with a chosen instant velocity between 182mm/s and 338mm/s, the 'velocity effect' does not influence the shape of the cycles when the instant velocity reaches maximum value. In fact the rounded shape that should occurs in the central part of force-displacement loop is not visible in Figure 97-Figure 100. Conversely the loops show a concave shape in

the central part and this effect could be related the irregular profile of flash temperature that has been detected in section 5.7 (see Figure 87-Figure 89).

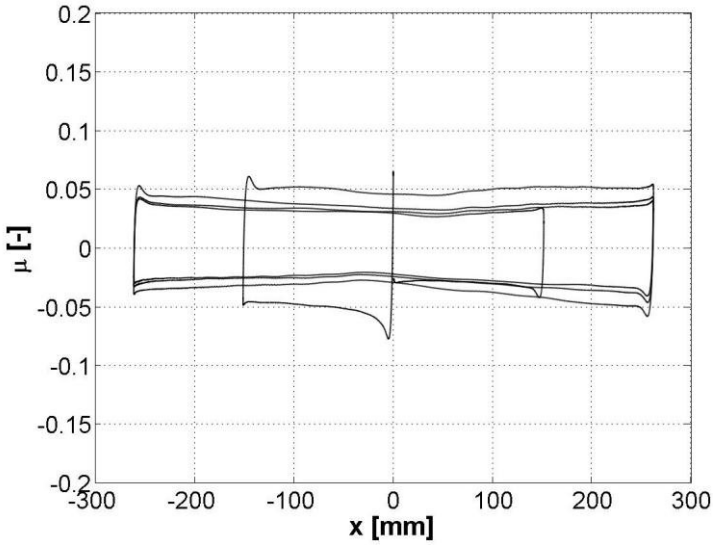

Figure 98: Experimental friction coefficient-displacement loop for p= 45MPa and v=260mm/s.

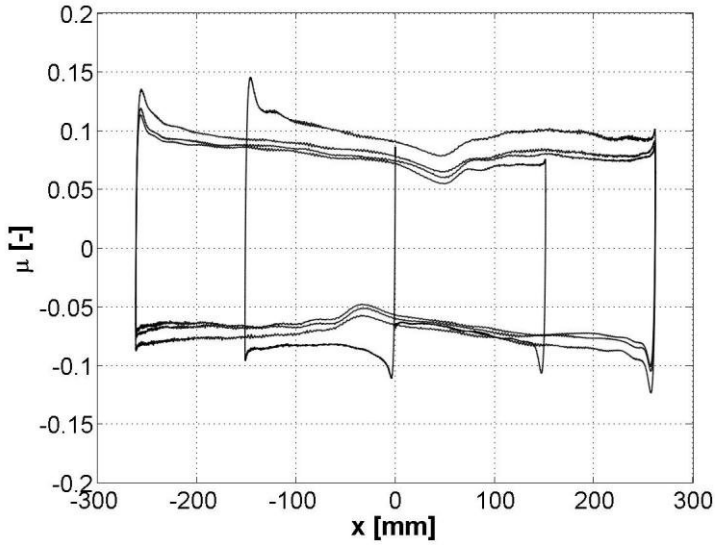

Figure 99: Experimental friction-displacement loop for p= 16MPa and v=260mm/s.

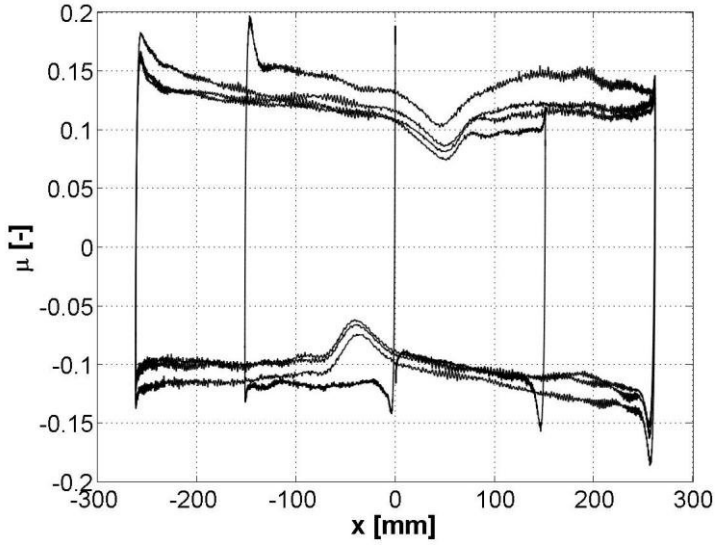

Figure 100: Experimental friction-displacement loop for p= 8MPa and v=260mm/s.

'Lo*ad effect'* and '*cycling effect'* are noticeable in these tests (Figure 97, Figure 98, Figure 99, and Figure 100). They directly affect the Energy Dissipated per Cycle (EDC), evaluated as the area underneath the force-displacement loop. Over the considered velocity range, the average values of EDC are EDC_{av}= 123.4, 94.8 and 69.7, kNm for the applied pressure of 8,16 and 45 MPa respectively. In Table 12 are collected the percent variation of EDC with respect to the average value EDC_{av}.

Table 12: Energy dissipated per cycle EDC with respect the average EDC_{av}.

		EDC reduction [%]		
Series	**V (mm/s)**	**p=8 Mpa**	**p=16 Mpa**	**p=45 Mpa**
1° Cycle	182	-2.2	-4.3	-5.1
	260	-4.1	-4.3	-1.6
	338	1.8	0.0	-3.4
2° Cycle	182	-8.3	-6.2	-9.0
	260	-15.1	-15.1	-22.0
	338	-12.0	-15.6	-20.6
3° Cycle	182	-11.7	-10.6	-14.6
	260	-18.3	-19.1	-28.3
	338	-13.8	-20.5	-26.5

The difference of the value reported in Table 12 confirm the dependence of the coefficient of friction on the applied load and a slight dependence on the velocity. The variation in percentage, between the actual value of EDC and the average value EDC_{av} is depicted versus the peak velocity and versus the cycles in Figure 103 and in Figure 104, respectively.

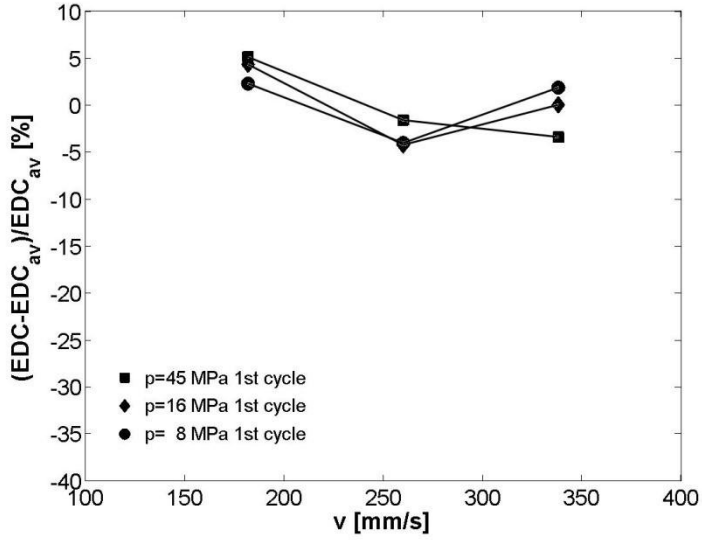

Figure 101: Percent variation of EDC versus velocity for 1st cycle.

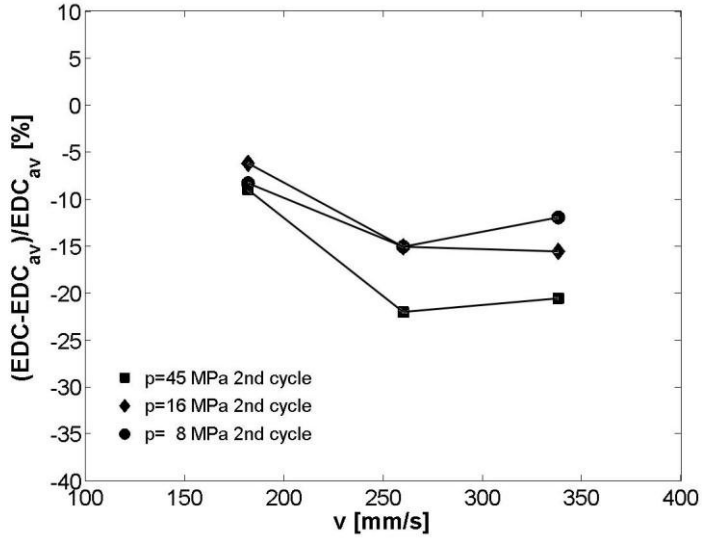

Figure 102: Percent variation of EDC versus velocity for 2nd cycle.

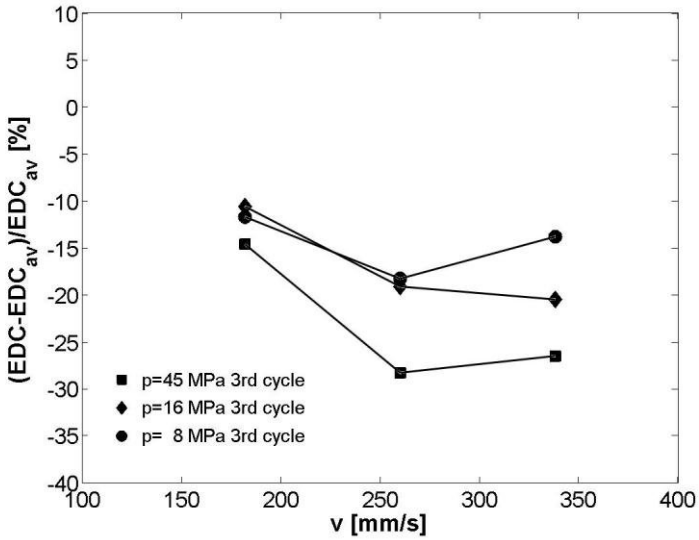

Figure 103: Percent variation of EDC with respect to the average value versus velocity for 3rd cycle.

The differences represented in Figure 101, Figure 102 and Figure 103 regard the variation of EDC with respect the velocity. Between the velocity of 182 mm/s and 260 mm/s there is a significantly decreasing of EDC then the relationship is almost constant. It is possible to confirm the existence of a critical velocity which ranges between 150 and 200 mm/s beyond which friction coefficient remains almost constant.

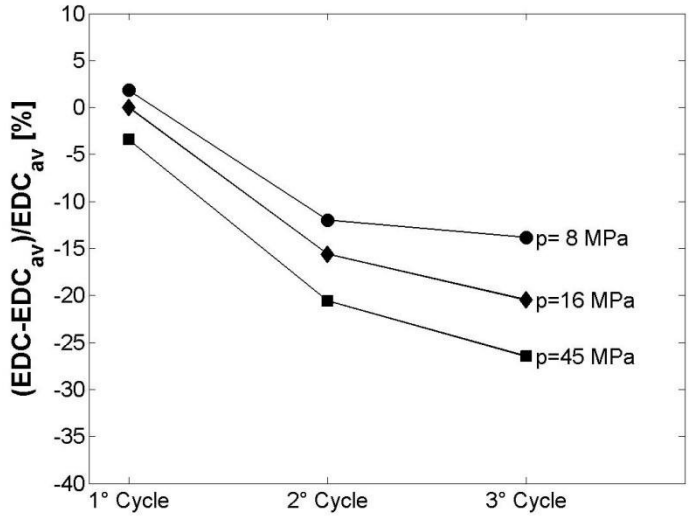

Figure 104: Percent variation of EDC with respect to the average value versus cycle and v=338 mm/s.

In Figure 104 is clear the dependency of the variation of EDC on both 'cycling *effect'* and '*load effect'*. The EDC range between low pressure and high pressure test increase cycle by cycle and for the third cycle is wider varying between -11.7 and -28.3%. The observed dispersion shows a relevant dependence of EDC by velocity and cycling. Since the dissipated energy is an important parameter for the control of acceleration, velocity and displacement imposed over the isolated structure, the load, velocity and cycling effect could significantly influence the predicted response of the whole structure.

7.2. Proposed model

The application of exponential models in the analysis of a sliding isolation system have been studied in the past (Constantinou et al.,1990 Mokha et al. 1993, Dolce et al.) with the purpose of evaluate the effects of sliding velocity, contact pressure, breakaway friction on the mechanical behavior of steel-PTFE sliding bearings. Indeed the phenomenological evaluation of these parameter have represented an important improvement for the evaluation of the friction coefficient. But it is still needed in the phenomenological model an implementation able to represent the reduction of the friction developed by sliding system along the travelled path, due to the increment of flash temperature.

In this study is proposed a model that allows the prediction of the friction degradation due to thermal effect, as well as the load and velocity effects. The model has this expression:

$$\mu(W, T_f, v) = f_w(W) \cdot f_T(T_f) \cdot f_v(v) \tag{7.1}$$

Where $f_w(W)$, $f_t(T_f)$ and $f_v(v)$ represent the dependency on the vertical applied load W (load effect), the flash temperature T_f (thermal effect) and instant velocity v (velocity effect) respectively. In the next parameters each function will be defined and calibrated according with experimental data. Then predicted and experimental results are finally compared.

7.3. Dependency of kinetic friction coefficient to applied normal pressure

In the existing literature, numerous studies deal with the effects of the applied load on the coefficient of friction. Many of the studies regard steel–PTFE interfaces [31], [44], [47], [55]. They show that the sliding friction coefficient reduces while increasing pressure with a rate of reduction practically constant and quite insensitive to sliding velocity. A similar trend was found for the steel-polymer interfaces of the isolators tested in this study. To assess the relationship between applied vertical load (pressure) and friction coefficient a proposed model is here evaluated. The load effect is expressed as function of the coefficient of friction coefficient μ_s, the applied vertical load W and a load reference value W_{ref}:

$$f_w(W) = \mu_s e^{-W/W_{ref}} \tag{7.2}$$

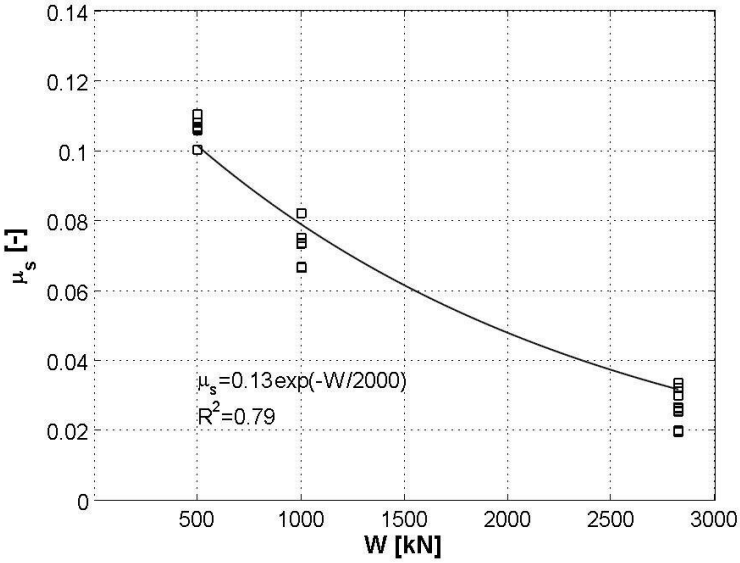

Figure 105: Variation of semi-static friction coefficient μ_{ss} with the applied load W**.**

Since the load effect is influences by the cross correlation between the aforementioned effects, the experimental data are opportunely processed in order to reduce the cross correlation between the variables. Therefore the influence of cycling effect is reduces only considering experimental data of the fist cycle. With regards to the velocity effect, the selected experimental data were picked in the portion of the loop with the highest instant velocity or rather the point x=0mm where slider pass through with the maximum pick velocity. Since the velocity effect is constant and it is not longer related when the velocity is more than 150-200mm/s [Bondonet 1997, Dolce et al. 2005], in this case in the selected point (x=0) data are all influenced by the velocity with a constant parameter f_v. the velocity effect will depurated in the next section of this study with a determined

correction parameter. Then in the evaluation of the prediction friction model proposed in eq(7.1), cross correlation between variables are reduced.

A determination factor of R^2 =0.79 was found by eq. (7.2) for the prediction of the experimental values. The values of μ_s =0.14 and W_{ref} =2000 kN are determined with a least squares regression over the experimental coefficients. These couple of values represent the best agreement between numerical and experimental results.

7.4. Dependency of kinetic friction coefficient to velocity

An increment of the coefficient of friction with the increasing sliding velocity, in the operational range of these devices, was documented by many authors (Mokha et al. 1990, Constantinou et al. 1990, Bondonee et al. 2002, Dolce et al. 2005). The experimental data considered in these studies are conducted at medium levels of sliding pick velocity. Apparently, coefficients of friction deducted by the experimental tests performed in this work are in disagreement with the exponential law existing in literature. The friction-displacement loop represented in Figure 97 shows a decreasing of friction coefficient in correspondence of higher velocity. This disagreement is due mainly by the coexistence of both velocity and cycling effect.

As mentioned above the increment of temperature at the contact surfaces between the slider and the steel concave plate due to repetition of cycles increases with velocity and the applied load. The device performance observed during high velocity and high pressure tests appears to be significantly affected by both the

velocity and the cycling effect with the latter influencing the device response in an opposite way with respect to velocity (reduction of friction coefficient).

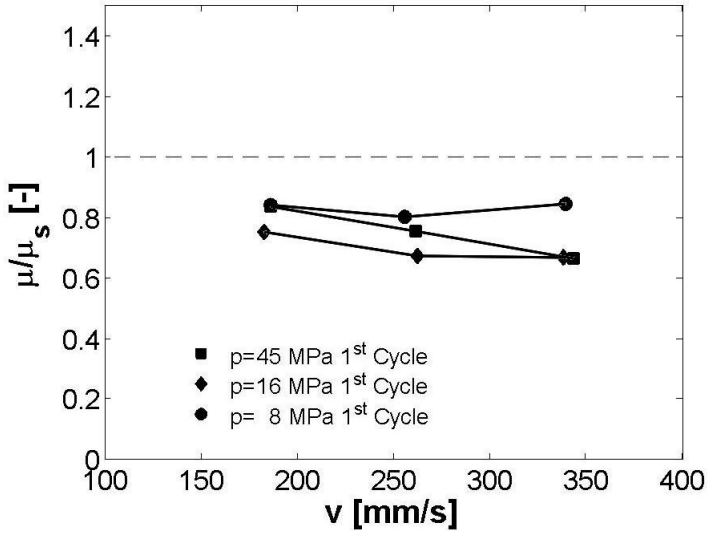

Figure 106: Ratio between friction coefficient after and before the first cycle vs instant velocity.

In Figure 106 is represented between friction coefficient after and before the first cycle vs instant velocity. This parameter is 0.85 for low pressure of 8 MPa and it is not related with the pick velocity of the test. Whereas the average ratio μ/μ_s is 0.80 and 0.75 for medium and high pressure test respectively.

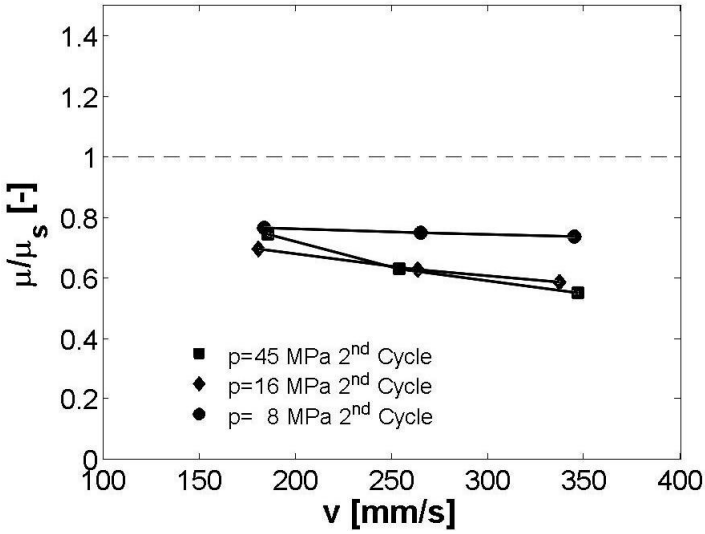

Figure 107: Ratio between friction coefficient μ/μ_s referred to the second cycle vs instant velocity.

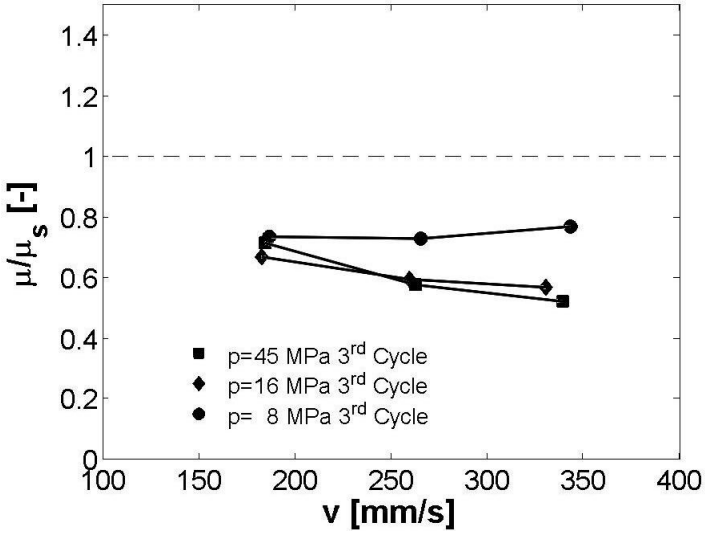

Figure 108: Ratio between friction coefficient μ/μ_s referred to the third cycle vs instant velocity.

In Figure 107 and in Figure 108 is shown the ratio μ/μ_s referred to the second and third coefficient respectively. This experimental data indicates a reduction of the coefficient of friction at the higher velocities, especially during the 2nd and 3rd cycle of the test for which cycling effects are particularly important. In fact friction coefficient is significantly affected by cycling effect which results more marked for higher velocity test.

Since for these tests there is a coexistence of both velocity and cycling effects, for the study of a relationship between kinetic coefficient of friction and the pick velocity it should be necessary a series of test witch range between low pick velocity and high velocity. With a full range of velocity it should be possible evaluate the influence of friction coefficient with the velocity.

The range of the experimental test reported in these study is not sufficient to evaluate the velocity effect parameter. Even though should have been possible to pick points of the loop in correspondence of the maximum displacement of the slider when the velocity of the slider decrease and the velocity effect is zero, the slider experimented a stick slip phenomenon that distorted the friction coefficient (Figure 97, Figure 100). Therefore, to overcome this issue, for the evaluation of a final model which includes all the parameter it is used the exponential law provided by Lomiento et Al. (2012):

$$f_v(v) = \gamma + (1-\gamma)e^{-|v|/v_{ref}} \tag{7.3}$$

where v is the sliding velocity, $v_{ref} = 10$ mm/s is a reference velocity, and $\gamma = 1.4$ represents the ratio between the fast-motion and the slow-motion coefficient of friction.

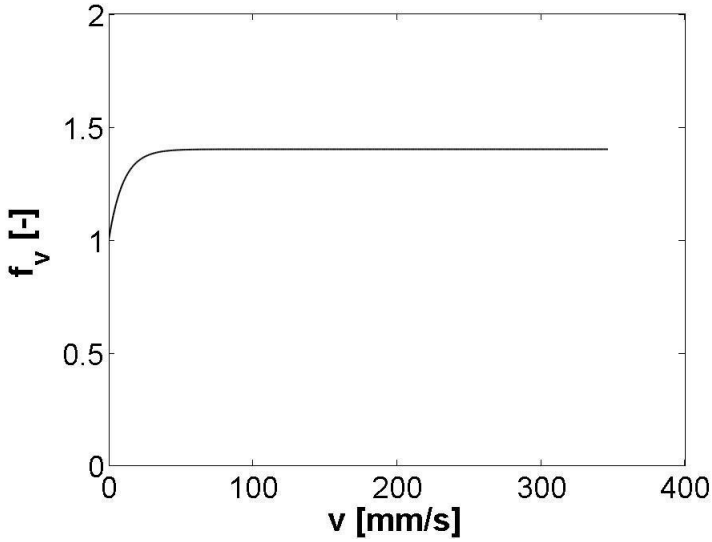

Figure 109: Predicted variation of the friction coefficient of friction with the velocity.

As shown in Figure 109, for the pick velocity range used in the tests the exponential velocity equation is constant it assumes the maximum value.

During the application of the sinusoidal input, the instant velocity decrease only when the slider reaches the maximum displacement (200÷260mm). Therefore the application of eq. (7.3) in this model slightly influence the friction displacement loop and it rounds only the corner of the predicted force-displacement loop. Over the fast-motion condition the value of f_v is equal or quite close to 1.4. When the motion is slow, the coefficient of friction f_v is equal to 1 and the rounding of the shape of the experimental loops is not evident because occurred a stick slip for low instant velocity. The coexistence of these effects affects the typical rounded shape of the loop at peak displacement (x=260mm).

7.5. Calibration of friction-temperature relationship

The repetition of reversal motion affects the coefficient of friction. The progressive reduction of the coefficient of friction it is called cycling effect. The decreasing of kinetic friction coefficient was for the first time noticed by Mokha et al (1990) for PTFE-steel sliding contact surfaces.

The friction degradation could be attributed to a decrease in hardness of the thin surface layer due to the frictional heating [62]. For a moving heat source, frictional heating causes also an abrupt gradient in the temperature distribution in the depth direction of the sliding surfaces (Jaeger, 1943). A reduction of the hardness in the vicinity of the surface based on the temperature distribution is reported by Nakahara (2005). The hardness sharp reduction near the sliding surface is considered to activate a thin soft layer on the surface that performs as a solid lubricant. The theoretical analysis of the temperature rise at contacting surfaces is generally based on the work of Blok (1963), Jaeger (1959) and Carlsaw et al. (1959), and the relationships obtained by these authors have been discussed and applied to the problem of the temperature rise due to friction by Archard (1959) and Rabinowicz (1964). Constantinou et al. (1999) have applied these theories to PTFE sliding isolators in order to detect the temperature rise at the sliding interface, achieving a good agreement between experimental and predicted values. In all these studies, the temperature rise is related to the heat flux generated by the frictional forces, equal to the power dissipated per unit area.

In this section a friction degradation is defined as:

$$f_T(T) = e^{-(T/T_{ref})^{\alpha}} \tag{7.4}$$

Where T_{ref} is a reference value of the parameter T and α represents the friction degradation rate.

The values of T_{ref} and α are obtained by least square regression of the experimental results. Since the direct use of the data reflects the load and velocity effects, a partial derivative of the friction model with respect of T was used in order to isolate the cycling effect and an additional function was defined as:

$$Z(T) = \frac{\partial \mu(W,T,v)}{\partial T} \cdot \frac{1}{\mu(W,T,v)} = \frac{\partial f_T(T)}{\partial T} \cdot \frac{1}{f_T(T)} \tag{7.5}$$

Eq. (7.5) depends only by thermal variable T. By substituting equation (7.1) in (7.5) and it is obtained:

$$Z(T) = -\alpha \frac{T^{\alpha-1}}{T_{ref}{}^{\alpha}} \tag{7.6}$$

Experimental values of $Z(\bar{T})$ at the experimental value of $\bar{T}$ were evaluated for each test of series 200-300-400 by the analytical model shown in chapter 6.

$$Z(\bar{T}) = \frac{\delta_T [\mu](\bar{T})}{\delta T} \cdot \frac{1}{E_T [\mu](\bar{T})} \tag{7.7}$$

Where δ_T, E_T are respectively the central difference operator and the central mean operator related to fixed position in the sinusoidal input picked cycles by cycles. δT represents the difference of temperature evaluated for selected position on the sliding surface and cycle by cycle. Equation (7.7) became:

$$Z\left(\bar{T}\right)=\frac{\mu_{i\_\bar{x}(j)}-\mu_{(i+1)\_\bar{x}(j)}}{T_{i\_\bar{x}(j)}-T_{(i+1)\_\bar{x}(j)}}\cdot\frac{2}{\mu_{i\_\bar{x}(j)}+\mu_{(i+1)\_\bar{x}(j)}} \tag{7.8}$$

Where $\bar{x}$(j) with j=1…n. represents the position selected in the loop and n the number of points; i=1:3, represents the cycle where the experimental data is picked. The values α and T_{ref} are determined with a least squares regression on the experimental data $Z(\bar{T})$. The values of α =0.8 and T_{ref} = 90 °C are determined.

The degradation function f_T is reported in Figure 110 versus T_f. This function represents the kinetic friction degradation under sliding motion in a high strength polymer-stainless steel contact surface. In Table 13 are reported the maximum flash temperatures evaluated with the analytical method (see Table 10) and as well the correspondent percent reduction of the coefficient of friction, evaluated as $f_T(T)-1$. An average value of friction reduction due to the cycling effect is 50%. The maximum friction coefficient reduction of 69% is obtained for the test 406 (p=45 MPa, v=338 mm/s) when the value of flash temperature evaluated in the central point of sliding surface in the third and last cycle is 92.4°C.

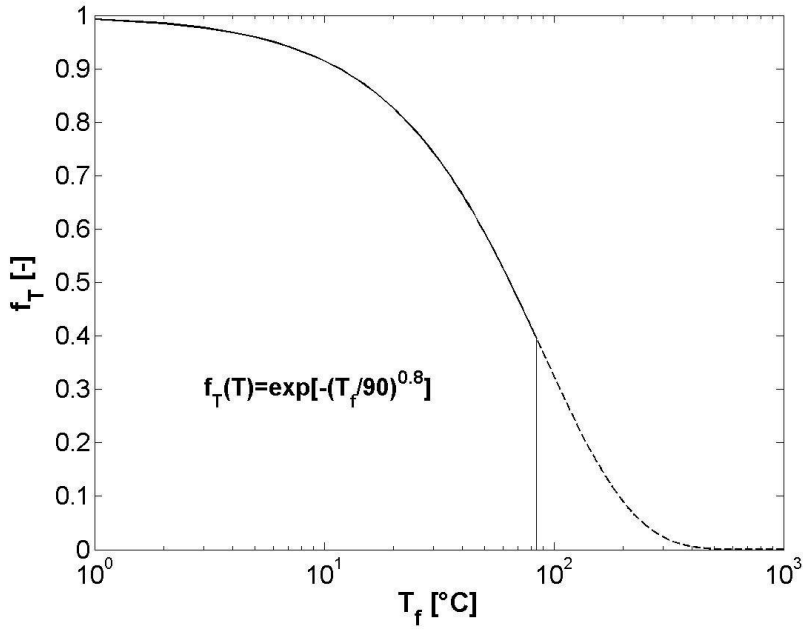

Figure 110: Reduction of the coefficient of friction predicted by function f_T.

The continuous line and Figure 110 represents the degradation of friction coefficient for the temperature obtained during the test. While the dashed line which tends to zero represents the theoretical behavior of the function f_T for $T_f \rightarrow \infty$. The function has a upper limits represented by the glass transition temperature of the polymer (T_g). Considering the experimental flash temperature evaluated with the thermographic camera (Table 9) and the reduction of the coefficient of friction predicted by function f_T, the overall decay of friction during the test is between 40-60% in the central part of the slider and 25-40% in the border.

Table 13: Maximum Flash Temperature of the variable T_f reported in Table 10 and relative friction reduction in each test.

		T_{f_slider} [°C]			friction reduction fc-1 (%)		
Series	V (mm/s)	p=8 Mpa	p=16 Mpa	p=45 Mpa	p=8 Mpa	p=16 Mpa	p=45 Mpa
200	182	31,5	45,4	64,4	-31	-39	-48
	260	33,2	51,4	68,2	-32	-42	-49
	338	37,5	55,1	76,8	-35	-44	-52
300	182	44,5	63,0	80,4	-30	-42	-52
	260	50,8	67,8	84,7	-34	-44	-54
	338	61,1	77,0	91,4	-40	-50	-57
400	182	48,1	65,2	80,6	-49	-58	-64
	260	53,8	68,5	82,4	-52	-60	-65
	338	57,4	75,1	92,4	-54	-62	-69

The correlation between f_v values predicted by using eq. (7.3) and experimental values, corrected to eliminate the temperature effect, is shown in Figure 111.

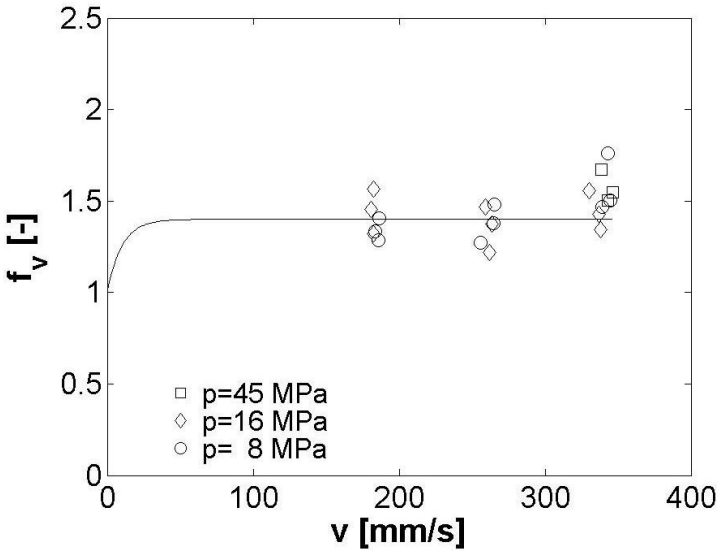

Figure 111: Variation of the coefficient of friction with the velocity v [44] and experimental values adjusted with the parameter $f_{Tf.}$

7.6. Final Model

All the model variables defined are in this section combined. By substituting eq. (7.2), eq. (7.3) and eq. (7.4) in eq (7.1) the proposed model is expressed as:

(7.9)

$$\mu(W, T_f, v) = f_w(W) \cdot f_T(T_f) \cdot f_v(v) = \mu_s e^{-W/W_{ref}} \cdot e^{-(T/T_{ref})^{\alpha}} \cdot \left[\gamma + (1-\gamma) e^{-|v|/v_{ref}}\right]$$

Eq. (7.9) is applied for the protocol test reported in chapter 5. For each test are selected three characteristic positions of the friction-displacement loop and for each cycle the couple $\left[\bar{x}_j, \mu(\bar{x}_j)_i\right]$ is represented in Figure 112.

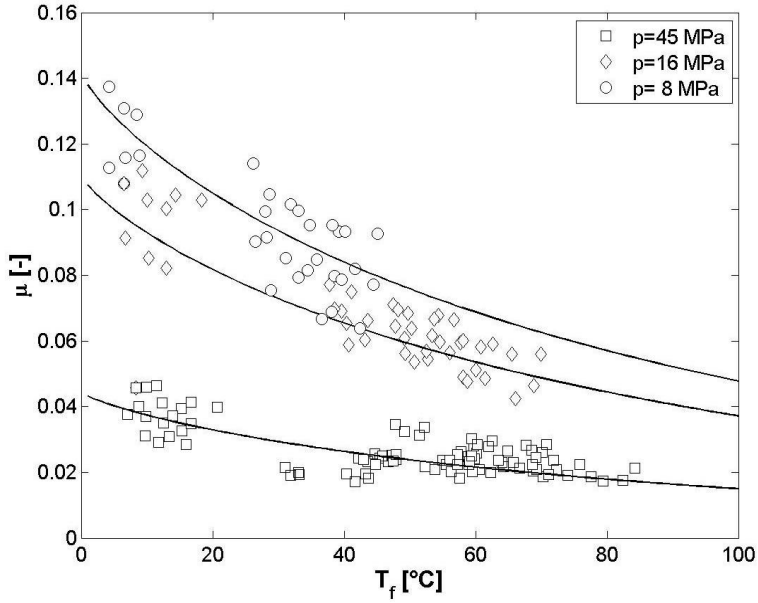

Figure 112: Experimental friction coefficient versus flash temperature compared with prediction model values (continuous line).

Figure 112 shows the comparison between the prediction model, represented with continuous line, and the experimental data with a average error of the predicted friction coefficient of 9.5%.

The experimental friction-displacement loops are compared in Figure 113, Figure 114 and Figure 115 with coefficient of friction predicted by eq. (7.9). The comparison between analytical and experimental loop are in good agreement.

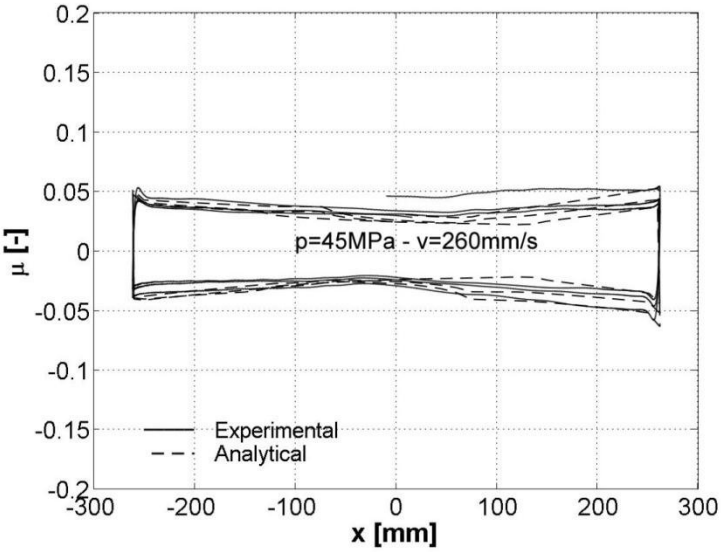

Figure 113: Comparison between Experimental and predicted (load + velocity + cycling effects) friction coefficient displacement loop for p= 45MPa and v=260mm/s.

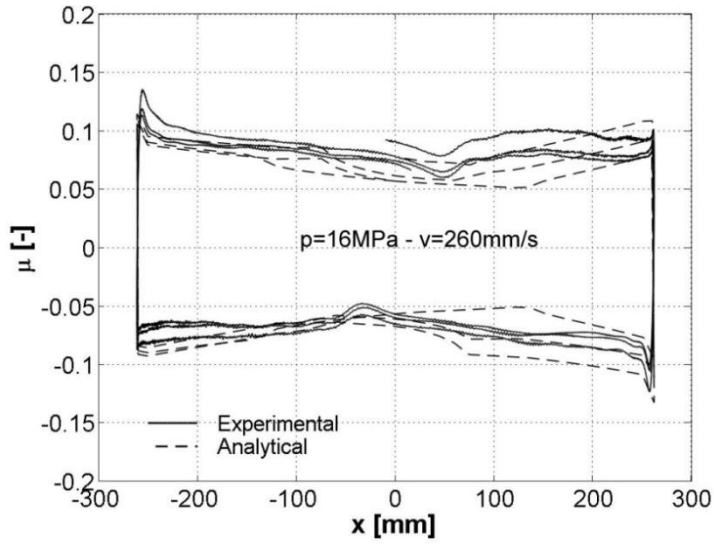

Figure 114: Comparison between Experimental and predicted (load + velocity + cycling effects) friction coefficient displacement loop for p= 16MPa and v=260mm/s.

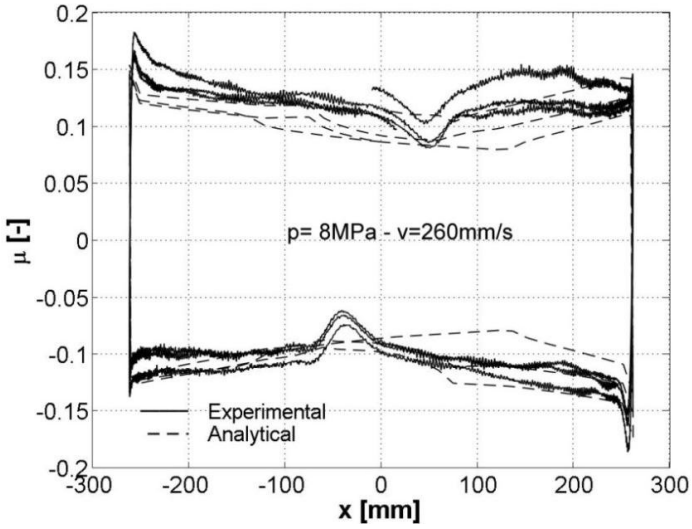

Figure 115: Comparison between Experimental and predicted (load + velocity + cycling effects) friction coefficient displacement loop for p= 8MPa and v=260mm/s.

It is possible to give an estimation of the agreement between the proposed model and the experimental data in term of EDC. In Table 14 the experimental EDCs, as well as the analytical EDCs evaluated with the proposed prediction model without the contribution of thermal effect, are collected. Instead In Table 15 the analytical EDCs evaluated with the contribution of the degradation coefficient $f_T(T)$ are reported. Different shades of gray are used for highlight the errors greater than 10%, 20% and so on.

Table 14: Experimental values of EDC ad percentage errors of the proposed model without the cycling effect.

		Experimental EDC			Analytical EDC Load+velocity					
P	V	1st Cycle	2nd cycle	3rd cycle	1st Cycle		2nd cycle		3rd cycle	
(Mpa)	(mm/s)	(kNm)	(kNm)	(kNm)	(kNm)	(%)	(kNm)	(%)	(kNm)	(%)
8	182	71,2	63,8	61,5	85,2	19,7	85,2	33,5	85,2	38,5
	260	66,8	59,2	56,9	90,8	35,9	90,8	53,4	90,8	59,6
	338	70,9	61,3	60,1	90,7	27,9	90,7	48,0	90,7	50,9
16	182	98,8	88,8	84,7	141,5	43,2	141,5	59,3	141,5	67,1
	260	90,7	80,4	76,6	132,7	46,3	132,7	65,0	132,7	73,2
	338	94,7	79,9	75,3	141,5	49,4	141,5	77,1	141,5	87,9
45	182	129,6	112,2	105,3	160,4	23,8	160,4	43,0	160,4	52,3
	260	121,3	96,2	88,5	150,6	24,2	150,6	56,5	150,6	70,2
	338	119,1	97,9	90,7	160,6	34,8	160,6	64,0	160,6	77,1

Table 15: Experimental values of EDC ad percentage errors of the proposed model including the cycling effect.

		Experimental EDC			Analytical EDC Load+velocity+cycling effects					
P	V	1st Cycle	2nd cycle	3rd cycle	1st Cycle		2nd cycle		3rd cycle	
(Mpa)	(mm/s)	(kNm)	(kNm)	(kNm)	(kNm)	(%)	(kNm)	(%)	(kNm)	(%)
8	182	71,2	63,8	61,5	70,8	-0,6	64,3	0,8	54,0	-12,2
	260	66,8	59,2	56,9	65,1	-2,5	59,0	-0,3	53,0	-6,9
	338	70,9	61,3	60,1	65,7	-7,3	58,7	-4,2	53,3	-11,3
16	182	98,8	88,8	84,7	101,7	2,9	89,9	1,2	81,5	-3,8
	260	90,7	80,4	76,6	93,8	3,4	82,0	2,0	74,1	-3,3
	338	94,7	79,9	75,3	93,5	-1,3	81,6	2,1	73,1	-2,9
45	182	129,6	112,2	105,3	107,7	-16,9	92,6	-17,5	82,8	-21,4
	260	121,3	96,2	88,5	95,2	-21,5	83,2	-13,5	75,6	-14,6
	338	119,1	97,9	90,7	98,0	-17,7	83,2	-15,0	72,3	-20,3

As explained before there is not significant differences in EDC for different pick velocity. The deviancy of analytical EDC with respect to the average EDC_{av} is quite low. The EDC predicted with the analytical model without the contribution of the degradation variable $f_T(T)$ is not accurate. For high pressure and higher velocity tests the errors in the prediction are 34.8%, 64% and 77,1% in overestimation of the EDC for 1st, 2nd and 3rd cycle, respectively. As expected the accuracy of the prediction model is lower for the 2nd and 3rd cycle where the temperature of the contact surface increase and the cycling effect is more significant. With respect to the model reported in eq (7.9) the prediction is more reliable and the errors are -17.7%, -15.0% and -20.3% for 1st, 2nd and 3rd cycle. The results show how the use of the prediction model without the use of the thermal effect produces not tolerant errors in the prediction of EDC, above all when the vertical applied load produce high contact pressure.

Chapter 8

8. Conclusions

In this study, it was decided to investigate the degradation of seismic performance of friction pendulum devices due to thermal effects. It must be noted that these specific anti-seismic devices represent the latest technology for seismic protection of buildings and bridges and are presently utilized in many project worldwide. In these supports the dissipation of seismic motion occurs exclusively by the friction produced during sliding of the surfaces while the seismic isolation is obtained by the shifting of the natural period of the superstructure. Several studies have shown that the friction coefficient in a contact problem between polymer (PTFE) and stainless steel deviates from the Coulomb's friction law. Furthermore, most recent studies have shown that the coefficient of friction is also in a close relationship with the increase of temperature due to the thermal effect.

The complete characterization of these device performance is however still incomplete even though recent experimental activity largely improved their acceptance and qualification. The effect of the temperature rise during seismic motion is of paramount importance and barely researched on full scale devices. It affects, in fact, the frictional characteristics of the low friction material of the device, with serious implications on the overall dissipation capacity of the isolator.

The research is focused on the acquisition, during laboratory tests, of the temperature pattern developed at the interface between sliding components. For

this goal it was used an high quality infrared imaging camera. It was necessary the design an ad hoc software for data interpretation and image correction due to the critical laboratory environment during the tests.

The acquired thermal information needed to be calibrated and further correlated with numerical models of performance degradation due to friction coefficient variations.

Therefore through an experimental campaign carried out with single pendulum bearings it has been investigated the dependence of the friction coefficient with the temperature rise in order to propose a phenomenological model able to assess the real performance of the friction pendulum.

A series of friction Pendulum have been tested at Caltrans SRMD Testing Facility of San Diego University of California which is equipped with a shaking table test specifically designed for full-scale tests. During the tests, the table was equipped with a thermographic camera specially calibrated for the type of material tested (polished stainless steel).

Based on the available experimental outcomes it was possible to point out some important results valid for the increase of flash temperature in high strength-stainless steel contacts surface according with the velocity and pressure range used in the experimental campaign described in this work.

The experimental flash temperature evaluated with the thermographic camera depends on pressure and velocity and significantly increase for higher velocity and higher pressure. Cumulative short motion tests cause an accumulation of heat on the slider and on the sliding surface and, as a consequence, the parameter T_f is subjected by a 'cycling effect'. The increment of temperature is not constant along the sliding surface and is more pronounced in the central part of the slider rather

than in the border of the sliding surface. This is basically due to the variation of instant velocity in the contact surface.

The evaluation of the temperature rise at the sliding interface was also carried out with Carslaw and Jaeger's Theory. The calibration of this analytical approach is based on the experimental temperature procedure deal with the thermographic camera.

In a second step an analytical comparison between the experimental friction coefficient and the temperature rise have been carried out and a prediction model of degradation of the friction coefficient was proposed.

The model introduced in this study presents three independent functions that take into account all together the effects of applied load f_w, sliding velocity f_v and thermal effect f_T on the coefficient of friction of sliding bearing. So it takes into account both mechanical variables such as velocity and apparent pressure, and also the degradation of dissipative characteristics of a friction pendulum due to thermal effects.

The comparison between experimental data with values predicted by the friction model was carried out in terms of EDC per cycle and coefficient of friction with and without the application of the degradation variable f_T. A 'Load *effect'* and '*cycling effect'* have been detected and they directly affect the EDC, evaluated as the area which is underneath the force-displacement loop. Based on experimental outcomes, it is clear the dependency of the variation of EDC on both '*cycling effect'* and '*load effect'*. Since the dissipated energy is an important parameter for the control of acceleration, velocity and displacement imposed over the isolated structure, the load, velocity and cycling effect significantly influence the predicted response of the whole structure.

The results show how the use of the prediction model without the use of the thermal effect produces not tolerant deviation in the prediction of EDC above all when the vertical applied load produce high contact pressure.

It could be useful to calibrate a relationship between cycling effect and pressure on the contact surface valid for high strength polymer liner and then provide a maximum allowable contact pressure to control the decay of friction coefficient. The comparison has shown the paramount importance of the thermal effect in term of dissipative characteristics of the sliding isolators especially for high contact pressure.

Reference

[1] AASHTO (1991), "Guide Specifications for seismic Isolation Design", included in Standard Specifications for Seismic Design of Highway Bridges,American Association of State Highwa and Transportation Officials, Washington.

[2] Amin N. and Mokha A. (1995). "US Court of Appeals Building: Seismic Isolation Implementation", Proc. Joint ASME/JSME Pressure Vessels and Piping Conference, Seismic Shock and Vibration Isolation, Honolulu, HI.

[3] Anderson T.L. (1989). "Seismic Isolation for the Losangeles Country Fire Command and Control Facility", Proc. ASCE Structures Congress, Vol. 1, San Francisco, CA.

[4] Archard, J. F. The temperature of rubbing surfaces, Wear, 2 (1959) 438 - 455.

[5] ATC – Applied Technology Council, (1996). ATC-40: Seismic Evaluation and Retrofit of Concrete Buildings, Report N°. SSC 96-01, Redwood City, California (USA).

[6] Benzoni G., and Seible, F. (1998). Design of The Caltrans Seismic Response Modification Device (SRMD) Test.Facility". USA – ITALY Workshop on Protective Systems. Report No. MCEER-98-0015, Multidisciplinary Center for Earthquake Engineering Research, Buffalo, New York City.

[7] Benzoni G., Casarotti, C., (2009), "Effect of Vertical Load, Strain Rate and Cycling on the response of Lead Rubber Seismic Isolatios". Journal of Earthquake Engineering.

[8] Benzoni G., Bonessio, N., Lomiento, G., (2011), "Experimental Performance and Modeling of Sliding Anti-Seismic Devices", 7th World Conference on Joints, Bearings and Seismic Systems for Concrete Structures, Las Vegas, Nevada, October 2-6.

[9] Blok H., "Fundamental mechanical aspects in boundary lubrication", SAE Trans., 46 (1940) 54 - 68.

[10] Blok H., "The Flash Temperature Concept", Wear, Vol 6, 1963, p 483-494.

[11] Bondonet G., and Filiatrault, A. (1997). "Frictional Response of PTFE Sliding bearings at Higher Frequencies". Journal of Bridge Engineering. 2:4, 139-148.

[12] Bowden, F.P. and Tabor, D. (1950), "The Friction and Lubrication of Solids: Part I", Oxford University Press, Oxford, UK.

[13] Bowden, F.P. and Tabor, D. (1964), "The Friction and Lubrication of Solids: Part II", Oxford University Press, Oxford, UK.

[14] Bowden, F.P. and Tabor, D. (1973), "Friction: an introduction to Tribology", Heinemann, UK.

[15] Buckle I.G. and Mayers R.L., (1990). Seismic Isolation: Hystory, Appplicatin and Performance- A world View, Earthquake Spectra, Vol. 6, No. 2.

[16] Braga F., Dolce M.,Ferrigno A., Laterza M.,Marotta G., Masi A, Nigro D and Ponzo F., (1997). "Indagine sperimentale per la valutazione delle caratteristiche meccaniche di isolatori elastomerici armati ad elevato smorzamento, *VII Congresso Nazionale L'ingegneria Sismica in Italia,* Taormina.

[17] Carslaw H.S. and Jaeger C. (1959), “Conduction of Heat in Solids”, 2nd Edition, Oxford University Press, London, UK.

[18] Campbell T.I. and Kong, W. L. (1987),"TFE Sliding Surfaces in Bridge Bearings, Report ME-87-06”, Ministry of Transportation and Communications, Ontario, Canada.

[19] Campbell T. I., Pucchio, J. B., Roeder, C. W. and Stanton, 1. F. (1991), "Frictional Characteristics of PTFE Used in Slide Surfaces of Bridge Bearings", Proc. 3rd World Congress on Joint Sealing and Bearing Systems for Concrete Structures, Toronto, Ontario, Canada, Vol. 2 of Pre prints (published by the National Center for Earthquake Engineering Research, Buffalo, NY), 847-870.

[20] Charleston A.W.,Wright P.D. and Skinner R.I., (1987). “Wellington Cnetral Police Station, Base isolation of an Essential Facility, Proc. Pacific Conf. on Earthquake Engineering, Vol. 2, Wairekei, New Zealand.

[21] Chopra A. K. (2007). “Dynamics of Structures, Theory and applications to Earthquake Engineering”.

[22] Chang K. C.,J.S. Hwang and Lee G.C (1990). “Analytical model for sliding behavior of Teflon-stainless steel interfaces”. Journal Engineering Mechanics. ASCE,116, 2749-2763.

[23] Charleston A.W., Wright P.D. ans Skinner R.I., (1987). Wellington Central Police Station, Base Isolation of an Essential Facility, Proc. Pacific Conf. on Earthquake Engineering, Vol. 2, Wairekei, New Zealand.

[24] Constantinou M. C., Mokha A., and Reinhorn, A. (1990). “Teflon Bearings in Base Isolation, Part II: Modeling”. Journal of Structural Engineering. 116:2 455-474.

[25] Constantinou M. C., Tsopelas, P., Kasalanati A. and Wolff, E. (1999). “Property Modification Factors for Seismic Isolation Bearings”. Technical

Report MCEER-99-0012, Multidisciplinary Center for Earthquake Engineering Research, Buffalo, NY.

[26] Costantinou M.C., Cassese J. And Harris H.G., (1987). "Friction characteristics of Teflon-steel interfaces under dynamic conditions", Earthquake Engineering and Structural Dynamics, 15 (6), 751-759.

[27] Clough R.W. and Penzien J. (1975), "Dynamics of Structures", McGraw-Hill, USA.

[28] Deb, S. K. and Paul, D. K. (2000). "Seismic response of buildings isolated by sliding-elastomer bearings subjected to bi-directional motion". 12th World Conference on Earthquake Engineering, Auckland, New Zealand.

[29] Dolce M., Cardone D. and Ponzo F., (2001a). "Comparison od Different Passive Control System for R/C Frames through Shaking Table Test, Proc. 5th World Congress on Joints, Bearings and Seismic System for Concrete Structures, Rome, Italy.

[30] Dolce M., Cardone D., Nigro D., Croatto F., (2003). "The effect of friction variability on the response of isolated bridges". 8th world Seminar on Seismic Isolation, Energy Dissipation And Active Vibration Control of Structures Yerevan, Armenia, October 6-10.

[31] Dolce, M., Cardone, D., and Croatto, F. (2005). "Frictional Behavior of Steel-PTFE Interfaces for Seismic Isolation". Bulletin of Earthquake Engineering. 3:1,75–99.

[32] Dolce M., Ponzo F.C., Goretti A., Moroni C., Giordano F., De Canio G., Marnetto R. (2008). "3D Dynamic Tests on 2/3 scale masonry Buildings retrofitted with different System". Proc. 14th World Conference on Earthquake Engineering, Beijing, China.

[33] Dolce M., Ponzo F.C., Di Cesare A., Arleo G. (2010). "Progetto di Edifici con Isolamento Sismico". IUSS Press.

[34] Duerig T.W., Melton K.N., Stoeckel D. and Wayman C.M., (1990). "Engineering aspect of shape memory alloys", Butterworth-Heinemann Ltd, London.

[35] Fenz, D.M. Constantinou, M.C. (2006). "Behavior of the double concave Friction Pendulum bearing", Earthquake Engineering & Structural Dynamics, 35, 1403-1424.

[36] Jaeger, J. C. (1943). "Moving sources of heat and the temperature at sliding contacts". Proc. R. Soc. New South Wales, 76, 203–224.

[37] Kelly J.M., (1988). "Base isolation in Japan", Report No. UCB/EERC-88/20, Earthquake Engineering Research Center, University of California, Berkeley, Ca.

[38] Kelly, J.M. (1990). "Base isolation: linear theory and design". J. Earthquake Spectra, 6, 223-244.

[39] Kelly, J.M. (1986). "Aseismic base isolation: review and bibliography" Soil Dyna. Earthquake Eng., 5,202-216.

[40] Kelly, J.M. (2004). "Seismic isolation, Earthquake Engineering, form Engineering Seismology to Performance - Based Engineering", pp.11.1-11.32.

[41] Kelly J.M., and Quiroz E., (1992). "Mechanical Characteristic of Neoprene Isolation Bearings", Report N. UCB/EERC-92/11, Earthquake Engineering Research Center, Berkeley, CA.

[42] Hwang J.S., Chang K.C. and Lee G.C. (1990). "Quasi static and dynamic sliding characteristics of Tefon-stainless steel interfaces". Journal Engineering Mechanics. ASCE,117, 2747-2762.

[43] Housner G.W., (1998). Structural control: past, present and future, Journal of Engineering Mechanish- ASCE, 123 (9), 897-971.

[44] Lomiento, G., Bonessio, N. and Benzoni, G. (2012). “Friction model for sliding bearings under short duration motion”. Submitted to Journal of Earthquake Engineering.

[45] Micheli I., Cardini S., Colaiuda A., Turroni P. (2004). “Investigation upon the dynamic structural response of a nuclear plant on aseismic isolating devices”, Nuclear Engineering and Design, vol. 228, Issues 1-3, 319-343.

[46] Ministry of Infrastructure, “Ministerial Decree of 14 January 2008. Nuove Norme Tecniche per le Costruzioni”. Official Gazette No. 29 of 4 February 2008. Ordinary Supplement No. 30).

[47] Mokha. A. S. , Constantinou, M. C. and Reinhom, A. M. (1990a), "Experimental Study and Analytical Prediction of Earthquake Response of a Sliding Isolation System with a Spherical Surface", Report NCEER-90-0020, National Center for Earthquake Engineering Research, Buffalo, NY.

[48] Mokha. A., Constantinou, M. and Reinhom, A. (1990b), "Teflon Bearings in Base Isolation. I: Testing". Structural Eng.., ASCE, Vol. 116, No.2, 438-454.

[49] Mokha, A., Constantinou, M. C., Reinhorn, A. M. and Zayas, V. (1991). “Experimental study of friction pendulum isolation system”. Journal of Structural Engineering. 117:4, 1201-1217.

[50] Mokha, A., Constantinou, M. C., and Reinhorn, A. M. (1993). “Verification of friction model of teflon bearings under triaxial load”. Journal of Structural Engineering. 119:1, 240–261.

[51] Mosqueda, G., Whittaker, A.S., and Fenves, G.L. (2004). “Characterization and Modeling of Friction Pendulum Bearings Subjected to Multiple Components of Excitation.” Journal of Structural Engineering,130:3 423-432.

[52] Naeim, F., and Kelly, J.M.(1999), “Design of Seismic Isolated Structures: From Theory to Practice”, Wiley, Chichester, U.K.

[53] Nakahara T., (2005) “A model of seizure based on Burwell and Strang’s concept of wear mode transition”. In proceedings of the 31st Leeds Lyon Symposiumon Life cycle tribology, pp. 547–553 (Elsevier, Amsterdam).

[54] Paynter, F. R. (1973), "Investigation of Friction in PTFE Bridge Bearings", The Civil Engineer in South Africa, August, 209-217.

[55] Pedicone D. (2013). “Experimental Assessment of the Mechanical Behavior of Friction Pendulum Devices”. Phd thesis, Università degli Studi dell'Aquila

[56] Pranesh M., and Sinha R., (2000) “VFPI: an isolation device for aseismic design”, Earthquake Engineering and Structural Dynamics, Vol. 29, pp. 603-627.

[57] Ponzo F.C., Di Cesare A., Arleo G., Totato P. (2010). Protezione sismica di edifici esistenti con controventi dissipativi di tipo isteretico: aspetti progettuali ed esecutivi, Progettazione Sismica, Anno II, n. 1, ppgg. 19-42.

[58] Rabinowicz, E., “Friction temperatures”, Prod. Eng. (NY), (March 30, 1964) 97-99.

[59] Rabinowicz, E. (1995), “Friction and Wear of Materials”, J. Wiley & Sons, Inc., New York.

[60] Reaveley L.R., Mayes R.L. and Sveinsson B.I., (1998). “Seismic Isolation of a Four Story Flight Simulator Manufacturing Facility”, Proc. 9th World Conference on Earthquake Engineering, Tokyo, Japan.

[61] Salomon, G., (1964). “Introduction in Mechanisms of Solid Friction”. P.J. Bryant and Lavik M., Elsevier, Amsterdam, pp. 3-6.

[62] Sextro, W. (2002), “Dynamical contact problems with friction”, pp. 51–54 Springer, Berlin, Heidelberg.

[63] Shames, I. H. and Cozzarelli, F. A (1992), "Elastic and Inelastic Stress Analysis", Prentice Hall, Eng. Jewoods Cliffs, New Jersey.

[64] Shenton, H. W., III, (1996), "Guidelines for Pre-Qualification, prototype and Quality Control testing of Seismic Isolation Systems", National Institute of Standards and Technology, NISTIR 5800, January.

[65] Skinner, R.I. (1982), "Base Isolation provides a large building with increased earthquake resistance; development, design and construction", Int. Conf. Natural Rubber for Earthq. Pro. Of Bldgs. And Vibration Isolation, Kuala Lumpur, Malaysia Feb.

[66] Skinner, R.I., Robinson, W.H. and McVerry, G.H. (1993), "An Introduction to Seismic Isolation", John Wiley and Sons, Chichester, UK.

[67] Soong, T. T. and Dargush, G. F. (1996). "Passive Energy Dissipation Systems in Structural Engineering". Wiley & Sons, London. UK.

[68] T.T. Soong, Michalakis C. Constantinou (2004), "Passive and active structural vibration control in civil engineering", Springer Linkbeilage, Zurich, Switzerland.

[69] Staudacher, E., Habacher C., and Siegenthaler R.(1970), "Erdbebensicherung in Baum", Neue Zurcher Aeitung, Technik

[70] Structural Engineers Association of California (SEAOC) (1985). "Recommended Lateral Design Requirements and Commentary, Blue Book"

[71] Structural Engineers Association of California (SEAO) (1989). "General Requirements for Design and Construction of Seismic-Isolated Structures", Ad hoc Base Isolation Subcommittee of the seismology Committee, Appendix to Chapter 1 of the SEAOC Blue Book.

[72] Structural Engineers Association of Northern California (SEAONC) (1986). "Tentative Seismic Isolation Design Requirements, Yellow Book"

[73] Tabor, D. (1981), "Friction-The Present State of Our Understanding", J. Lubrication, Techn., ASME, Vol. 103, 169-178.

[74] Tarics A.G., Way D. and Kelly J.M. (1984). “The implementation of Base Isolation for the Foothill Communities Law and Justice Center”. Technical Report No. RTA-84, San Francisco, California

[75] Tsopelas, P., Constantinou, M. C., Okamoto, S., Fuji, S. and Ozaki, D. (1996). “Experimental study of bridge seismic sliding isolation system”. Engineering Structures. 18:4, 301–310.

[76] Tsai, C.S. (1997). Finite element formulations for friction pendulum seismic isolation bearings. International Journal for Numerical Methods In Engineering. 40:1, 29-49.

[77] UBC (2007). “Uniform Building Code”, International Code Council, Chapter 16-17.

[78] UNI EN 1998-1:2004, (2004). Eurocode 8: Design of structures for Earthquake Resistance, Part1: General rules, seismic actions and rules for buildings.

[79] UNI EN 1998-2:2005, (2005). Eurocode 8: Design of structures for Earthquake Resistance, Part2: Bridges.

[80] UNI EN 1337-1:2000, (2000). Structural bearings – General design Rules.

[81] UNI EN 1337-2:2004, (2004). Structural bearings- Part 2: Sliding Elements.

[82] UNI EN 1337-3:2005, (2005). Structural bearings- Part 3: Elastomeric bearings.

[83] Udwadia, F. Westermo, B. (1983), “Periodic Response of a sliding Oscillator System to Harmonic Exitation”, J Earthq. Eng. Struct. Dynam., Vol. 11, pp 135-146.

[84] Zayas, V., Low, S., and Mahin, S. (1987). “The FPS earthquake resisting system”. Report No. CB/EERC-87/01”, Earthquake Engineering Research Center, University of California, Berkeley, California.

[85] Zayas, V., Low, S., Bozzo L., and Mahin, S. (1989). “Feasibility and performance studies on improving the earthquakes resistance of new and existing buildings using the frictional pendulum system”. Report No.CB/EERC-89/09, Earthquake Engineering Research Center, University of California, Berkeley, California.

[86] Zayas, V., Low, S. and Mahin, S. (1990). “A simple pendulum technique for achieving seismic isolation”. Earthquake Spectra. 6:2, 317-334.

[87] Way D. and Howard J. (1990). “Seismic Rehabilitation of the Mackay School of Mines with Base Isolation”, Earthquake Spectra, Vol. 6, No. 2.